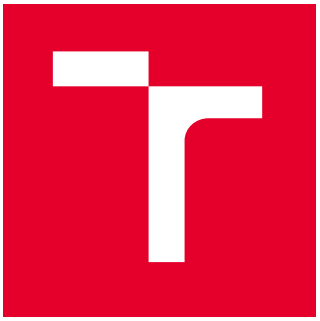

BRNO UNIVERSITY OF TECHNOLOGY

VYSOKÉ UČENÍ TECHNICKÉ V BRNĚ

FACULTY OF MECHANICAL ENGINEERING

FAKULTA STROJNÍHO INŽENÝRSTVÍ

ENERGY INSTITUTE

ENERGETICKÝ ÚSTAV

HEAT TRANSFER IN A RECIPROCATING COMPRESSOR

PŘENOS TEPLA V PÍSTOVÉM KOMPRESORU

DOCTORAL THESIS

DIZERTAČNÍ PRÁCE

AUTHOR — **Ing. Patrik Rapta**

AUTOR PRÁCE

SUPERVISOR — **prof. Ing. Miroslav Jícha, CSc.**

ŠKOLITEL

BRNO 2026

ABSTRACT

The heat exchanged between the gas and the cylinder wall superheats the suction charge and lowers the volumetric efficiency of a reciprocating compressor. This heat transfer is routinely predicted by dimensionless correlations some of which are calibrated on internal combustion engines, which have not been tested directly against the instantaneous in-cylinder flux of a running compressor they are meant to reproduce. The instantaneous in-cylinder heat flux of a small air compressor was therefore measured directly over several pressure ratios, to identify the fluxes, to determine the heat transfer coefficients on selected surfaces, and to assess five published correlations. The surface temperature was recorded with flush-mounted coaxial thermocouples at the valve plate and at two liner positions. The heat flux was recovered through the semi-infinite-solid solution, and the gas temperature was reconstructed from the cylinder pressure with a self-consistent energy balance. The flux reaches tens of kilowatts per square metre and exceeds one hundred at the valve plate. It changes direction at least twice in each revolution and on average carries heat from the wall into the gas, superheating the charge by 35 to 85 K. The heat transfer coefficient is recovered reliably only as a two-term quantity with a magnitude and a phase, because the flux lags the gas-to-wall temperature difference. None of the five correlations reproduces the flux without refitting, and refitting reaches only a common residual floor set by the phase structure of the flux. The analysis also quantified the gas leakage and the suction-line acoustic resonance. The work is the first direct, crank-angle-resolved validation of in-cylinder heat-transfer correlations on a running compressor and shows that the quasi-static coefficient cannot represent the measured phase lag.

KEY WORDS

reciprocating compressor, in-cylinder heat transfer, semi-infinite solid, heat transfer correlations, phase lag

ABSTRAKT

Teplo vyměněné mezi plynem a stěnou válce přehřívá sací náplň a snižuje dopravní účinnost pístového kompresoru. Tento přestup tepla se běžně predikuje pomocí bezrozměrných korelací, z nichž některé jsou kalibrované na spalovacích motorech. Ty doposud nebyly přímo ověřeny vůči okamžitému tepelnému toku ve válci běžícího kompresoru, jejž mají reprodukovat. Okamžitý tepelný tok ve válci malého vzduchového kompresoru byl proto změřen přímo při několika tlakových poměrech, a to za účelem identifikace tepelných toků, určení součinitelů přestupu tepla na vybraných površích a posouzení pěti publikovaných korelací. Povrchová teplota byla snímána zapuštěnými koaxiálními termočlánky na ventilové desce a ve dvou polohách na stěně válce. Tepelný tok byl zpětně určen řešením polonekonečného tělesa a teplota plynu byla rekonstruována z tlaku ve válci pomocí energetické bilance. Tepelný tok dosahuje desítek kilowattů na metr čtvereční a na ventilové desce překračuje sto kilowattů na metr čtvereční. Nejméně dvakrát za otáčku mění směr a v průměru přenáší teplo ze stěny do plynu, čímž přehřívá náplň o 35 až 85 K. Součinitel přestupu tepla lze spolehlivě určit pouze jako dvousložkovou veličinu s velikostí a fází, neboť tepelný tok se opožďuje za teplotním rozdílem mezi plynem a stěnou. Žádná z pěti korelací nereprodukuje tepelný tok bez optimalizace koeficient. Ta však dosahuje pouze společné reziduální meze dané fázovou strukturou tepelného toku. Analýza rovněž kvantifikovala únik plynu a akustickou rezonanci v sacím potrubí. Tato práce představuje první přímou validaci korelací přestupu tepla ve válci běžícího kompresoru s rozlišením podle úhlu natočení kliky a ukazuje, že kvazistatický součinitel nedokáže vystihnout naměřené fázové zpoždění.

KLÍČOVÁ SLOVA

Pístový kompresor, přenos tepla ve válci, polonekonečné těleso, korelace přenosu tepla, fázové zpoždění

BIBLIOGRAPHIC CITATION

RAPTA, Patrik. *Heat transfer in a reciprocating compressor*. Online, doctoral Thesis. Miroslav JÍCHA (supervisor). Brno: Brno University of Technology, Faculty of Mechanical Engineering, 2026. Available at: https://www.vut.cz/en/students/final-thesis/detail/172179.

Affirmation

I hereby declare that I have written the Ph.D. thesis on my own according to advice of my supervisor prof. Ing. Miroslav Jícha, CSc. And all the literary sources are quoted correctly and completely.

In Brno _____

Patrik Rapta _____

CONTENTS

INTRODUCTION 8

1 COMPRESSORS 10

1.1 Working Principle and Types 10

1.2 Compression Cycle 12

1.3 Efficiency 15

1.4 Superheating and its Effect 19

1.5 Valve Dynamics 22

1.6 Leakage 26

2 HEAT TRANSFER IN RECIPROCATING COMPRESSORS 28

2.1 Overview and Historical Development 28

2.2 System-Level Thermal Analysis 29

2.3 In-Cylinder Heat Transfer 31

2.4 Heat Transfer Correlations 35

2.5 Numerical Comparison of Correlations 43

3 METHODS FOR INSTANTANEOUS HEAT FLUX DETERMINATION 47

3.1 Heat Flux Sensors 47

3.2 Semi-Infinite Solid Theory 49

3.3 Heat Flux Calculation Methods 52

3.4 Coaxial Thermocouples 55

4 RESEARCH GAPS AND OBJECTIVES 59

4.1 Research Gaps 59

4.2 Objectives, Research Questions and Hypotheses 61

5 EXPERIMENTAL SETUP 62

5.1 Test Rig and Instrumentation 62

5.2 Signal Processing and Surface Temperature 68

5.3 Thermodynamic Model and Gas State Reconstruction 70

5.4 Heat Flux, Heat Transfer Coefficient, and Nusselt Number 71

5.5 Spectral Analysis of Pressure Pulsations 74

5.6 Cycle-Derived Indices and Leakage 74

5.7 Uncertainty Analysis 75

6 RESULTS AND DISCUSSION 82
6.1 Preliminary Steady-State Characterisation 82
6.2 Validation of Thermocouple Installation 89
6.3 Cylinder Pressure, Valve Events, and Polytropic Exponents 92
6.4 Leakage and Backflow 95
6.5 In-Cylinder Superheating 98
6.6 Compressor Performance 102
6.7 Suction Flow and Valve Dynamics 103
6.8 Surface Temperature and Heat Flux 106
6.9 Heat Transfer Coefficient on Selected Surfaces 109
6.10 Validation of Heat Transfer Correlations 113
7 CONCLUSION 122
7.1 Summary of Findings 122
7.2 Contribution to the Field 123
7.3 Recommendations for Future Work 125
PUBLICATIONS RELATED TO THE THESIS 127
OTHER PUBLICATIONS 128
NOMENCLATURE 130
REFERENCES 134

INTRODUCTION

Compressors have become an increasingly integral component of our day-to-day life. Their application spans a broad range of industrial and commercial sectors, from household refrigeration to large-scale industrial gas compression, petrochemical processing, and heat pump systems. The global number of air conditioning units alone doubled from 800 million to 1.6 billion between 2000 and 2016, with demand projected to continue growing sharply in the coming decades[1]. As a substantial share of electricity is still generated from fossil fuels, improvements in compressor efficiency carry direct environmental implications. The projection illustrated in Figure 1 suggests that the difference between a scenario favouring efficient equipment and one driven purely by cost could amount to approximately 2 800 TWh in annual electricity savings by 2050[1].

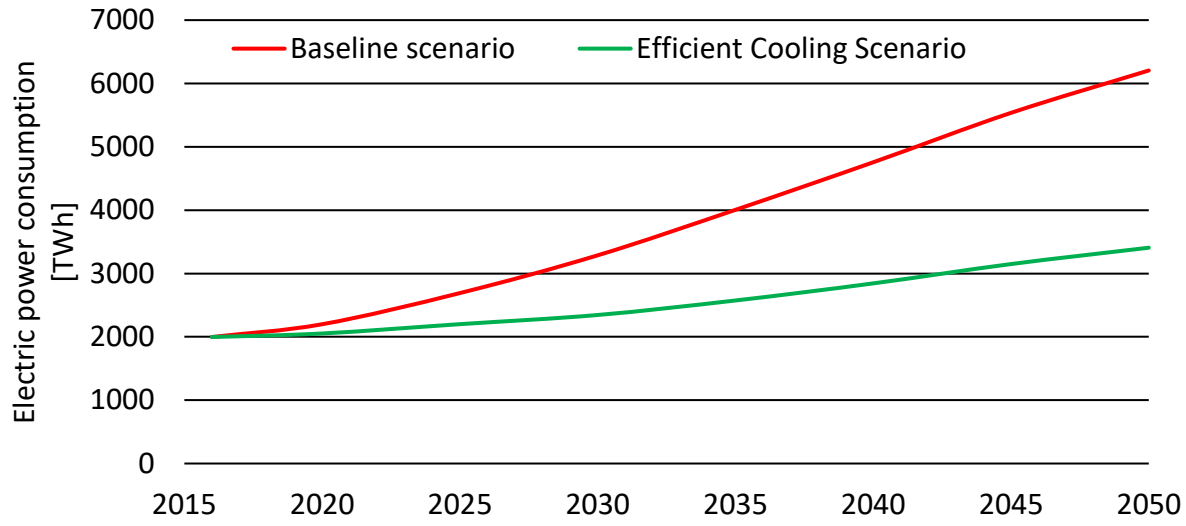

Figure 1 World energy use for space cooling [1]

The overall efficiency of a reciprocating compressor can be decomposed into electrical (~88%), mechanical (~92%), and thermodynamic efficiency (80–83%), with the last offering the greatest potential for improvement [2]. Approximately 49% of thermodynamic losses are attributable to superheating of the working fluid, a consequence of heat transfer from the warm cylinder walls and cylinder head to the cold incoming gas during the suction process [2], [3]. Accurate characterisation of this instantaneous in-cylinder heat transfer is essential to understanding and improving compressor performance.

Several empirical Nusselt correlations have been proposed for this purpose. Some were developed originally for internal combustion engines [4], [5]. Others were derived specifically for reciprocating compressors, either from experimental data [6], [7], [8] or from numerical simulations [9], [10]. Despite this body of work, no consensus exists on which correlation best represents physical reality, and their accuracy has not been fully verified experimentally, owing in large part to the difficulty of measuring instantaneous in-cylinder conditions [11], [12].

The experimental determination of instantaneous heat flux inside the cylinder is challenging

because of the dynamic nature of the process, limited access, and mechanical constraints [6]. The established approach, inferring heat flux from surface temperature measured by coaxial thermocouples via semi-infinite solid theory [13], [14], [15], is well suited to these conditions, as temperature fluctuations are effectively dampened within the first few millimetres [16]. Evaluating the heat transfer coefficient HTC from the resulting heat flux requires knowledge of the instantaneous gas temperature, which is itself a challenging quantity to obtain. Direct measurement by thermocouples is complicated by their thermal inertia. Even fine-wire probes require numerical compensation of the temperature signal to recover instantaneous values [2], [17] making indirect reconstruction from a thermodynamic model the more practical approach. High-frequency synchronised acquisition is a further prerequisite, as low sampling rates are insufficient to resolve the crank-angle-dependent surface temperature variations [12].

The present work adopts this approach to provide a systematic experimental comparison of established Nusselt correlations against crank-angle-resolved heat flux measurements at multiple locations and across a range of pressure ratios (PR). A test rig based on the EK 4-2 reciprocating compressor (Orlík, Czech Republic) is instrumented with coaxial type-E thermocouples, cylinder pressure sensors, and an encoder, with synchronised acquisition at 50 kHz. Instantaneous heat flux is determined from surface temperature via semi-infinite solid theory, and the HTC is evaluated using instantaneous gas temperature reconstructed from a zero-dimensional thermodynamic model. The experimental Nusselt number profiles are then compared against established correlations phase by phase (compression, discharge, expansion, and suction), enabling, for the first time on this class of compressor, an assessment of which models capture the physical reality of in-cylinder heat transfer with sufficient fidelity.

1 COMPRESSORS

Reciprocating compressors are among the most widely used mechanical systems in modern industry, operating across an extraordinary range of conditions and working fluids. This chapter introduces the working principle, classification, and performance characteristics of reciprocating compressors, with emphasis on the thermodynamic loss mechanisms that motivate the present research.

1.1 Working Principle and Types

A compressor is a machine that increases the pressure of a gas by supplying mechanical work to it. This distinguishes it from a fan or blower, which moves gas at approximately constant pressure, and from a pump, which performs an analogous function on liquids. The energy input to the compressor is ultimately stored in the compressed gas as increased enthalpy and, in systems operating on the vapour compression refrigeration cycle, is transferred to the condenser as the working fluid returns to its liquid state.

Two very different physical principles govern how compressors achieve this pressure increase. In dynamic compressors, kinetic energy is imparted to the gas by a rotating impeller and subsequently converted to pressure through diffusion. The gas flow is continuous, and the machine operates at essentially steady state. Turbocompressors (centrifugal and axial) and ejectors are the principal representatives of this class (Fig. 1.1). Dynamic compressors are the preferred choice in large-scale power generation, aviation, and industrial gas processing where continuous flow at high volume is required.

In positive displacement compressors, a defined volume of gas is mechanically enclosed and progressively reduced, raising its pressure before the compressed charge is discharged. This class covers a broad range of machine types. Rotary positive displacement compressors (Figure 1.1) achieve this volume reduction through the rotation of shaped elements within a housing. They provide continuous or near-continuous flow and are compact. Among rotary types, the scroll compressor has become particularly prevalent in small-to-medium capacity air conditioning and heat pump systems because of its low noise, high part-load efficiency, and mechanical simplicity. Reciprocating compressors achieve the same volume reduction by means of a piston moving within a cylinder, driven by a crank mechanism. The gas is admitted and discharged through self-acting valves that open and close in response to pressure differences alone, with no external actuation. The classification of compressor types is summarised in Fig. 1.1, with the reciprocating branch, the focus of this work, highlighted.

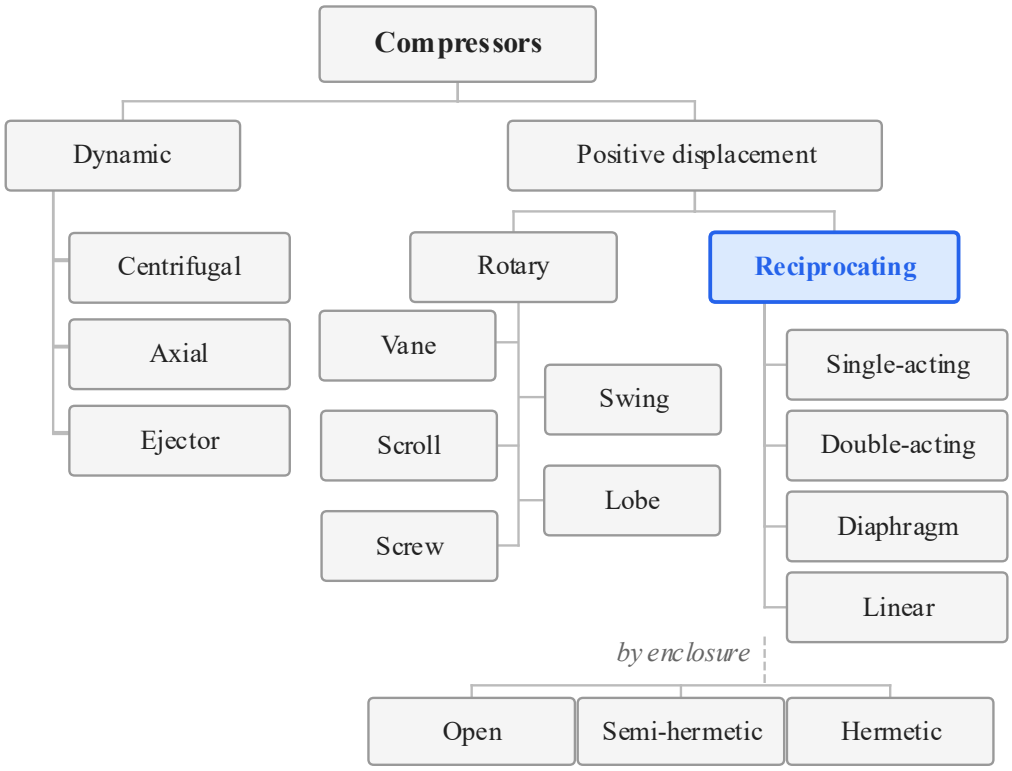

Figure 1.1 Classification of compressors by operating principle and constructional type. The reciprocating compressor branch, which is the subject of the present work, is highlighted.

Positive displacement compressors are further classified by the number of compression stages, by the range of pressure ratio achieved, and by their constructional enclosure. In open compressors, the cylinder block is mechanically separate from the drive motor and connected to it by a shaft seal, enabling the motor to be replaced independently and the refrigerant circuit to be serviced externally. This configuration is standard in large industrial and transport refrigeration plant. Semi-hermetic compressors enclose the motor and compression mechanism in a bolted housing, allowing internal access for maintenance while reducing the risk of refrigerant leakage. Fully hermetic compressors weld or braze the motor and compression assembly into a sealed shell. They are not field-serviceable but are compact, inexpensive to manufacture, and virtually leakproof, making them the dominant design for household refrigerators, air conditioners, and small-to-medium commercial refrigeration equipment.

The vapour compression cycle, in which a compressor raises the pressure of a gaseous refrigerant that has absorbed heat at low pressure from the cooled space, underlies the overwhelming bulk of air conditioning and refrigeration equipment in use worldwide [1]. Within this technology class the specific compressor type varies by application and capacity range. Scroll and rotary vane compressors dominate in split-system and window air conditioning units because of their compactness and low noise at the capacity levels typical of residential cooling. Reciprocating compressors in fully hermetic form are the standard choice for household refrigerators and freezers, where their robustness, wide pressure ratio range, and low manufacturing cost at small displacement volumes are decisive advantages. They remain widely used in commercial refrigeration plant and multi-stage high-pressure applications across the full range of enclosure

types.

Beyond refrigeration and air conditioning, reciprocating compressors are essential in many industrial applications where their ability to reach high pressure ratios with precise volumetric control is not matched by other machine types. In natural gas processing, petrochemical plant, and hydrogen compression, large open reciprocating machines handle the demanding combination of high pressure, low molecular weight, and variable flow. In carbon capture, utilisation, and storage systems, reciprocating compressors raise captured CO_2 to the supercritical pressures required for pipeline transport and geological injection [7]. Compression is one of the most energy-intensive stages in the entire process chain. Reciprocating liquid-hydrogen pumps pressurise LH_2 to the supercritical state (40 to 100 MPa) under cryogenic conditions[18]. The thermodynamic losses of the compression process, dominated in all these cases by in-cylinder heat transfer, are directly relevant to the decarbonisation of industrial sectors that have few alternative abatement pathways.

The convective heat transfer in the cylinder is characterised through dimensionless correlations, in which the influence of working fluid properties is captured implicitly. Air, as an ideal gas with well-characterised thermophysical properties, provides a reproducible test medium for studying these mechanisms, and the resulting correlations carry over to other working fluids through the same framework [11]. The prevalence of reciprocating compressors across applications whose efficiency improvement has direct environmental consequence, together with the suitability of air as a representative working fluid, motivates the present work.

1.2 Compression Cycle

A connecting rod of length *L* couples the crank pin, located at radius *r* from the crankshaft axis to the piston pin (Fig. 1.2). As the crankshaft rotates through angle θ, the piston displacement from top dead centre is [19]:

$$x(\theta) = r \cdot (1 - \cos\theta) + L \cdot \left(1 - \sqrt{\left(1 - \left(\frac{r}{L} \cdot \sin\theta\right)^2\right)}\right) \tag{1.1}$$

The instantaneous volume of the compression space is therefore

$$V(\theta) = V_D + \left(\frac{V_h}{2}\right) \cdot \left[(1 - \cos\theta) + \left(\frac{r}{4L}\right) \cdot (1 - \cos 2\theta)\right] \tag{1.2}$$

where V_D is the clearance volume remaining at top dead centre, V_h is the displacement volume, and the final term arises from the geometric series expansion of the exact expression for small values of the crank ratio *r/L [20]*. The resulting approximately sinusoidal variation of cylinder volume with crank angle governs the timing and magnitude of all thermodynamic events in the cycle.

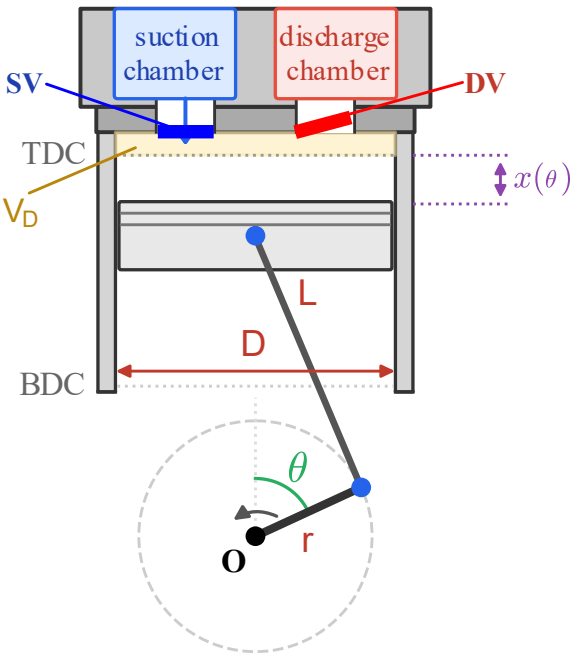

Figure 1.2 Schematic of the reciprocating compressor with crank mechanism, cylinder, piston with rings, valve plate with self-acting suction (SV) and discharge (DV) valves, and suction/discharge chambers. Key dimensions are the crank radius r, connecting rod length L, bore D, clearance volume V_D. TDC and BDC denote top and bottom dead centre, $x(\theta)$ is the piston displacement from TDC.

The piston operates within the cylinder bore and is sealed against it by piston rings. These rings prevent leakage of compressed gas past the piston while providing a low-friction sliding contact. The cylinder head carries the valve plate, in which suction and discharge ports are opened and closed by self-acting valves, flexible or spring-loaded elements that respond passively to the instantaneous pressure difference across them, opening when the driving differential exceeds the closing force and closing when it reverses. This is the fundamental operational distinction between reciprocating compressors and internal combustion engines. In an engine, inlet and exhaust valves are driven by a camshaft on a fixed timing determined by the engine speed, whereas in a compressor the valves are driven by the gas itself and their timing adapts automatically to the prevailing pressure conditions. Several valve geometries are in common use (Fig. 1.3). Reed valves use a thin elastic strip that is deflected by the pressure difference and acts as a cantilever with stiffness

$$k = \frac{E \cdot b \cdot \delta^3}{L_b^3} \tag{1.3}$$

determined by the material modulus E, strip width b, thickness δ, and free length L_b [21]. Ring and plate designs lift an annular or slotted plate axially. In all cases the valve responds dynamically to the instantaneous pressure difference, and its lift, velocity, and impact with the seat at closing are governed by coupled equations of fluid dynamics and structural mechanics rather than by external control.

The suction chamber connects the low-pressure inlet port to the cylinder through the suction

valve, providing a buffer volume that smooths the pulsating suction flow. Correspondingly, the discharge chamber collects the compressed gas from the discharge valve before it passes to the outlet. These chambers are central to the overall thermal balance of the compressor, as the gas that passes through them exchanges heat with the surrounding structure.

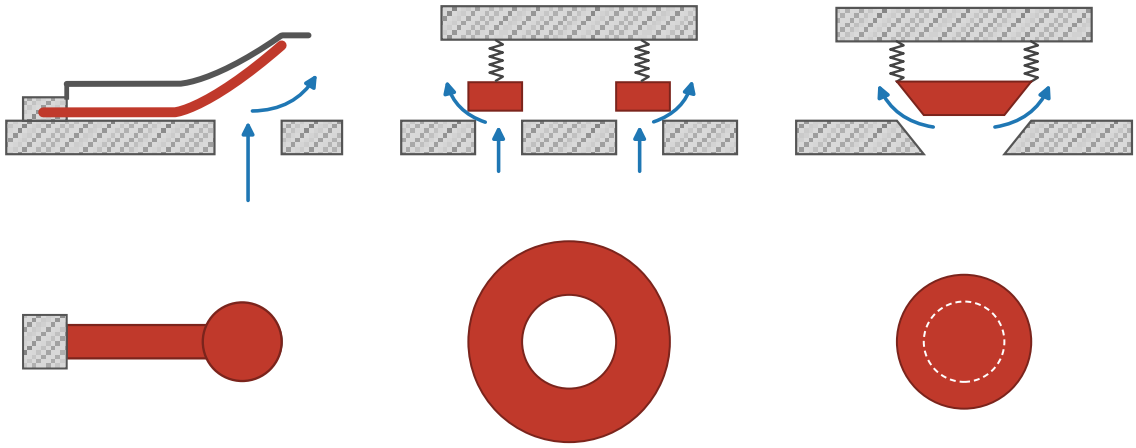

Figure 1.3 Common self-acting discharge-valve geometries in reciprocating compressors. (a) reed, (b) ring, (c) plate/disc.

The compression cycle consists of four sequential phases, shown on the p-V diagram in Fig. 1.4. The four phases are expansion of the gas trapped in the clearance volume after top dead centre (TDC), suction once the cylinder pressure falls below the suction pressure, compression after bottom dead centre (BDC), and discharge once the cylinder pressure exceeds the discharge pressure by the amount needed to open the valve. The compression trajectory lies between the isothermal and isentropic limits and is characterised by a polytropic index n with $1 < n < \kappa$ that depends on the rate of heat exchange with the cylinder walls.

The polytropic index n characterises the compression trajectory but does not in general remain constant throughout the cycle. Its effective value varies with crank angle as the balance between heat transfer and compression work shifts, and it depends on the specific operating conditions and wall temperatures. For the two closed-valve phases, compression and expansion, a more direct thermodynamic description is available. With the valves closed, the cylinder forms an approximately sealed control volume in which the gas mass m is constant. The instantaneous gas temperature can then be recovered directly from the ideal gas law:

$$T_{gas}(\theta) = \frac{p(\theta) \cdot V(\theta)}{m \cdot R} \tag{1.4}$$

where m is determined from the thermodynamic state at a reference crank angle, conventionally the moment of inlet valve closing for compression, and the moment of discharge valve closing for the subsequent expansion of clearance gas. This approach requires no assumption about the value of n and relies solely on the measured pressure trace and the known cylinder geometry,

making it more robust than the polytropic relation under conditions where n is poorly defined. For the open-valve phases, suction and discharge, the gas mass is not constant, and the instantaneous temperature cannot be recovered by the same method without knowledge of the instantaneous mass flow rate through the valve, a substantially more demanding measurement.

The real p-V diagram (solid line in Fig. 1.4) departs from the theoretical ideal (dashed line) in several practical ways [2]. The ideal cycle assumes instantaneous valve events, no pressure losses, and adiabatic compression. Finite valve pressure drops inflate the area of the p-V loop. During suction the cylinder pressure lies below p_{suc} by the pressure drop Δp_{sv} across the suction valve, and during discharge it exceeds p_{dis} by Δp_{dv} across the discharge valve. This raises the indicated work above the isentropic reference. Re-expansion of the trapped clearance gas delays the opening of the suction valve and reduces the net mass of fresh gas admitted in each stroke. These deviations have a direct quantitative impact on both the volumetric and the isentropic efficiency of the machine.

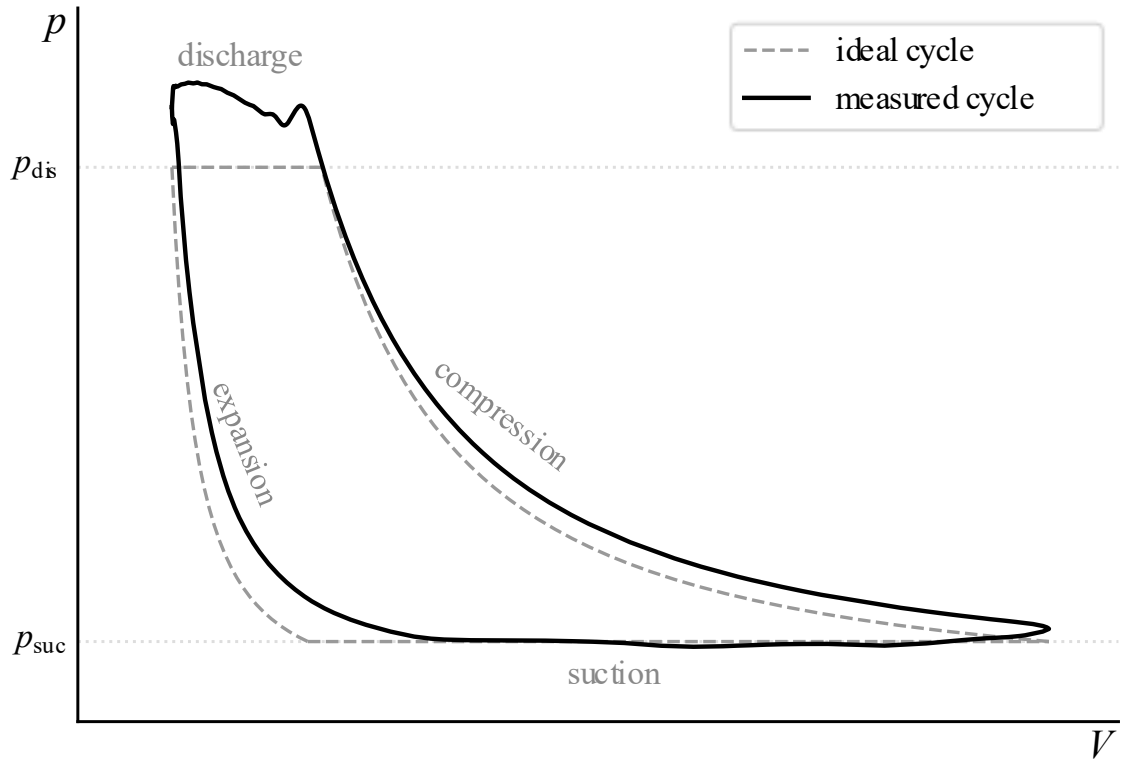

Figure 1.4 Indicator (p–V) diagram of the Orlík EK 4-2 compressor measured at a higher pressure ratio. The dashed line is the ideal cycle with isentropic compression and expansion between the suction pressure and the vessel pressure. The solid line is the measured cycle.

1.3 Efficiency

These stages are quantified by the electrical efficiency, the mechanical efficiency, the isentropic efficiency, and the volumetric efficiency. The first two are largely determined by the motor and mechanism design. The latter two are directly affected by the thermodynamic processes within the cylinder, and in particular by the heat exchange between the gas and the cyl-

inder walls [22], [23], making the isentropic and volumetric efficiency the central link between compressor performance and in-cylinder heat transfer.

The electrical efficiency of the drive motor

$$\eta_e = \frac{\dot{W}_m}{\dot{W}_e} \tag{1.5}$$

It typically reaches 87 to 88 % for the small hermetic and semi-hermetic machines common in refrigeration applications [2], [24]. It reflects the conversion losses in the motor windings and the slip of the asynchronous motor at its operating frequency. The value is set mainly by motor design and is relatively insensitive to the compressor operating point. It therefore offers limited scope for improvement through changes to the compression cycle itself.

The mechanical efficiency (1.6) is the fraction of shaft power converted into indicated compression power $\dot{W}_{cp}$ after overcoming bearing friction, piston ring friction, and losses in the connecting rod and crankshaft assembly. It reaches up to 92 % in well-designed machines [2].

$$\eta_m = \frac{\dot{W}_{cp}}{\dot{W}_m} \tag{1.6}$$

The dominant contribution to mechanical losses is the friction at the main bearings and the piston-cylinder interface. These depend on lubricant viscosity, surface finish, and the normal forces generated by the crank geometry, and are reduced by careful design of the lubrication system and piston clearance.

The isentropic efficiency η_{is}, defined as the ratio of the isentropic compression work $\dot{W}_{is}$ to the actual indicated work (1.7). It ranges from about 80 to 83 % for small hermetic reciprocating compressors running with refrigerants at typical vapour compression cycle conditions [2], [11]. These values give a representative benchmark, although the exact figure depends on the working fluid, the pressure ratio, and the machine size.

$$\eta_{is} = \frac{\dot{W}_{is}}{\dot{W}_{cp}} \tag{1.7}$$

Its departure from the ideal process reflects several irreversibility sources that can be decomposed by thermodynamic phase. Losses during suction arise from pressure drops across the suction valve and from superheating of the incoming gas by heat transfer from the warm cylinder walls. Losses during compression arise from the deviation of the polytropic trajectory from the isentropic ideal. Losses during discharge arise from pressure drops across the discharge valve and from heat transfer to the gas as it passes through the hot discharge port. Losses during re-expansion of clearance gas reduce the work that can be recovered from the trapped volume [22], [25]. Of these, thermodynamic losses attributable to heat transfer represent the greatest single source of departure from ideal performance and so the greatest potential for improvement [2].

The temperature–entropy (*T*-*s*) diagram (Fig. 1.5) makes the role of heat transfer in the compression process easy to follow. In the isentropic reference process compression follows a vertical path at constant entropy. In the real polytropic compression the heat exchange with the cylinder walls bends the trajectory. Early in the stroke the gas is cooler than the wall, heat flows into the gas, and the path shifts to the right of the isentrope. Once the gas temperature exceeds the wall temperature, the flux reverses and the path curves back toward the isentropic reference.

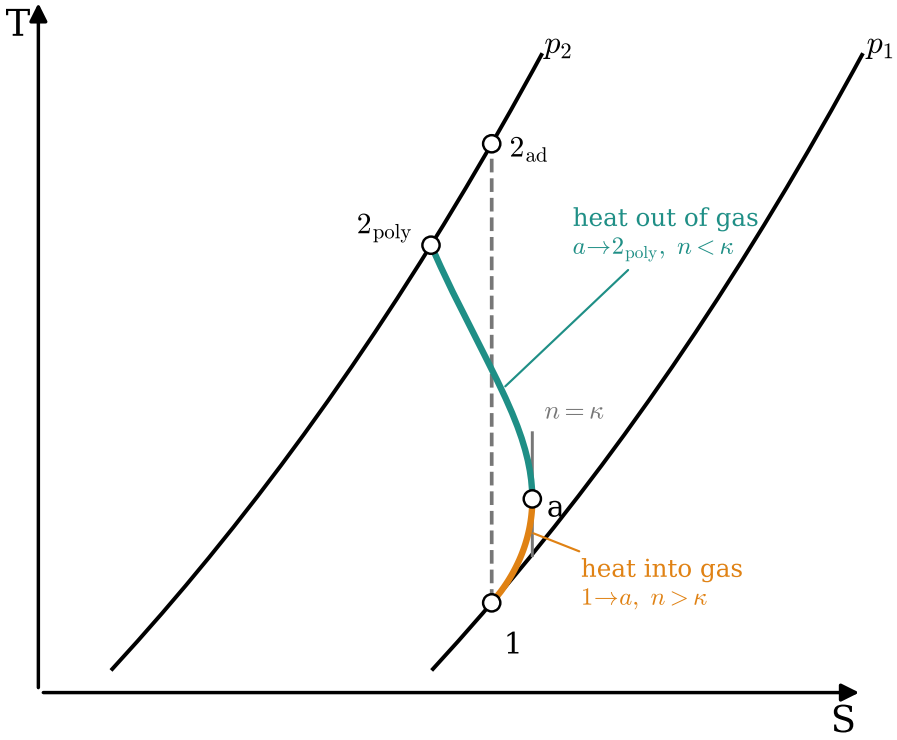

Figure 1.5 Temperature–entropy (*T*–*s*) diagram of in-cylinder compression with heat transfer. The dashed grey line marks the isentropic reference $1 \rightarrow 2_{ad}$. Along the real polytropic path the cool gas is first heated by the wall ($1 \rightarrow a$, $n>\kappa$), then rejects heat once it becomes hotter than the wall ($a \rightarrow 2_{poly}$, $n<\kappa$). Point a marks where the gas and wall temperatures are equal ($n=\kappa$).

The T-s diagram thus makes the qualitative role of each heat exchange event clear. A segment lying to the right of the isentropic line indicates entropy generation due to heat flowing into the gas, while a segment lying to the left indicates heat flowing from the gas to the walls. The thermodynamic effect of heat exchange depends strongly on the direction of the flux and the phase of the cycle in which it occurs. Heat flowing from the wall into the cold gas early in compression increases the required work, while heat flowing from the hot gas to the walls later in compression reduces it. Understanding which heat exchange events dominate, and when they occur within the cycle, is the central question for improving compressor thermodynamic efficiency.

The volumetric efficiency (equation 1.8) expresses how effectively the displacement volume is used to deliver fresh gas. It splits into three multiplicative contributions [22]. These are the effect of motor slip at the operating frequency, the deviations from the ideal cycle caused by valve pressure drops, heat transfer, supercharging, back-flow, and leakage, and the purely geometric effect of the clearance volume (equation 1.9),

$$\eta_v = \frac{V}{\nu_1 \cdot V_{sw}} \tag{1.8}$$

$$\eta_{v_c} = 1 - \varepsilon_c \cdot \left(P^{1/\kappa} - 1\right) \tag{1.9}$$

With ε_c the clearance ratio. This last contribution is one of the most practically significant design parameters, because re-expansion of the trapped clearance gas occupies an increasingly large fraction of the inward stroke as the pressure ratio rises. The re-expanded volume is

$$V_{D,re} = C \cdot V_{sw} \cdot \left(\frac{p_{dis}}{p_{suc}}\right)^{1/\kappa} \tag{1.10}$$

and the volumetric efficiency thus decreases with increasing pressure ratio. Halving the clearance ratio from 2.0 % to 0.8 % improved volumetric efficiency by about 11.6 % at a representative operating condition [22]. Doubling the piston-cylinder gap from its nominal value to 0.01 mm reduced volumetric efficiency by about 7.9 % and isentropic efficiency by about 10 %. This sensitivity underlines the importance of tight manufacturing tolerances. The other major contributor to η_v degradation is superheating of the incoming gas by heat transfer from the warm cylinder walls, treated separately in Section 1.4.

The coupling between isentropic and volumetric efficiency is not just additive. A lower isentropic efficiency typically implies higher discharge temperatures and warmer cylinder walls, which in turn increase suction gas superheating and further degrade volumetric efficiency. Cooling of the gas during compression, achieved by effective heat transfer from the gas to the cylinder walls, instead reduces the compression work and yields an in-cylinder thermal efficiency contribution exceeding 100 %, since removing heat during compression is thermodynamically beneficial relative to the isentropic reference [22].

The scale of the thermal challenge is reflected directly in the energy balance of the machine. In a hermetic reciprocating compressor at steady state, the heat rejected from the shell to its surroundings accounts for 70 to 80 % of the total electrical power input, a consequence of compression work, mechanical friction, and motor losses all ultimately appearing as heat within the sealed enclosure [23]. Even in open compressors, where motor heat is not recirculated through the gas path, the compression process alone raises the cylinder walls and valve plate to temperatures that drive substantial heat fluxes into the gas during each suction stroke. A quantitative picture of where these losses are concentrated is given by the loss breakdown of Ribas [2], reproduced in Fig. 1.6. Suction gas superheating accounts for about 49 % of all thermodynamic losses, suction losses for 25 %, discharge losses for 22 %, and leakage for the remaining 4 %. The dominance of the superheating term, itself a direct consequence of heat transfer from the warm walls and valve plate to the cold incoming gas, makes in-cylinder heat transfer the single most important thermodynamic loss mechanism in this class of machine. This is the primary engineering motivation for its accurate experimental characterisation. Heat transfer losses account for about 7 % of the fractional reduction in isentropic efficiency and 15 % of the fractional reduction in volumetric efficiency, both substantially higher than for a scroll compressor

under identical conditions [26]. The difference is attributable to the suction valve and to the larger temperature difference between the suction and discharge sides in the reciprocating configuration.

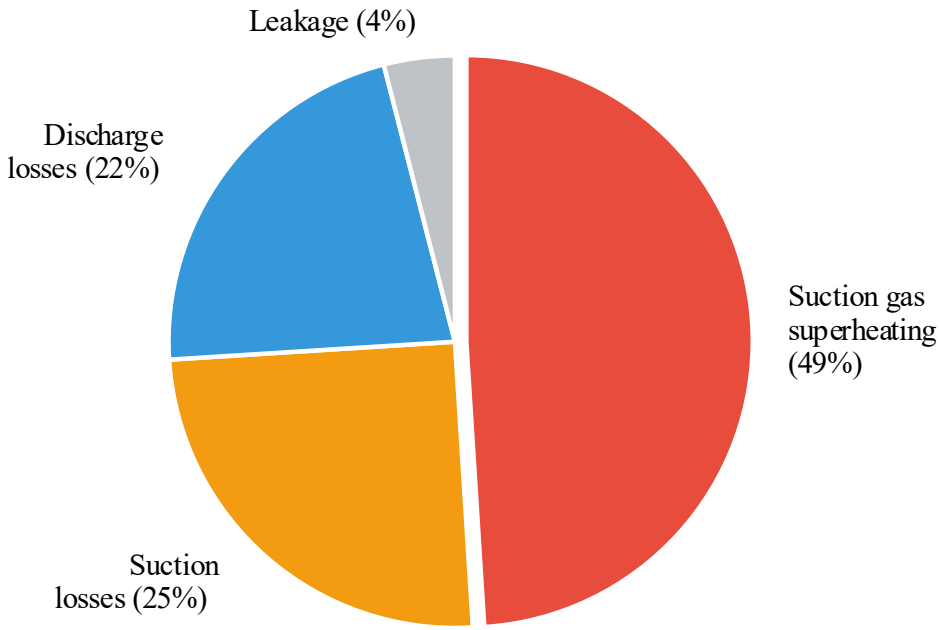

Figure 1.6 Thermodynamic loss breakdown for a hermetic R-134a reciprocating compressor [2].

1.4 Superheating and its Effect

Superheating, in the context of reciprocating compressors, refers to the increase in gas temperature above the suction line temperature that the working fluid undergoes before it reaches the cylinder and begins to be compressed. Unlike the isentropic temperature rise during compression, which is the intended thermodynamic process, superheating represents a parasitic heat gain that imposes an efficiency penalty without delivering any useful work, and its physical origins and mitigation are the central concern of this section.

Superheating does not occur at a single location. It accumulates along the entire suction path of the gas (Fig. 1.7). In hermetic and semi-hermetic compressors, a fraction of the incoming gas recirculates within the compressor shell before entering the suction muffler, where it absorbs heat from the motor windings, the discharge line, and other warm surfaces. The mixing parameter (equation 1.11) is the fraction of suction gas that enters the muffler directly from the suction pipe, rather than the fraction that has circulated through the warm shell interior [27]. A parametric study showed that φ is a first-order determinant of the suction gas temperature, and therefore of volumetric efficiency.

$$\varphi = \frac{\dot{m}_{dir}}{\dot{m}_{total}} \tag{1.11}$$

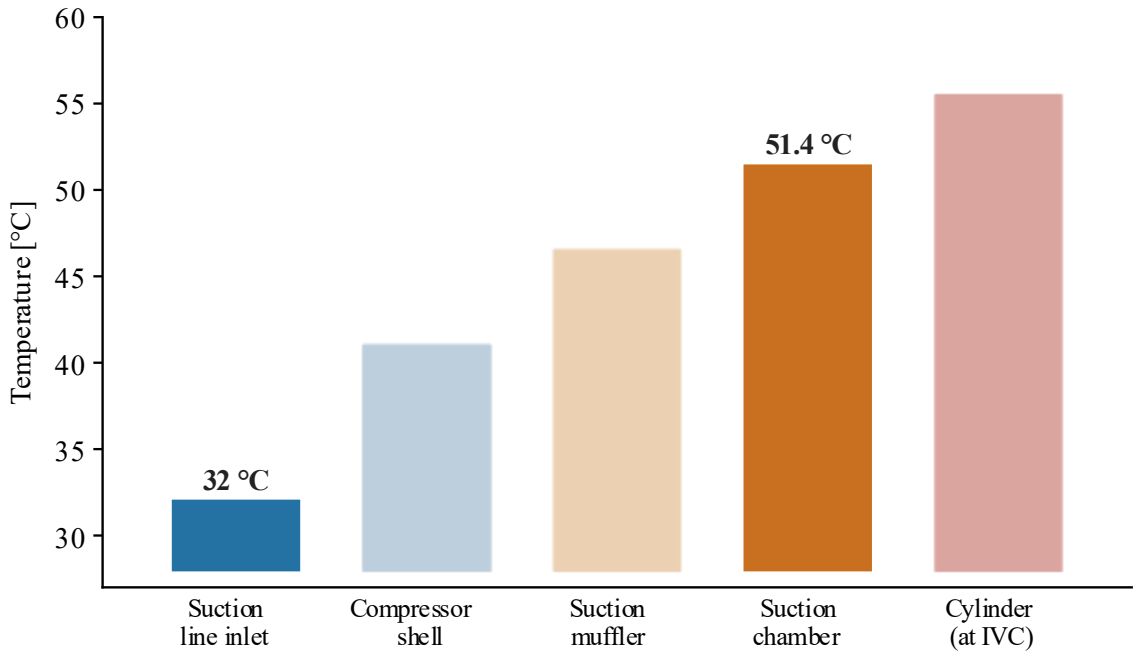

Figure 1.7 Cumulative superheating of the suction gas along the flow path from suction line inlet to the cylinder at inlet valve closing. Data for operating condition A [3].

In open compressors drawing air directly from the environment this shell-recirculation mechanism is absent. The relevant superheating sources are instead the suction piping, the suction chamber, and the cylinder itself. The suction-branch contribution is captured explicitly through the term $\tilde{\eta}_{Q(sl)}$, which treats the heat gain in the suction branch as a direct efficiency loss [22]. In the suction chamber immediately upstream of the suction valve, the gas temperature rises further through heat exchange with the warm cylinder head and valve plate. The only direct experimental characterisation of instantaneous thermodynamic conditions in the suction chamber of a reciprocating compressor used hot-wire and cold-wire probes to measure gas temperature and velocity at 3600 rpm [3]. With the suction valve closed, the gas temperature in the suction chamber exceeded the adiabatic reference by about 7.9°C. This is a substantial local superheating that occurs before the suction valve even opens. Once the suction valve opens and gas enters the cylinder, it meets the warm cylinder walls, valve plate, and piston top, and gains additional heat throughout the induction stroke.

The physical mechanism by which suction superheating degrades compressor performance operates through two coupled pathways. First, a higher gas temperature at the start of induction means a lower gas density, by the ideal gas law,

$$\rho = \frac{p}{R \cdot T} \tag{1.12}$$

so that at fixed suction pressure a gas at higher temperature occupies more specific volume. The cylinder thus draws in less mass in each stroke for the same displaced volume, which

reduces the volumetric efficiency directly. Second, gas entering the cylinder at an elevated temperature begins compression from a higher thermal state and needs more work per unit mass to reach the discharge pressure. This raises the indicated specific work and degrades isentropic efficiency [26]. Reciprocating compressors are therefore substantially more sensitive to in-cylinder heat transfer losses than scroll compressors running under identical conditions. The additional heat gain through the suction valve pathway is specific to the reciprocating design. The system-level consequence of this temperature penalty extends beyond the compressor itself. In hermetic refrigeration compressors, each 1 K rise in the compression start temperature reduces the coefficient of performance of the refrigeration system (Table 1.1) [28]. This sensitivity is specific to refrigerant-cycle machines, but it shows why the temperature at which compression begins is a first-order design parameter.

The quantitative significance of superheating has been debated in the compressor literature for decades. In-cylinder heat transfer was estimated to cause as much as a 10 to 20 % decrease in compressor thermodynamic and volumetric efficiencies [6]. Simulation later showed the maximum negative effect of internal heat transfer on efficiency to be unlikely to exceed 2.5 % under practical conditions, suggesting the earlier estimate was exaggerated [25]. The principal quantitative estimates are collected in Table 1.1. That conclusion held only if the HTC took the values predicted by available correlations, and changed substantially if the true coefficient were higher, a qualification that subsequent work has largely confirmed. The disagreement between correlations is substantial, and the actual magnitude of the superheating penalty depends strongly on the accuracy of the heat transfer model used.

Table 1.1 Reported impact of suction gas superheating on compressor performance

Source	Reported effect
Adair [6]	10–20 % decrease in thermodynamic and volumetric efficiency
Brok [25]	maximum efficiency penalty below 2.5 %
Almbauer [28]	−0.32 % COP per +1 K increase of the compression-start temperature
Sim [27]	halving the suction-side HTC lowered the chamber temperature by 7.8 °C and raised volumetric efficiency by 3 %

The dynamical character of superheating is a further reason why quasi-static or time-averaged treatments are inadequate. The gas temperature in the suction chamber is not a slowly varying quantity but oscillates in response to pressure waves generated by valve opening events [3]. When the suction valve is closed, the temperature oscillations are caused by acoustic pressure waves propagating within the chamber. The gas velocity rises from about 3 m/s in the closed-valve state to about 32 m/s at valve opening, a change of an order of magnitude that occurs over a fraction of the compressor cycle. This strongly non-stationary character means that the superheating penalty depends on the instantaneous thermal state of the gas at the moment the

valve opens, not on a cycle-average temperature. Capturing it accurately requires time-resolved measurements and modelling tools that resolve the valve event itself.

Reducing superheating is one of the primary routes available to improve the thermodynamic performance of reciprocating compressors, and it motivates the need for quantitative knowledge of the in-cylinder heat transfer process. In hermetic compressors, insulation of the suction system is one direct approach. At the in-cylinder level, halving the thickness of the suction valve, which reduces flow restriction and the pressure drop during induction, improves volumetric efficiency by about 0.8 % and isentropic efficiency by about 1.0 % [22]. All these design interventions require knowledge of the instantaneous HTC and its variation through the cycle, because the gain from any given measure depends on when and where the heat exchange occurs. Without crank-angle-resolved experimental data, it is not possible to evaluate which interventions are most effective or to validate the numerical models used for compressor design. The characterisation of instantaneous in-cylinder heat transfer that motivates the present work is therefore a direct prerequisite for evidence-based reduction of the dominant thermodynamic loss.

1.5 Valve Dynamics

The behaviour of the self-acting valves, whose geometric variety was introduced in Section 1.2, governs not only the timing and completeness of the gas exchange but also the velocity and direction of the gas flows that dominate in-cylinder heat transfer during the open-valve phases. A physical description of valve dynamics is a prerequisite for understanding both the deviations of the real p-V diagram from the theoretical ideal and the flow conditions that motivate the velocity-based heat transfer correlations. The valves respond passively to the instantaneous pressure difference across them, and their motion is governed by the coupled interaction of gas forces, spring forces, and the inertia of the valve plate.

The motion of a self-acting valve plate is governed by the balance of gas pressure forces, spring restoring force, and plate inertia [19], [29]. The valve opens only when the net gas force exceeds the spring resistance, stays open as long as this condition holds, and closes with a delay set by plate inertia after the pressure difference reverses. The mass flow rate through the open aperture is governed by the instantaneous pressure difference and the effective flow area, which varies continuously with valve lift. Two consequences follow. First, when the pressure difference reverses while the valve is still open, back-flow occurs and gas is partially expelled from the cylinder, which reduces the net volumetric efficiency [19]. Second, the mass flow rate, and with it the gas velocity through the valve passage, peaks not at the instant of valve opening but later, when a larger aperture is available.

The equations of motion and flow above describe the idealised behaviour of a single-degree-of-freedom spring-mass system responding to a smoothly varying pressure difference. In practice, three qualitatively distinct patterns of valve motion are observed (Fig. 1.8), each with different consequences for compressor performance. In the ideal case the valve opens promptly,

stays fully open throughout the gas exchange phase, and closes precisely at its end. In the second pattern the valve closes with a delay beyond what the pressure-spring balance alone would predict. The plate inertia, together with the viscous resistance of the lubricating oil film trapped between the valve plate and its seat, resists the motion of the plate even after the net driving pressure force has reversed. This phenomenon, known as valve stiction, arises because the oil film between the plate and its seat must be physically displaced. The required viscous force scales inversely with the cube of the film thickness [30], and viscous effects dominate over capillary and surface-tension effects under dynamic conditions, and the delay grows with oil viscosity and contact area [31]. The practical consequence is a period of reverse flow through the still-open valve that reduces the net gas mass retained in the cylinder beyond what the pressure-reversal mechanism alone would produce. In the third pattern, valve flutter, the plate oscillates during the gas exchange phase and repeatedly impacts the seat or the stop. The impacts radiate pressure waves into the connected chamber, and the oscillation reduces the time-averaged effective flow area and raises the indicated work. Under unfavourable operating conditions (high pressure ratio, elevated rotational speed, or geometric mismatches between the valve and its passage) the flow through the valve aperture can reach sonic conditions. At that point the mass flow rate becomes independent of the downstream pressure and the valve loses its self-regulating character entirely. This choking condition sets an upper bound on the gas delivery rate that cannot be overcome by further increasing the pressure difference.

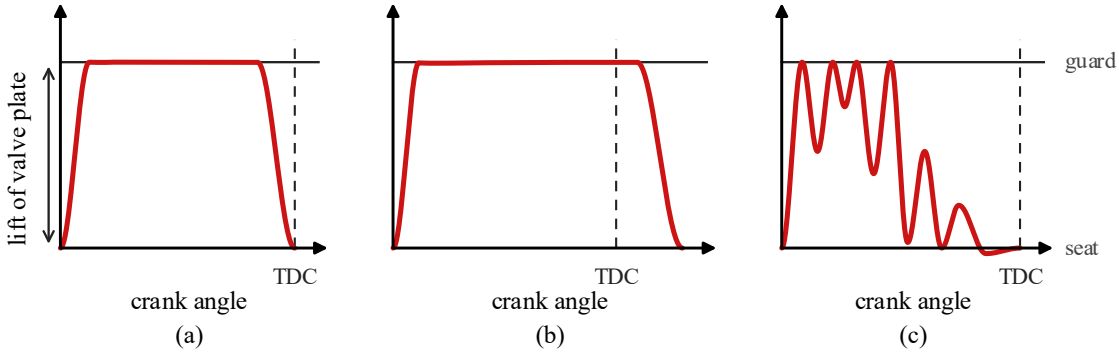

Figure 1.8 Qualitative valve lift l_v as a function of crank angle θ for three characteristic motion patterns. (a) ideal opening and closing, (b) delayed closing due to oil-film stiction, (c) flutter with repeated impacts on seat and stop. Grey band indicates the gas-exchange phase.

The closing of a valve is not just a mechanical event but an acoustic one. When the suction valve closes at the end of the induction stroke, or the discharge valve closes at top dead centre, the abrupt termination of the gas column flow generates a pressure wave that propagates through the connected chamber. The coupling between valve dynamics and pressure pulsations in the suction system is bidirectional. Pressure fluctuations in the muffler affect the valve dynamics, and the valve motion in turn generates the pulsations. This coupling must be resolved simultaneously for accurate compressor simulation [32]. On the discharge side, valve opening starts a rarefaction wave that travels back and forth in the compression chamber, generating oscillating pressure forces on the piston and contributing to valve losses [33]. These internal pressure pulsations arise mainly at valve transition events and are amplified by flutter during

the open-valve phase. They travel through the connected fluid volumes and are reflected at geometric discontinuities such as muffler walls and chamber boundaries, producing oscillating pressure variations that persist into the next phase of the cycle. Direct measurements in the suction chamber captured the consequence [3]. The temperature oscillations observed with the suction valve closed arise from these pressure waves, not from slow thermal equilibration with the walls. This causal chain (valve event, pressure wave, temperature oscillation in the suction chamber) connects the valve dynamics described in this section to the non-stationary superheating characterised in Section 1.4, and underlines why the two phenomena cannot be treated in isolation.

The self-acting valves open and close once in each revolution. This forces periodic gas pulsations in the suction and discharge lines (Figure 1.9). The pulsations couple to the acoustic resonances of those lines. They can then amplify the pressure fluctuation far beyond the kinematic forcing [34], [35].

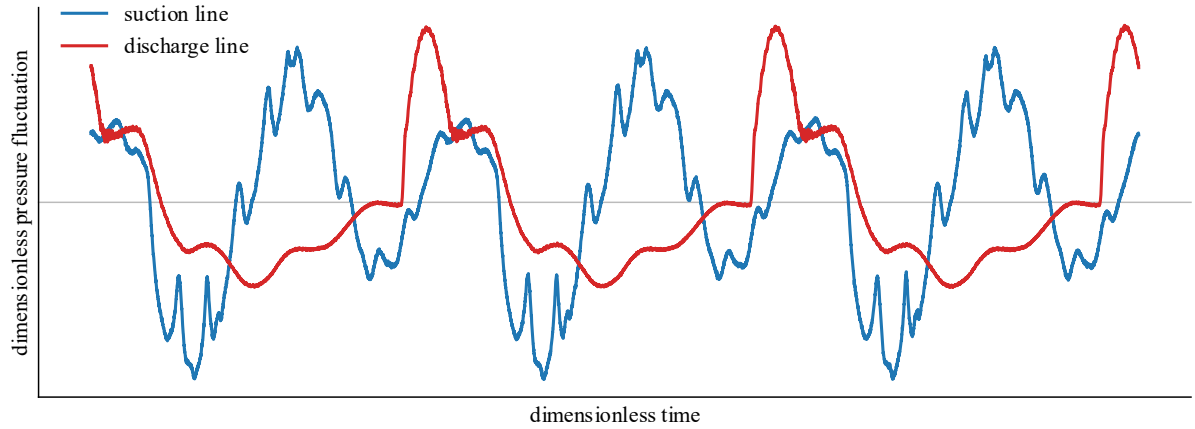

Figure 1.9 Measured pressure fluctuation in the suction and discharge lines over a few revolutions. Both axes are dimensionless. The traces show the periodic pulsation forced by the valves and the acoustic oscillation it carries.

A chamber with a connecting neck behaves as a Helmholtz resonator. A long line behaves instead as a distributed system. Its standing-wave modes follow from the one-dimensional wave equation. A line that is open at one end and closed at the other resonates at its quarter-wave frequency and the odd harmonics of it [34], [36].

Because the valves act once in each revolution, the forced pulsation is periodic at the shaft frequency and carries its harmonics, the running-speed orders. A line responds strongly when one of these orders falls close to a natural frequency of its gas column, so a pulsation that would be modest under the kinematic forcing alone is amplified by the resonance, and which order dominates then depends on how the orders align with the line modes rather than on the forcing amplitude [29]. A resonant line carries a standing wave with a fixed spatial shape, a pressure antinode at the closed end and a node at the open end, so the pulsation amplitude varies along the line. This mode shape, and not the frequency alone, distinguishes an acoustic resonance from a simple kinematic order, since the two can share the same frequency. These pulsations add to the indicated work and to the radiated noise. They are commonly suppressed by suction and discharge mufflers [34].

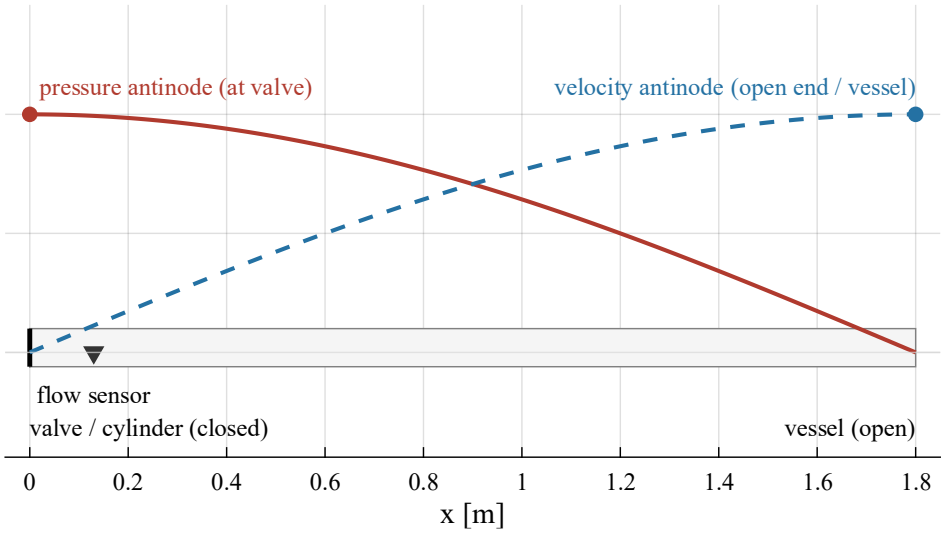

Figure 1.10 The suction line modelled as a quarter-wave resonator, closed at the valve and open at the vessel. The pressure amplitude has an antinode at the valve and the velocity amplitude an antinode at the open end. The quarter-wave frequency $f = c_s/4L_s$ is about 48 Hz, which matches the measured second-order resonance.

The gas velocity through the valve passage during the valve-open period is substantially higher than anything achievable through piston motion alone. Gas velocities of 68 to 71 m/s through the discharge valve channels at the crank angles of peak discharge flow were measured in a three-dimensional fluid-structure interaction (FSI) simulation [37]. These velocities are set by the instantaneous pressure difference and aperture area through the equations above, and they vary continuously throughout the valve-open period as both the pressure difference and the valve lift evolve at the same time. The coupling between the valve plate motion and the flow field acts in both directions. The flow forces on the plate are themselves set by the velocity field that the plate position creates. Full resolution of this fluid-structure interaction requires the simultaneous solution of the structural and fluid equations [37]. In practice, the equations above embody a one-way coupling. The flow is computed from the instantaneous pressure and aperture, while the influence of the flow field on the plate dynamics enters only through the bulk pressure coefficient C_{fs}. This representation is adequate for thermodynamic modelling purposes, as shown by the agreement between predicted and measured p-V diagrams [19], [21].

The direct connection between valve dynamics and in-cylinder heat transfer is that the instantaneous valve mass flow rate sets the characteristic convective velocity in the cylinder during the open-valve phases. During compression and expansion, when the valves are closed, the only flow in the cylinder is driven by piston motion and is well characterised by the mean piston velocity, the basis of all classical Nusselt correlations from Annand [4] through Adair [6]. During suction and discharge, the valve-induced jet flow dominates, and the relevant velocity scale is set by the gas velocity through the valve aperture (equation 1.13). This physical insight motivated separate Reynolds number expressions for the valve-open phases, using the instantaneous valve mass flow rate as the characteristic velocity, in contrast to all preceding correlations that used piston kinematics alone [9].

$$u_{char}(t) = \frac{\dot{m}_{valve}}{\rho \cdot A_{valve}} \tag{1.13}$$

The valve dynamics equations in this section are therefore not just a constructional detail. They are the physical link between the macroscopic thermodynamic state of the compression cycle and the local convective heat transfer that governs compressor efficiency.

1.6 Leakage

Part of the gas trapped in the cylinder escapes before it is delivered. This lowers the volumetric efficiency and wastes the compression work already spent on it. Two paths dominate (Figure 1.11). Gas blows by the piston rings into the crankcase through the radial clearance between piston and cylinder. Gas also leaks back through the suction and discharge valves when they do not seal perfectly. Leakage accounts for about 4 % of the thermodynamic losses, a share that grows with the pressure ratio [2], [38], [39].

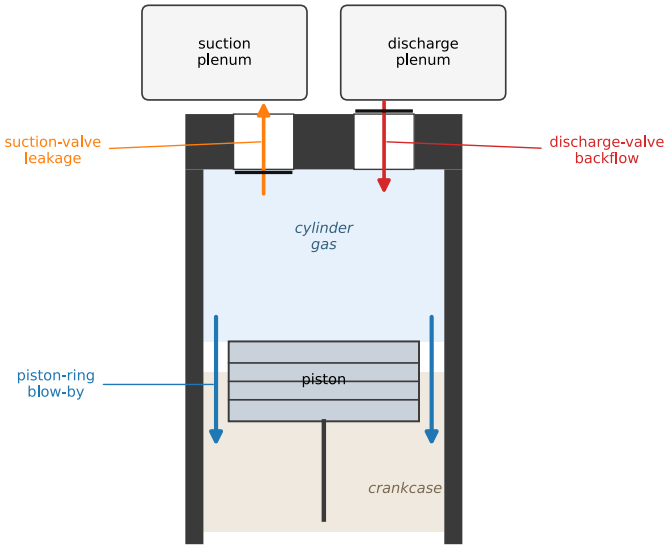

Figure 1.11 The main leak paths in a reciprocating compressor. Gas blows by the piston rings into the crankcase, flows back through the discharge valve during re-expansion, and leaks out through the suction valve during compression.

The piston-cylinder leakage has a direct and an indirect part [40]. The direct part is the gas forced through the clearance by the pressure difference and the piston motion. The indirect part is carried by the lubricating oil. The direct leakage is modelled as a laminar flow through the annular gap between piston and cylinder, treated as a ringless gap [40]. It superposes a shear-driven (Couette) component and a pressure-driven (Poiseuille) component. The leakage depends strongly on the clearance height, the sealing length and the gas viscosity.

Later work refined this model. Gas compressibility cannot be neglected. The secondary lateral motion of the piston also changes the leakage [39]. This motion raises leakage by up to 90 %

[38]. The effect is largest at high pressure ratios. It becomes negligible below a clearance of about 6 μm.

Leakage through the valves is a compressible flow through the valve orifice, driven by the pressure difference across it. It appears mainly as backflow through the discharge valve. This backflow occurs during the re-expansion of the clearance gas. At that moment the discharge-side pressure briefly exceeds the falling cylinder pressure.

2 HEAT TRANSFER IN RECIPROCATING COMPRESSORS

The thermodynamic framework developed in the preceding sections identified in-cylinder heat transfer as the primary driver of superheating, the dominant efficiency loss in this class of machine, and established the valve dynamics that control the flow conditions under which this heat transfer occurs. Although this process has been recognised as a critical factor since the late 1930s, the mechanisms governing it remain surprisingly underexplored from an experimental standpoint.

2.1 Overview and Historical Development

Research on in-cylinder heat transfer in reciprocating compressors spans nearly a century and reflects a recurring tension between empirical correlations calibrated on indirect data and the direct experimental measurement that would test them. This section traces the main milestones, while the individual contributions are analysed in the thematic sections that follow. The earliest treatments were dimensional, relating the HTC to instantaneous pressure, temperature, and piston speed from engine measurements. A quasi-static treatment assumes the heat flux follows the gas-wall temperature difference instantaneously. That assumption was shown to be inadequate early on by measurements that revealed a temporal shift, or phase lag, between the two [41].

During 1960s a family of dimensionless Nusselt correlations was built on internal combustion engine data, differing mainly in their characteristic velocity and length scale [4], [5], [42], [43]. Their transfer to compressors rarely acknowledged the physical differences between the two machines, namely the self-acting reed valves, the absence of combustion, and the resulting different flow. A first explicit dynamic correction, a dT/dt term added to the quasi-static relation, followed soon after [44]. Compressor-specific work began with the first direct measurement in a refrigeration compressor, which gave a compressor correlation that was widely adopted in the two decades that followed [6]. Early simulations suggested the efficiency effect was modest, but they rested on an assumed HTC and called explicitly for experimental validation [25].

Independent evidence soon questioned that early correlation. On a compressor using R12 as a working fluid the same functional form appeared with a leading constant larger by more than an order of magnitude, and a direct numerical solution of the conservation equations gave much higher heat fluxes. [7], [45]. From the late 1980s the field took three parallel directions. System-level thermal modelling showed that the global prediction depends directly on the in-cylinder correlation used as a boundary condition [23]. The first systematic comparison found that the engine-derived Annand correlation [4] outperformed the compressor-specific alternatives [46]. The phase lag received its most rigorous analytical treatment through a complex Nusselt num-

ber validated against gas-spring experiments [47].

The 2000s added computational fluid dynamics (CFD), which resolved the valve-induced flow that governs the open-valve heat transfer [9], [10], [48] and coupled the conjugate heat transfer between the cooling-water circuit and the solid cylinder body, with the gas-side heat transfer imposed as a boundary condition [49]. The most recent decade consolidated around comparative studies and new working fluids. A zero-dimensional comparison of five correlations found predicted efficiencies differing by up to 30 %, while none had been validated against measured in-cylinder heat flux [11]. A conjugate heat transfer simulation of an ionic liquid-piston compressor found that the Annand, Woschni and Disconzi correlations all underpredict the in-cylinder heat transfer relative to CFD, with the Annand form the highest of the three [50].

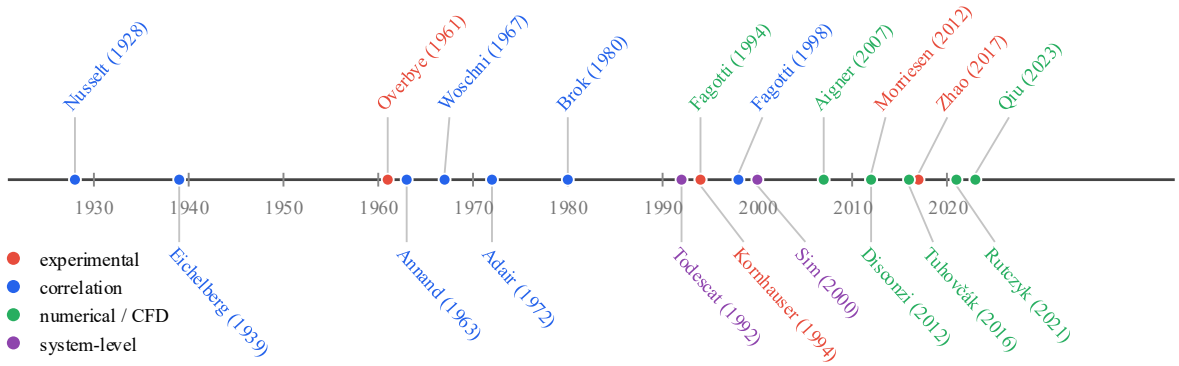

Figure 2.1 Timeline of the principal milestones in compressor heat transfer research, 1928–2023, colour-coded by approach.

The principal milestones are summarised in Fig. 2.1. Taken as a whole, this history shows a field that has produced an extensive body of correlations and comparative studies while consistently deferring the experimental ground truth that would allow them to be ranked with confidence.

2.2 System-Level Thermal Analysis

Compressor heat transfer is most usefully understood not as a set of isolated local processes but as the behaviour of a thermally coupled system. The working fluid exchanges heat with every component along its path, from the suction muffler through the suction chamber and cylinder to the discharge side. The superheating of the suction gas is therefore not solely a product of in-cylinder heat exchange. It is the cumulative result of heat gained at several stages along the suction path, each set by the temperatures of the surrounding components, which are in turn governed by the heat released during compression and discharge. Mapping this temperature distribution and the heat flows between components is a prerequisite for identifying where superheating losses can be reduced.

System-level analysis treats the compressor as a network of control volumes, each with an energy balance, coupled through overall thermal conductances, and solves for the steady-state

temperature distribution. This trades spatial resolution within a component for the ability to model the machine as an integrated thermal system. A critical survey distinguished three classes of approach [2]. Integral models apply lumped balances to control volumes linked by conductances. Hybrid models treat conduction in the solids differentially and the fluid integrally. Fully differential CFD removes the need for prescribed coefficients at a much higher cost. The route judged best for design is a combination of numerical models and experiment, each compensating for the limitations of the other [2].

The integral approach was first applied to a hermetic refrigeration compressor, dividing it into control volumes (Fig. 2.2) and solving a coupled set of steady-state energy balances [23]. The gas-to-wall heat exchange is taken from existing in-cylinder correlations, and the solid-to-solid conductances are fitted to measured temperatures. The model agreed well with experiment. Its accuracy depends directly on the in-cylinder correlation used as a boundary condition, because an error there propagates through the whole network.

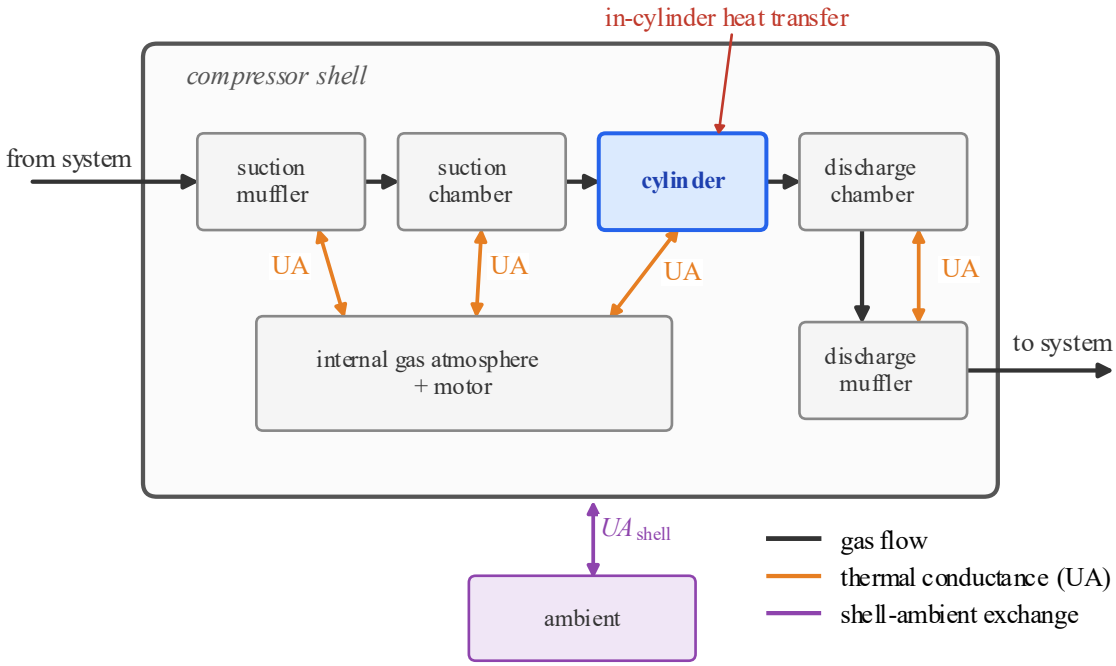

Figure 2.2 Thermal network of a hermetic compressor. Control volumes are coupled by thermal conductance (UA) [23]. In-cylinder heat transfer enters as the boundary condition supplied by a Nusselt correlation.

The framework was later extended to include motor losses and the mechanical heat of compression [27]. A parametric study drew attention to a quantity rarely considered in in-cylinder work, the fraction of suction gas that passes directly through the muffler against the fraction that recirculates within the shell before entering the suction path. This mixing fraction has a first-order effect on the suction gas temperature, yet it is a flow-geometric quantity that in-cylinder measurements alone cannot supply [27]. The thermal environment seen by the gas before it enters the cylinder is itself a function of the global thermal balance.

A later model paired thermocouple measurements at multiple internal locations with a lumped-parameter model whose coefficients came from classical correlations rather than from calibra-

tion, which highlighted the lubricating oil as a heat-transfer medium that redistributes heat between motor, cylinder, and shell [51]. A finer twelve-volume network resolved the oil and inner-gas control volumes [52], and a two-part energy-balance model tracked compressor efficiency and temperatures through the on-off transients of a refrigeration system [53].

A hybrid model combined a differential treatment of conduction in the solids with an integral treatment of the fluid, gaining spatial fidelity while avoiding a full three-dimensional flow solution. With in-cylinder correlations as the fluid-side boundary condition, the choice of correlation set the predicted temperatures throughout the solid parts of the compressor, not only at the cylinder wall [54].

A systematic decomposition of the overall efficiency into its physical sub-processes quantified the contribution of each across a range of conditions [22]. Superheating losses were a major contributor to the thermodynamic inefficiency, which confirms the central motivation for detailed in-cylinder work. Changes in geometry, valve characteristics, and clearance volume affected the loss components in coupled and often counterintuitive ways.

A system-level thermal model of a hermetic compressor selected HTCs for the individual control volumes from literature correlations and adjusted them against measured temperatures, reaching agreement within ±20% [55]. The external thermal state of the running compressor is shown as an example in Fig. 2.3, where the cylinder head is markedly hotter than the crankcase.

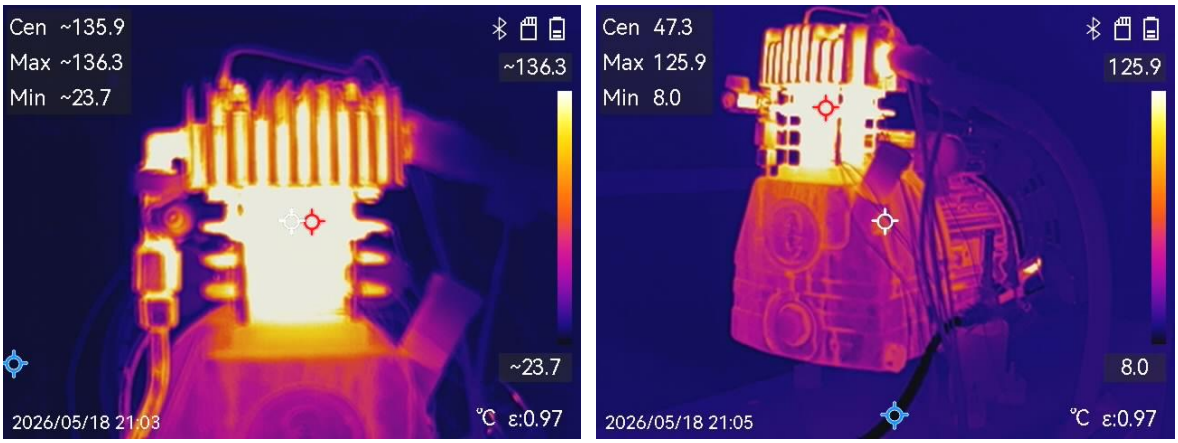

Figure 2.3 Thermal-camera images of the running compressor, (a) in detail and (b) zoomed out view. The finned cylinder head reaches about 136 °C while the crankcase stays near 47 °C. The images show the heat path from the hot gas through the cylinder wall and head to the surroundings.

2.3 In-Cylinder Heat Transfer

The system-level analysis reviewed in the preceding section treats the cylinder primarily as an energy balance boundary, a component exchanging heat with surrounding structures via conductances calibrated against experimental data or estimated from correlations. This treatment is adequate for predicting the global thermal profile of the compressor but not sufficient for understanding the physical mechanisms that govern superheating and determine thermodynamic efficiency. For this purpose, attention must be directed to the cylinder interior, where

the working fluid undergoes the compression cycle in direct thermal contact with the surrounding solid surfaces under conditions that are transient, three-dimensional, and strongly coupled to the instantaneous state of the valves and the thermodynamic state of the gas.

The in-cylinder heat transfer process is characterised above all by its variability throughout the cycle. Both the direction and the magnitude of the local heat flux change several times during each cycle, as shown schematically in Fig. 2.4. During early compression the gas is cooler than the wall and heat flows into the gas. As the gas temperature rises above the wall temperature, the flux reverses. Discharge creates intense local convection in the narrow clearance between piston and valve plate, expansion reverses the flux once more, and during suction the warm walls again heat the fresh charge. The mean HTC increases markedly with rotational speed and pressure ratio [56]. The mean heat flux in each cycle, however, decreases with increasing rotational speed. This counterintuitive result is explained by the shorter time available for heat exchange at higher speeds, and it has direct implications for how the operating conditions affect the severity of superheating.

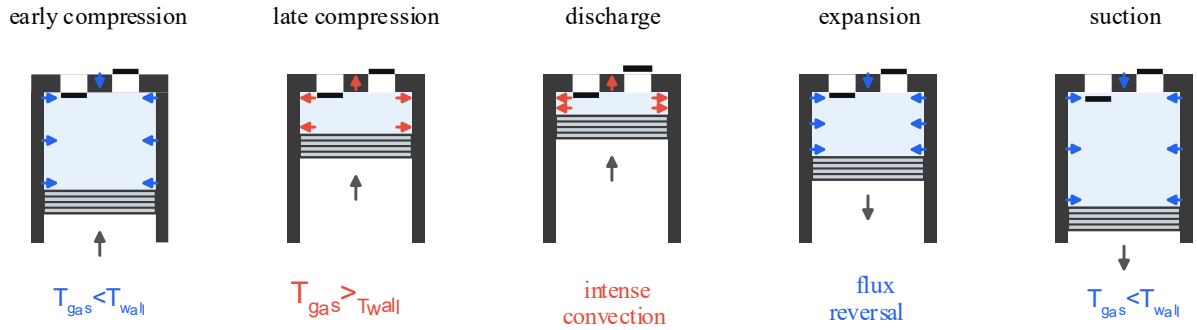

Figure 2.4 Direction of the in-cylinder heat flux through the five phases of the cycle (schematic).

The heat transfer does not occur uniformly across the compression chamber walls but at multiple surfaces with distinctly different characteristics (Fig. 2.5). The cylinder wall presents the largest surface area and generally makes the dominant contribution to the total heat exchange over a complete cycle. Its temperature varies along the axial direction, higher near the valve plate, where the gas reaches its highest temperatures during the discharge process, and lower near the bottom dead centre. The valve plate is an additional wall at the top of the compression space. During discharge, when the piston is close to top dead centre, the gas between the two surfaces is accelerated to very high velocities, creating locally intense convective heat transfer at the valve plate surface that substantially exceeds the rates on the cylinder wall. The piston surface represents a moving boundary whose thermal contribution varies continuously with its position. During discharge, when the piston is closest to the valve plate, the small clearance accelerates the gas and substantially increases the heat transfer at both surfaces simultaneously. The instantaneous heat flux differs between these surfaces not only in magnitude but also in direction at a given crank angle, particularly during the valve-open phases [10]. During the discharge process the heat flux at the cylinder wall is substantially lower than at the piston and valve plate surfaces, because as the piston approaches the valve plate the area of cylinder wall exposed to high-velocity clearance flow diminishes [48]. The piston and valve plate surfaces

then carry the dominant heat transfer load.

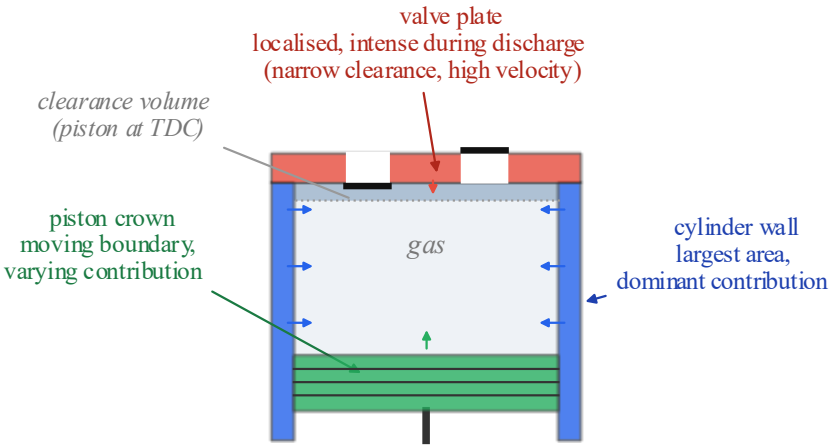

Figure 2.5 Heat transfer surfaces of the compression chamber, namely the valve plate, the cylinder wall, and the piston crown (schematic).

Underlying these differences is the fact that the gas is not at a single temperature. A cool layer next to the wall sits below a much hotter core, and three-dimensional simulations place the instantaneous liner flux several times below the piston and the valve plate. When the charge is compressed or expanded quickly the wall-adjacent gas cannot follow the bulk in time and can even drive heat against the bulk temperature difference, so a single convective coefficient loses its usual sign and meaning [14], [45], [48], [57], [58].

The most physically significant, and most practically challenging, feature of in-cylinder heat transfer is the role of valve-induced flow. During the closed-valve phases of the cycle, the flow within the cylinder is driven solely by the piston motion. The resulting convective velocities are moderate and relatively well described by kinematic parameters such as the mean piston speed. This is the basis on which the classical correlations [4], [5] were constructed and later adopted for compressors. When the valves open, the situation changes dramatically. During suction, the incoming gas jet is deflected by the valve reed, flows along the valve plate, and then redirects toward the cylinder wall before reaching the piston surface, at each stage creating convective heat transfer rates substantially higher than those achievable through piston motion alone. During discharge, the gas accelerating through the diminishing clearance between the approaching piston and the valve plate generates high-velocity flow that creates similarly intense localised heat transfer. Ignoring this valve-induced flow leads to substantial underprediction of heat transfer, particularly during discharge [48]. The contribution of the piston surface to the total heat transfer during suction decreases along the flow path, because the gas is progressively heated by the valve plate and the cylinder wall before it reaches the more distant piston. All classical kinematic correlations, including those designed for compressors, substantially underestimate heat transfer during suction because they lack any mechanism to represent valve-induced flow enhancement [9]. CFD that resolves the independent motion of each valve plate together with the transient internal flow, using a fluid-structure interaction formulation, shows the full complexity of the coupling between the valve dynamics and the chamber flow

field [37]. The consequences of this coupling for heat transfer cannot be captured by single-equation kinematic correlations.

The dynamic character of in-cylinder heat transfer is not confined to the cylinder itself. Measured suction-chamber gas velocities are far higher during valve opening than in the closed-valve state, as set out in Section 1.5 [3]. A quasi-static treatment of the suction chamber is therefore physically inadequate, and instantaneous heat transfer in this chamber contributes to the overall thermodynamic losses, extending the physical picture presented in this section to the immediate upstream environment of the compression space.

A further effect that clearly separates in-cylinder heat transfer from steady-state convection is the phase lag between the bulk gas-wall temperature difference and the resulting heat flux at the surface, illustrated in Fig. 2.6. Because the gas temperature cannot respond instantaneously to the boundary conditions imposed by compression and expansion, the heat flux does not simply follow the instantaneous temperature difference. The temporal shift between the two quantities varies throughout the compression cycle and can produce physically counterintuitive results.

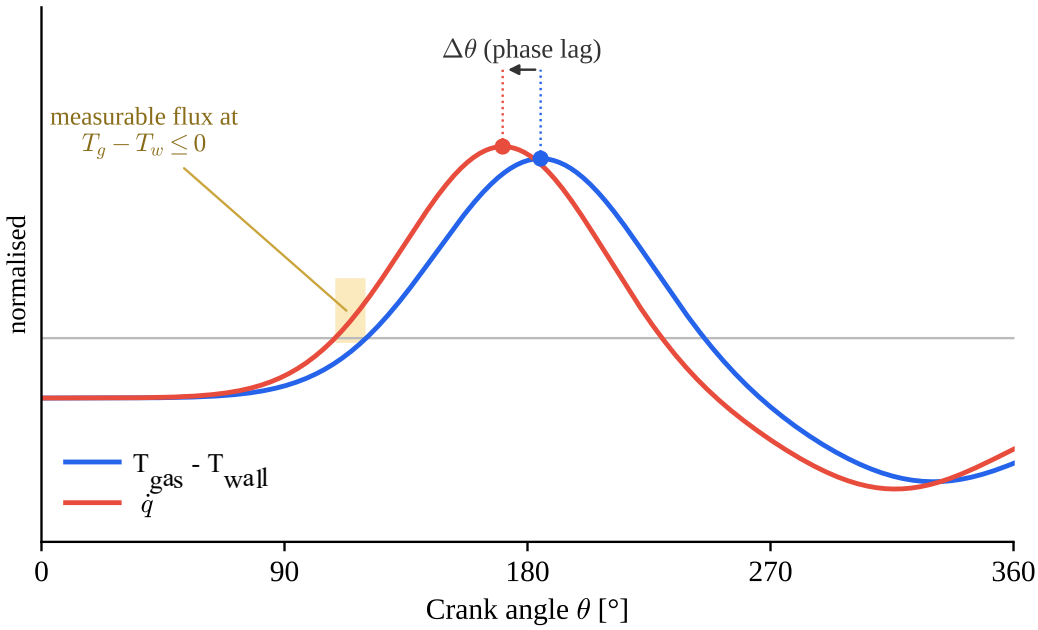

Figure 2.6 Phase lag between the gas-to-wall temperature difference and the heat flux (schematic, lag exaggerated). The peak flux precedes the peak ΔT by approximately 8° [14]. A measurable flux persists where $\Delta T \leq 0$.

The phase lag is well documented in many reciprocating machine measurements. Direct heat flux measurements in internal combustion engine (ICE) cylinders show four consistent features [41]. The heat flux during compression substantially exceeds that during expansion. The maximum occurs approximately 8° before top dead centre. A measurable flux is present even when the gas and wall temperatures are momentarily equal. During expansion, heat flows from the wall to the gas even when the bulk gas temperature exceeds the wall temperature. These effects are attributable to the volumetric rate of compression and expansion rather than the instantaneous temperature difference alone [14]. Adding a term proportional to the time derivative of the

bulk mean gas temperature addresses this limitation in the static formulation [44], and the inadequacy of quasi-static interpretations has been confirmed across multiple diesel engine configurations [59].

The most rigorous analytical treatment of the lag decomposes the heat flux into a component proportional to the gas-wall temperature difference and a component proportional to the rate of change of gas temperature, both expressed through a complex HTC [47].

In the compressor context, the phase shift appears as a systematic residual in correlation predictions near the transition between compression and discharge. A discrepancy between measured heat flux and correlation predictions at this transition comes from the phase shift, which a real-valued Nusselt correlation cannot represent [8].

Characterising the instantaneous HTC from a measured heat flux requires the instantaneous bulk gas temperature as the reference for the wall temperature. This temperature cannot be measured directly, because thermocouples in the gas stream are too slow to follow the rapid changes of the compression cycle and the valve events. The choice of gas-temperature reference therefore affects the calculated coefficient strongly, most of all near the crank angles where the gas-to-wall temperature difference passes through zero.

The work reviewed in this section defines the challenge that any predictive correlation must address. The heat transfer process is three-dimensional and highly transient. It is dominated by valve-induced flow during the open-valve phases. It shows a lag between the temperature difference and the heat flux that standard quasi-static correlations are structurally incapable of representing. It also depends on a gas reference temperature that is itself difficult to measure.

2.4 Heat Transfer Correlations

The phenomena defined in the preceding section must be addressed by any predictive model. Direct simulation of the three-dimensional transient flow field is too expensive for design or simulation use, so the field has historically relied on empirical correlations that reduce heat transfer to a tractable algebraic expression. This section presents the principal correlations in the literature.

Most published correlations express the instantaneous convective HTC through a Nusselt number of the general form:

$$Nu(\theta) = a \cdot Re(\theta)^b \cdot Pr(\theta)^c \tag{2.1}$$

$$Nu = \frac{h \cdot D}{\lambda} \tag{2.2a}$$

$$Re = \frac{\rho \cdot u \cdot D}{\mu} \tag{2.2b}$$

$$Pr = \frac{c_p \cdot \mu}{\lambda} \tag{2.2c}$$

The constants a, b, c and the definitions of u and D distinguish the individual correlations. Gas properties are evaluated at the instantaneous bulk conditions, making the correlations implicitly time-dependent through the gas state. The wall heat flux follows from Newton's law of cooling:

$$q(\theta) = h(\theta) \cdot \left(T_{gas}(\theta) - T_{wall}\right) \tag{2.3}$$

The wall temperature is usually assumed constant since the within-cycle wall variation is below ±0.56 K [6].

The Annand correlation [4], from heat transfer measurements in internal combustion engines, takes the form:

$$Nu = a \cdot Re^{0.7} \tag{2.4}$$

The Reynolds number uses the mean piston speed as the characteristic velocity and the bore as the characteristic length. The constant a lies in the range 0.35 to 0.8 depending on charge motion intensity, with 0.7 the standard reference in compressor work [4], [11]. The Reynolds number is commonly replaced by the Péclet number, giving the explicit form (Equation 2.4b) used in compressor studies. The radiation term of the original formulation is neglected in compressors, where gas temperatures are far below those in fired engines. The defining limitation of Annand in the compressor context is the mean piston speed as the sole characteristic velocity. It captures piston-driven flow but has no mechanism for the enhanced convection from valve-driven flow during suction and discharge.

$$Nu = 0.7 \cdot Re^{0.7} \cdot Pr^{0.7} \tag{2.4b}$$

The Woschni correlation [5] addresses the mean-piston-speed limitation through a phase-dependent characteristic velocity:

$$Nu = 0.035 \cdot Re^{0.8} \tag{2.5}$$

The Reynolds number is based on the bore and a characteristic velocity defined differently for the gas exchange and closed-valve phases [5].

$$u_{char} = 6.18 \cdot \bar{u}_p \ (gas\ exchange),\ u_{char} = 2.28 \cdot \bar{u}_p \ (closed\ valves) \tag{2.5b}$$

The compressor form of the Woschni correlation, with its phase-dependent characteristic velocity, has been fitted to a single operating point and then used to predict isentropic and volumetric efficiencies across several working fluids [60]. It recognised that in-cylinder flow intensity changes strongly between valve-open and valve-closed phases, an insight later borne out, although the coefficients were calibrated for combustion engines with cam-driven valves, high combustion-generated turbulence, and flow patterns unlike those in compressors. The large gap in the leading constant between Woschni (0.035) and Annand (0.7) reflects their very different

characteristic velocities, so the two predict comparable Reynolds numbers and heat transfer rates despite the apparent difference [11]. Even in their original engine context, both fail to predict the history and peak of the heat flux, with the largest discrepancies during expansion [59].

A modification of Woschni argued that it overestimates the coefficient during combustion and underestimates it during compression [61]. Retaining the dimensional form but adjusting the volume exponent and adding a constant offset to the velocity term, it can be written as:

$$h_c \propto {p_c}^{0.8} \cdot {T_c}^{-0.4} \cdot {u_{char}}^{-0.06} \cdot \left(\bar{u}_p + 1.4\right)^{0.8} \tag{2.6}$$

The 1.4 m/s offset keeps the coefficient finite at zero piston speed. In a parametric study of a CO_2 reciprocating compressor, Hohenberg [61] follows Woschni and Annand during compression and expansion but differs substantially during discharge, where the velocity formulations matter most [56].

The Adair correlation, from direct measurements in a reciprocating compressor cylinder head, takes the form:

$$Nu = 0.053 \cdot Re^{0.8} \cdot Pr^{0.6} \tag{2.7}$$

The Reynolds number uses a characteristic length from the instantaneous cylinder volume and surface area (Equation 2.7b). The characteristic velocity comes from the crankshaft angular speed and combines a piston motion component with a crank-angle-dependent swirl component, following previous studies [43]. The characteristic length is an instantaneous equivalent diameter:

$$D_e(\theta) = \frac{6V(\theta)}{A(\theta)} \tag{2.7b}$$

This length scale varies continuously with crank angle, rising from a minimum near top dead centre, where the volume is small and the area relatively large, to a maximum near bottom dead centre. The variation captures the spatial confinement as the piston nears the valve plate. The correlation came from a single fast-response thermocouple in the head and correlated time-averaged data within ±20%. Despite this uncertainty it became and remains the standard compressor-specific reference.

The characteristic velocity is the tangential swirl velocity rather than the piston speed. From motored-compressor measurements, the swirl angular velocity was approximated as roughly twice the crankshaft speed around bottom dead centre, where suction-induced swirl is strongest, and half that elsewhere [6]:

$$\omega_g(\theta) = \begin{cases} 2\omega[1.04 + cos(2\theta)] & for\ \pi/2 \leq \theta \leq 3\pi/2 \\ \omega[1.04 + cos(2\theta)] & otherwise \end{cases} \tag{2.7c}$$

A modification of Adair reduced the constant in the swirl velocity expression from unity to 0.5,

giving better agreement between simulation and experiment for open-type refrigerant compressors [25]. Though numerically minor, it was the first calibration of Adair against independent data from a different compressor, which suggests the original constants may have been geometry specific.

A different approach applied the Dittus-Boelter turbulent pipe flow correlation directly to the cylinder, treating the in-cylinder flow as fully developed turbulent pipe flow with the bore as the characteristic length [62]. This neglects the oscillatory nature of piston-driven flow, the absence of a developed velocity profile in the short cylinder, and the transient character of valve-induced flow. It produces almost no predicted heat transfer over the cycle, a consequence of the very low characteristic velocities it implies [46]. It is kept for completeness as a lower bound that shows the consequences of an inappropriate physical analogy.

A further approach analytically solved the continuity and energy equations in the one-dimensional thermal boundary layer at the gas-wall interface, valid for small volume modulation [63]. The instantaneous wall heat flux is:

$$q(t) = \frac{\pi\lambda/l_{th} \cdot \delta_T \cdot T \cdot F \cdot cos(\omega t + \psi) + (T_{gas} - T_{wall})/l_s}{1 + \delta_v \cdot cos(\omega t)} \tag{2.8}$$

where l_{th} (2.8a) is the thermal penetration depth, F a dimensionless function of the ratio (2.8b) between hydrodynamic and thermal boundary layer thicknesses, ψ the phase angle between temperature difference and heat flux, δ_T the temperature modulation (2.8c), δ_v the relative volume modulation, and T_0 the reference gas temperature. This was the first compressor correlation to incorporate a phase lag explicitly. The derivation assumes small sinusoidal volume modulation, a geometry-specific wall area variation, and a simplified one-dimensional boundary layer, which limit its general applicability. In a compressor code it produced physically impossible negative heat transfer conductance under some conditions [46].

$$l_{th} = \sqrt{\frac{2\alpha}{\omega}} \tag{2.8a}$$

$$\xi = \frac{l_t}{l_{th}} \tag{2.8b}$$

$$\delta_T = (\kappa - 1) \cdot \delta_v \tag{2.8c}$$

The Liu correlation [7] came from wall temperature distribution measurements in a R12 refrigeration compressor across pressure ratios, suction temperatures, speeds, and axial locations. It takes the form:

$$Nu = 0.75 \cdot Re^{0.8} \cdot Pr^{0.6} \tag{2.9}$$

It is identical in form to Adair but with a constant more than an order of magnitude larger. The key difference is the characteristic length (Equation 2.9b).

$$D_e = \frac{3D \cdot S}{2S + D} \tag{2.9b}$$

This is a fixed geometric parameter rather than an instantaneous quantity as in Adair. The difference is physically significant. Adair's length (2.7b) varies continuously, approaching zero near top dead centre and amplifying predicted heat transfer near the valve plate. Liu's (2.9b) is constant and reflects the average confinement at bottom dead centre. The two therefore diverge in both their constants and their crank-angle dependence. The unexplained order-of-magnitude gap in constants, with this difference in length definition, has prevented consensus on which, if either, represents physical reality.

The Hsieh correlation [8] came from a high-pressure two-stage reciprocating gas compressor at pressures up to 41.3 MPa, where the pressure dependence of gas transport properties is significant. It takes the form:

$$Nu = (C_1 \cdot Re_1 + C_2 \cdot Re^{C_3}) \cdot \left(\frac{\mu}{\mu_0}\right)^{C_4} \tag{2.10}$$

The normalised viscosity ratio is referenced to nitrogen at standard conditions, and the extra Reynolds number term, based on the piston velocity at the start of discharge, captures the enhanced gas velocity during compression with discharge. Separate constants are given for each phase. A phase shift between the gas-wall temperature difference and the heat flux was noted in the data at the start of expansion [8].

The quasi-static assumption shared by this early period was first challenged at the correlation level by adding a term proportional to $\mathrm{d}T_{gas}/\mathrm{d}t$ to account for the phase lag [44]. In later diesel-engine measurements this additive correction gave substantially better agreement with the directly measured heat flux [14].

The Fagotti [58] correlation addresses the phase lag in the correlation structure by adding the time derivative of the mean gas temperature to the driving force (Equation 2.11), following previous publications[14], [44], [47].

$$q(\theta) = h \cdot \left[\left(T_{gas}(\theta) - T_{wall}\right) + \tau \cdot \frac{dT_{gas}}{dt}\right] \tag{2.11}$$

τ is a calibrated time constant for the thermal response of the gas. The distinction from Kornhauser [47] is methodological. Here the time constant was calibrated against a finite volume CFD simulation of the two-dimensional transient flow in a hermetic compressor rather than derived analytically from gas spring experiments [58]. Validated against global performance data with improved agreement over quasi-static approaches, it encodes the dynamic gas-wall interaction at the correlation level, though the reliance on CFD calibration rather than direct heat flux measurements remains a fundamental limitation.

The Disconzi correlation [9], from two-dimensional CFD simulations with coupled reed valve dynamics for a hermetic refrigeration compressor, is a four-phase formulation with a separate

Reynolds number for each phase (Table 2.1). For the closed-valve phases, compression (Equation 2.12a) and expansion (Equation 2.12c), the characteristic velocity comes from the instantaneous piston speed. For the valve-open phases, discharge (Equation 2.12b) and suction (Equation 2.12d), it is a power-law combination of the mean piston speed and an instantaneous valve velocity. That valve velocity characterises the flow through the valve passage and equals the instantaneous valve mass flow rate divided by local gas density and valve passage area.

The Stanton number (Equation 2.13) was adopted as the primary heat transfer parameter from full three-dimensional CFD simulations with explicit valve dynamics [10]. Separate Stanton values were derived for each chamber surface and each phase. This surface-specific, phase-resolved treatment is the most physically detailed in the compressor literature, capturing both spatial non-uniformity across surfaces and variation through the cycle. It demands twelve Stanton values from CFD of specific geometries, so generalisation depends on new simulations.

$$St = \frac{Nu}{Re \cdot Pr} \tag{2.13}$$

Table 2.1 Phase-specific Reynolds number definitions of the Disconzi correlation [9]

Process	**Reynolds Number**		**Constants (Equation 2.1)**
Compression	$Re = \frac{\rho(\tau) D \bar{u}_p}{\mu(\tau)}$	$(2.12a)$	a = 0.08 b = 0.8 c = 0.6
Discharge	$Re = \frac{\rho(\tau) D (\bar{u}_p + \bar{u}_p{}^{0,8} u_{char}(\tau)^{0,2})}{\mu(\tau)}$	$(2.12b)$	a = 0.08 b = 0.8 c = 0.6
Expansion	$Re = \frac{\rho(\tau) D \bar{u}_p}{\mu(\tau)}$	$(2.12c)$	a = 0.12 b = 0.8 c = 0.6
Suction	$Re = \frac{\rho(\tau) D (\bar{u}_p + 2\bar{u}_p{}^{-0,4} u_{char}(\tau)^{1,4})}{\mu(\tau)}$	$(2.12d)$	a = 0.08 b = 0.9 c = 0.6

Heat transfer in small fast-running piston compressors was studied through full three-dimen-

sional CFD of four valve configurations [57]. Rather than an analytical correlation, the work showed that the size, distribution, and shape of the inlet and outlet ports strongly influence the heat flux distribution in ways that vary between configurations and cannot be captured by any correlation based on piston kinematics or global valve mass flow rate alone. This exposes a fundamental limit of all single-formula approaches. When valve geometry departs from the calibration configurations, predictive validity is lost in ways that constant adjustment cannot correct.

Kornhauser [47] proposed a very different approach using complex Nusselt number model (Equation 2.15). The approach addresses the phase lag limitation at the level of the correlation's mathematical structure.

$$q(\theta) = h_r \cdot \left(T_{gas} - T_{wall}\right) + h_i \cdot \frac{dT_{gas}/dt}{\omega} \tag{2.14}$$

Where h_r and h_i are the real and imaginary parts of a complex HTC, and the second term the heat flux component driven by the rate of change of gas temperature. Both components are expressed through a complex Nusselt number (2.15) correlated against an oscillation Péclet number (2.16). The formulation was shown consistent with the semi-empirical dT/dt modifications [14], [44]. Unlike Fagotti [58], which calibrates the derivative term against CFD, it is derived analytically from gas conduction theory. It was validated against pressure-volume measurements from gas-spring apparatus over a wide range of speeds, pressures, gases, and geometries, and correlated both the magnitude and the phase of the measured heat transfer. Its limited adoption reflects mainly the difficulty of obtaining the instantaneous rate of change of gas temperature, not any deficiency in its physical basis.

$$Nu_c = Nu_r + i \cdot Nu_i \tag{2.15}$$

$$Pe_\omega = \frac{\omega \cdot D^2}{4\alpha_{gas}} \tag{2.16}$$

The correlations differ along three criteria that determine their physical applicability. These are the characteristic velocity, the treatment of valve-open phases, and the representation of the phase lag. Table 2.2 summarises these for the five correlations evaluated in the present work.

On the first criterion, Annand [4] and Woschni [5] use variants of the mean piston speed. Adair [6], Brok [25], and Liu [7] use velocities from the crankshaft angular speed with different length definitions. Hohenberg [61] modifies Woschni with an offset velocity term. Only Disconzi [9] and Aigner [10] explicitly include the valve flow, through the instantaneous mass flow rate or CFD-derived surface Stanton numbers. These velocity definitions are compared over the cycle in Fig. 2.7.

Table 2.2 Structural characteristics of the heat transfer correlations evaluated in this work

Correlation	Form	Char. velocity	Dynamic features	Basis
Annand (1963)	$Nu = a \cdot Re^{0.7}$ (2.4)	$\bar{u}_p$	—	ICE exp.
Woschni (1967)	$Nu = 0.035 \cdot Re^{0.8}$ (2.5)	$\bar{u}_p$	Coeff. change at valve open	ICE exp.
Adair (1972)	$Nu = 0.053 \cdot Re^{0.8} \cdot Pr^{0.6}$ (2.7) *	ω-based + swirl	—	Compr. exp.
Disconzi (2012)	$Nu = a \cdot Re^{b} \cdot Pr^{c}$ (2.12)	$\bar{u}_p$ + $u_{char}(\dot{m})$	$u_{char}(\dot{m})$ in Re	CFD (2D)
Aigner (2007)	$St\ for\ each\ surface\ and\ phase$	CFD-derived	CFD-resolved	CFD (3D)

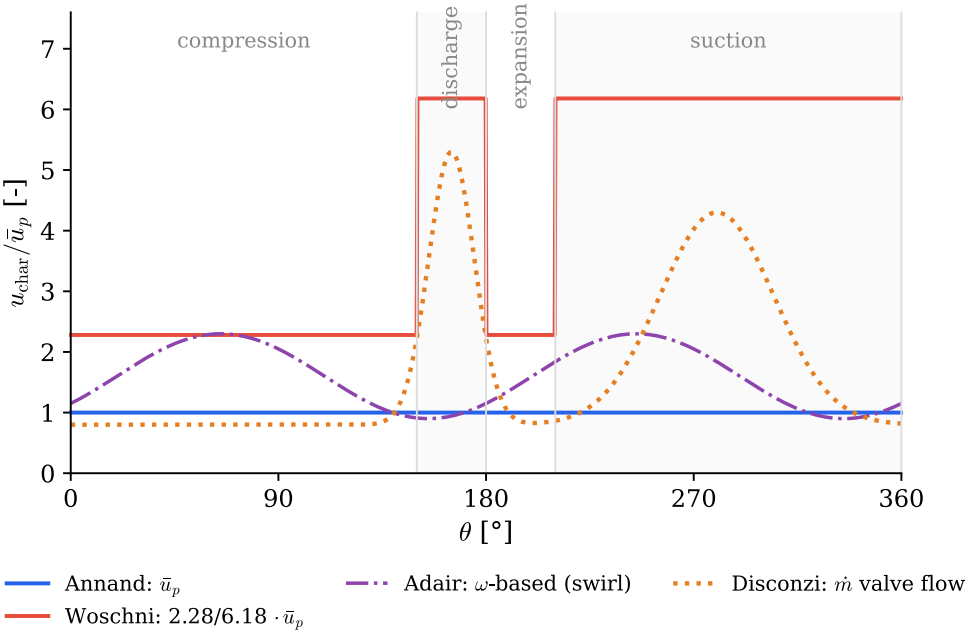

Figure 2.7 Characteristic velocity definitions of the principal correlations over one cycle (schematic phase boundaries).

On the second criterion, all correlations except Disconzi [9] and Aigner [10] fail to represent the change in dominant flow mechanism at valve opening. Hsieh [8] addresses it partly through phase-specific constants without changing the velocity definition.

On the third criterion, all quasi-static correlations cannot represent the phase lag. Among compressor specific correlations only Polman [63] embedded a phase angle explicitly, in a con-

strained form. Fagotti [58] added a derivative term calibrated against CFD. Kornhauser [47] gave the most rigorous treatment through the complex Nusselt number framework validated against direct gas-spring measurements.

These structural distinctions, not just differences in constants, are the main source of the large disagreements between correlations documented in the comparative studies reviewed next, and they define the physical questions any experimental validation campaign must address.

2.5 Numerical Comparison of Correlations

The structural differences between correlations in characteristic velocity, valve-open phase treatment, and phase lag have direct consequences for predicted compressor performance. This section reviews the comparative studies that quantified these consequences.

Six correlations were compared against measured component temperatures from a small hermetic refrigeration compressor across six operating conditions [46]. Four were disqualified on physical grounds, leaving Annand [4] and Adair [6] as viable candidates. Liu [7] gave the smallest wall-temperature deviation yet produced physically impossible negative cylinder conductances at most conditions because of a discontinuity in its swirl velocity expression. It was discarded despite its superior temperature predictions.

Polman [63] was excluded for the same negative-conductance reason. Brok [25] gave results nearly identical to Adair, confirming their shared structure offers no independent predictive capability. Hamilton [62], based on the Dittus-Boelter pipe-flow form, produced almost no heat transfer over the cycle and was rejected as unphysical.

Annand gave the best overall agreement. An engine correlation outperforming all compressor-specific alternatives was an early signal that compressor-specific research had not yet produced a reliably superior model. A transient model of compressor startup and shutdown also adopted the Annand correlation for the in-cylinder heat transfer, after it had been validated against measured component temperatures in earlier studies [9].

A different approach used a two-dimensional CFD simulation with coupled reed valve dynamics as the reference against which classical correlations were evaluated [9]. Disagreement concentrated in the valve-open phases. During discharge, Annand and Liu returned the highest heat flux and Adair and Woschni the lowest. During suction, all four classical correlations substantially underestimated the heat flux, because kinematic correlations contain no valve-induced flow enhancement. The heat transfer decomposition by process showed why this matters. The net heat transferred to the gas during suction was 10.2 W, against 4.2 W from the gas to the walls during discharge. Accurate suction-phase prediction is therefore the dominant requirement for assessing gas superheating, and all classical correlations are structurally deficient in exactly this phase. The correlation was validated across two refrigerants, three speeds, and three pressure conditions.

The most complete comparative study implemented five correlations in a zero-dimensional

first-law model [11]. The comparison spanned four working fluids at two wall temperatures and two inlet gas temperatures.

All five correlations behaved similarly during compression and expansion, where piston motion dominates the flow. They diverged most during suction and discharge. Disconzi consistently predicted the highest suction heat flux and the highest temperature at the start of compression, a direct consequence of its valve-mass-flow-based characteristic velocity. The maximum spread in predicted isentropic efficiency between correlations reached 30.4% at the higher wall temperature. The full comparison for both fluids is shown in Fig. 2.8.

Adair showed the weakest sensitivity to wall temperature, attributed to its crankshaft-angular-speed characteristic velocity and instantaneous equivalent diameter [11]. The Aigner approach requires Stanton numbers calibrated against CFD of specific geometries, so applying it to other configurations without recalibration adds uncertainty.

A change of wall or inlet gas temperature affects compressor efficiency more than the choice of correlation, which shows the importance of accurate thermal boundary conditions [11]. Efficiencies were almost unaffected by speed over the range examined. The accuracy of the available correlations had not been experimentally verified because of the complexity of the required measurement setup.

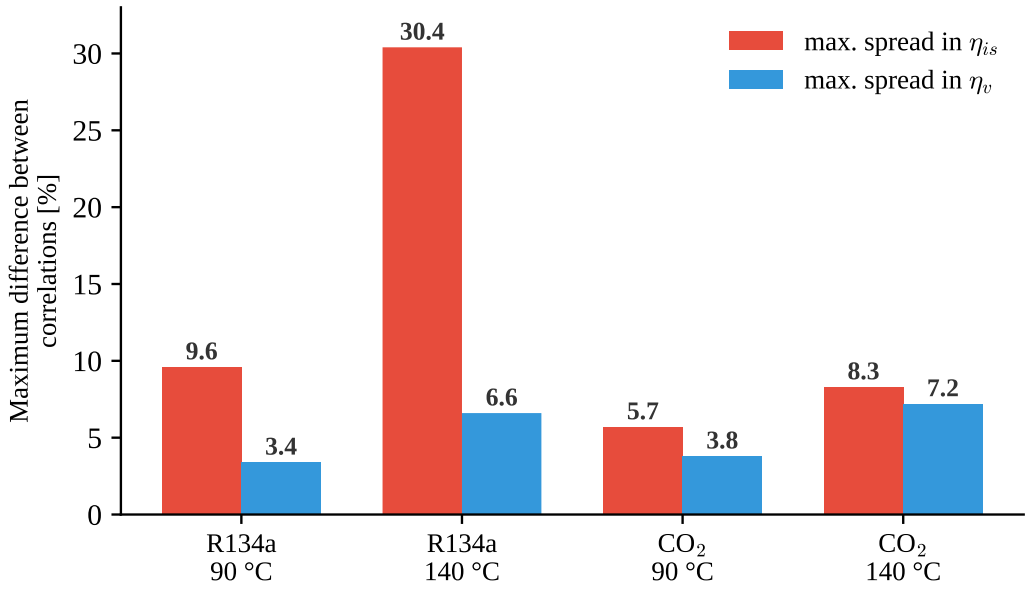

Figure 2.8 Maximum spread in predicted isentropic and volumetric efficiency between five correlations for R134a and CO_2 at wall temperatures of 90 °C and 140 °C. Data from [11]

An earlier conference paper added phase-resolved detail [64]. Net cycle heat transfer ranged by more than a factor of three between models, yet the suction-phase totals were very similar across all five. This apparent paradox arises because the models diverge most in the instantaneous distribution of heat flux within the suction and discharge phases, not in their phase-integrated magnitudes.

A parametric study added the Hohenberg correlation [61] and used CO_2 in a large-bore compressor [56]. Compression and expansion again agreed across all four correlations, with

Woschni and Hohenberg especially close, while Adair differed markedly throughout the cycle because of its crankshaft-angular-speed velocity. Hohenberg, which agrees better with experiment than Woschni, was the primary reference. Mean HTC rose with speed, pressure ratio, and suction pressure, while mean heat flux in each cycle fell with speed as less time is available for exchange. Adair was by far the most sensitive to suction pressure, confirming that its extreme sensitivity is a structural consequence of its velocity definition rather than verified physical behaviour.

The comparison was extended to cryogenic conditions, testing a modification of the Kornhauser framework, on a closed liquid hydrogen pump cylinder [18], [47]. Excluding the piston surface, it gave acceptable heat flux predictions at the liner and head at higher speeds but deviated substantially at the lowest speed and at the piston surface throughout, where the very low thermal diffusivity of liquid hydrogen leaves a persistent cold zone, the formulation cannot represent. The oscillation Péclet number also exceeded the validated range, invalidating the equal-real-and-imaginary-part assumption. Correlations developed for conventional gases therefore cannot be extrapolated to cryogenic fluids without explicit validation.

Table 2.3 Comparative studies of in-cylinder heat transfer correlations

Study	Correlations compared	Reference data	Working fluid	Key finding
Fagotti [46]	Adair, Annand, Liu, Brok, Hamilton, Polman	Measured component temperatures, conductances	R-134a	Annand best overall. Liu and Hamilton physically implausible.
Disconzi [9]	Annand, Woschni, Adair, Liu + own	2D CFD with coupled valve dynamics	R-134a, R-600a	All classical correlations underestimate suction-phase.
Tuhovcak [11]	Annand, Woschni, Adair, Disconzi, Aigner	0D thermodynamic model	Air, CO_2, R134a, R404a	$\Delta\eta_{is}$ up to 30.4 %. Wall temperature more influential than correlation choice.
Liu [56]	Annand, Woschni, Hohenberg, Adair	0D model, large-bore CO_2 compressor	CO_2	Adair most sensitive to p_{suc} Mean $\dot{q}$ decreases with RPM.
Qiu [18]	Lekic (ext. of Kornhauser)	CFD, liquid H_2 pump	Cryogenic H_2	Fails at 30 RPM and at piston surface. Pe_ω exceeds validated range.

A broad survey placed these studies in context, identifying twenty-five correlations published over nearly a century [12]. The small number reflects both the difficulty of the measurements and the commercial incentive to keep calibration data proprietary.

The comparative studies are summarised in Table 2.3. They establish three conclusions relevant to the validation challenge of this dissertation. First, the correlations diverge most sharply dur-

ing the valve-open phases, which are the hardest to instrument and the most sensitive to geometry, valve design, and working fluid. Second, the differences under realistic conditions are large enough to carry engineering significance, with isentropic efficiency differing by up to 30.4% at elevated wall temperatures. Third, none of these studies compares predictions against experimentally measured instantaneous in-cylinder heat flux. All compare against global performance, steady-state temperatures, or other numerical models. The absence of this ground truth is the central limitation of the field.

3 METHODS FOR INSTANTANEOUS HEAT FLUX DETERMINATION

Experimentally verifying the correlations of the preceding chapter requires resolving the instantaneous heat flux at the inner cylinder surface within a single compression cycle. This rules out steady-state techniques. The process is rapid and cyclic, and the heat flux changes direction several times during each cycle. Two approaches exist for measuring heat flux at a reciprocating compressor cylinder surface. Direct measurement using heat flux sensors is simple but subject to practical constraints that preclude its use inside the cylinder. Indirect inference from surface temperature measured by coaxial thermocouples, with semi-infinite solid theory linking the two quantities, is more involved but well-established and suited to in-cylinder conditions. This chapter characterises direct measurement and its limits, then develops the indirect method in the order it is applied, from the underlying theory through the numerical calculation methods to the coaxial thermocouple itself.

3.1 Heat Flux Sensors

Heat flux sensors convert a local temperature difference into a voltage proportional to heat flux, without a separate surface temperature measurement or knowledge of the wall material properties. They form two practical families, the differential-temperature and the calorimetric gauge [65]. Figure 3.1 places these alongside the indirect surface-temperature method developed in the rest of this chapter. The differential temperature class, represented by the Schmidt-Boelter gauge, is the most widely used in industrial and aerodynamic applications. A constantan wire wound around an insulating wafer forms a thermopile by electroplating one half of the coil with copper. The output voltage (3.1)

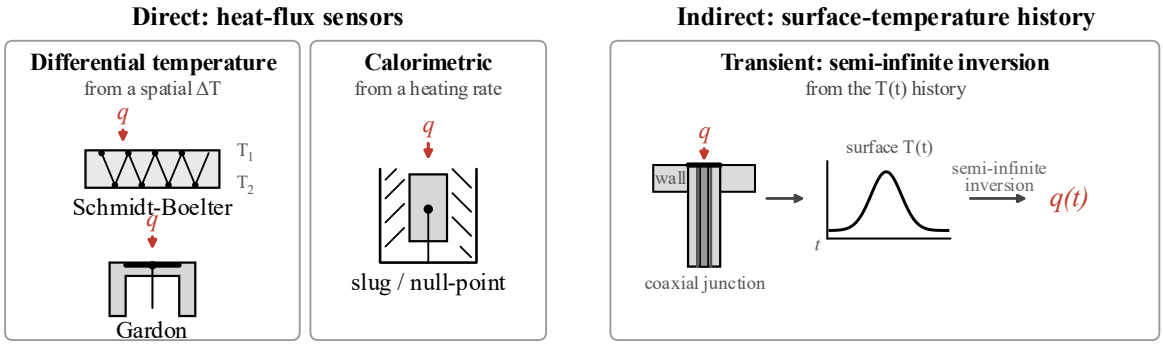

Figure 3.1 Methods for surface heat-flux measurement. Direct heat-flux sensors form two families, the differential-temperature gauge such as the Schmidt-Boelter and Gardon types and the calorimetric gauge such as the slug and null-point types [65]. The indirect method used in this work measures the surface-temperature history with a coaxial surface-junction thermocouple and recovers the flux by semi-infinite inversion (Sections 3.2 and 3.3).

$$E_0 = N \cdot \varepsilon_S \cdot (T_H - T_C) \quad (3.1)$$

where N is the number of turns of constantan wire on the thermopile coil and ε_S the relative Seebeck coefficient, is proportional to the axial temperature difference across the wafer and hence to the heat flux [66]. Calibration against traceable standards establishes the scale factor, with uncertainties below ±4% [66]. Thin-film variants deposit the thermopile onto a polyimide substrate, reducing the sensor profile while keeping the same direct-readout principle [65], [67].

Direct readout is advantageous when two conditions hold together. The heat flux must vary slowly relative to the sensor time constant, and the envelope must accommodate the sensor body. This can be used for example in a measurement of a small hermetic reciprocating compressor. Mounting thin-film thermopile sensors on the inner shell, suction muffler, discharge chamber and on the motor [68]. During several minutes for each steady-state operating point, the calibration-factor uncertainty stayed within ±5%. The cyclic frequency is invisible to the filtered signal, as intended, since only the time-averaged heat flux at each location is needed. This distinction between quasi-steady and instantaneous measurement governs the applicability of heat flux sensors. For crank-angle-resolved heat flux inside the cylinder, which varies by an order of magnitude within a cycle and reverses sign during suction and expansion, the conditions that make these sensors effective no longer hold.

Table 3.1 Capabilities of surface-mounted heat flux sensors compared with in-cylinder requirements

Requirement	**HFS capability**	**In-cylinder need**
Geometric envelope	Sensing element 3–6 mm dia., several mm depth [2]	Cylinder wall thin, valve plate confined; bore 50 mm with limited radial space
Temporal resolution	τ = 10–15 ms for fast Schmidt–Boelter [66]	Valve events span ~1–2 ms; dominant suction HT over 10–20° CA
Thermal disturbance	Cold island effect: sensor body diverts heat laterally if $\beta_{sensor} \neq \beta_{wall}$ [65]	Requires matching β to cast iron (~11 700 W·s½·m^{-2}·K^{-1})
Chemical environment	Adhesive and insulating materials susceptible to degradation	Oil mist, refrigerant atmosphere in hermetic compressors

Four specific constraints prevent their use for in-cylinder instantaneous measurement (Table 3.1). The first is geometric. The restricted internal space of hermetic compressors is the primary

geometric obstacle [2]. The dimensions of commercially available sensors are incompatible with the thin walls and confined bore of the compression cylinder, particularly at the valve plate and cylinder head where the heat flux variation is most pronounced.

The second is temporal. Valve events span one to two milliseconds, an order of magnitude below the response of the fastest gauges, so a sensor resolves only the lowest few harmonics. In a small hermetic compressor, the net transfer to the walls is about 10.2 W during suction, against -4.2 W during discharge and -1.8 W during compression [9]. The dominant suction transfer occurs over 10 to 20 degrees, which a sensor with a 10 to 15 ms response would almost entirely suppress. The finite-response correction (Equation 3.2) gives only partial relief, because it amplifies noise in the signal derivative and is least reliable when the flux changes most rapidly.

$$q_{corr} = q_{meas} + \tau \cdot \frac{dq_{meas}}{dt} \tag{3.2}$$

The third is thermal disruption by the sensor insert. Any flush body with thermal properties differing from the wall modifies the local flux, the cold island effect [65]. A sensor of lower conductivity than the cast iron wall diverts heat laterally and reduces the flux through the sensing surface. Minimising this requires matching the thermal product (Equation 3.3) to the wall, which severely restricts viable materials.

$$\beta = \sqrt{\rho \cdot c \cdot \lambda} \tag{3.3}$$

Furthermore, the chemically aggressive oil and refrigerant atmosphere attacks the adhesives and insulators of commercial sensors and contact resistance at the interface adds a further systematic error.

These constraints jointly preclude heat flux sensors for instantaneous in-cylinder measurement. External and quasi-steady configurations remain appropriate [68]. Crank-angle-resolved flux at the inner wall instead requires measuring the surface temperature history with a flush-mounted sub-millisecond sensor and inferring the flux through the semi-infinite solid relationship between surface temperature and heat flux.

3.2 Semi-Infinite Solid Theory

The indirect approach rests on the one-dimensional semi-infinite solid model of transient conduction. The material is treated as extending to infinity in depth, so a surface disturbance never reaches a far boundary within the time of interest. This section examines the justification for this approximation in a compressor cylinder wall and the relationship it implies between the measured surface temperature and the inferred heat flux. Recovering the surface heat flux from a measured surface temperature is an inverse heat conduction problem, for which the governing theory and solution methods are set out in full [69].

The governing equation for one-dimensional transient conduction in a homogeneous solid with

constant properties is

$$\frac{\partial T}{\partial t} = \alpha \cdot \frac{\partial^2 T}{\partial x^2} \tag{3.4}$$

The surface boundary condition specifies the applied heat flux:

$$-\lambda \cdot \frac{\partial T}{\partial x}|_{x=0} = \dot{q}(t) \tag{3.5}$$

where $\dot{q} > 0$ denotes heat flowing into the solid from the gas. The semi-infinite condition requires $T \to T_0$ as $x \to \infty$. With zero initial temperature perturbation, application of the Laplace transform to this system yields the transformed surface temperature $\tilde{T}_{wall}$ in terms of the transformed heat flux $\tilde{q}$:

$$\tilde{T}_{wall} = \frac{\bar{q}}{\lambda \cdot \sqrt{\frac{p}{\alpha}}} \tag{3.6}$$

where p is the Laplace variable. Inversion gives the fundamental convolution relation between surface temperature and heat flux [67], [70]:

$$T_{wall}(t) - T_\infty = \frac{1}{\beta} \cdot \frac{1}{\sqrt{\pi}} \cdot \int_0^t \frac{\dot{q}(\tau)}{\sqrt{t - \tau}} \, d\tau \tag{3.7}$$

The surface temperature at any instant is a weighted superposition of all past heat flux values, with earlier contributions attenuated as the square root of elapsed time. The thermal product β sets the amplitude of the response. A wall with large β shows smaller surface temperature fluctuations for the same flux.

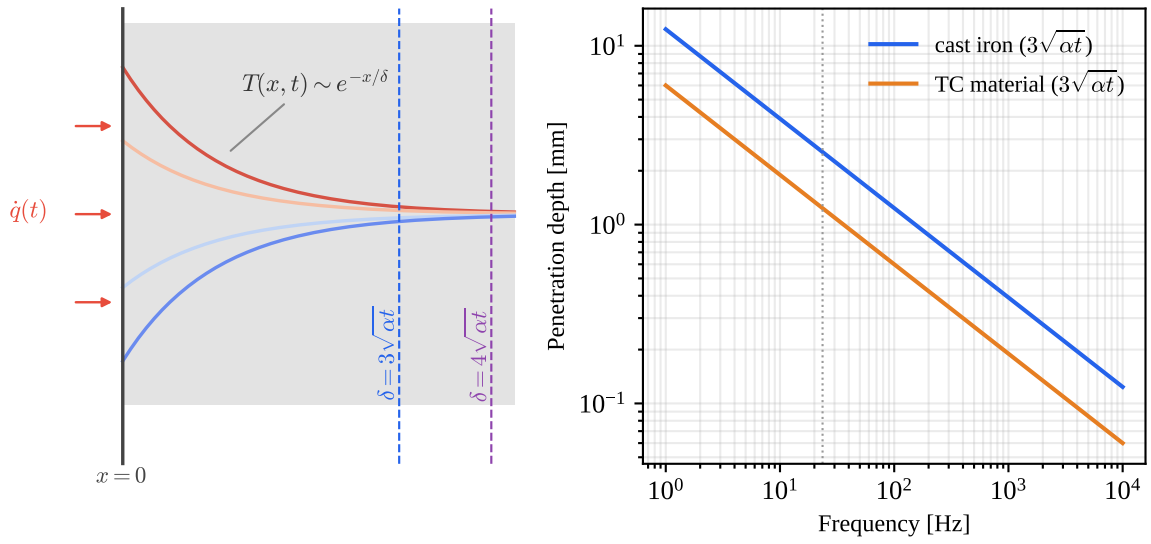

Figure 3.2 Semi-infinite solid model and penetration depth versus frequency for cast iron and the thermocouple material. The validity limits are $3\sqrt{(\alpha t)}$ (Schultz and Jones, 1973) and $4\sqrt{(\alpha t)}$ [65]

In a finite wall the model is valid only while the disturbance penetrating from the surface does not reach the far boundary within the measurement window. Two non-equivalent criteria exist, both shown in Fig. 3.2. The temperature perturbation and the heat flux both fall below one percent at the condition [67]:

$$L_i > 3\sqrt{\alpha t} \implies F_0 = \frac{\alpha t}{L_i^2} < \frac{1}{9} \tag{3.7a}$$

Deriving the condition from the error in the inferred heat flux rather than the temperature attenuation gives the stricter criterion [65]:

$$L > 4\sqrt{\alpha t} \implies F_0 \leq \frac{1}{16} = 0.0625 \tag{3.7b}$$

The two criteria differ by a factor of 1.33 in required wall thickness. Absent a specific error budget, the stricter Childs criterion is the safer requirement. This validity condition recurs below for the thermocouple body and is not restated.

A complementary picture comes from periodic steady-state loading [16]. For purely harmonic loading at a given frequency, the temperature amplitude decays exponentially with depth, so the penetration of unsteady fluctuations is small, and a quasi-steady solution applies to the bulk of the wall. For cast iron at compressor frequencies, both this skin-depth analysis and the step-function analysis yield penetration depths of order one to two millimetres, confirming that the disturbance stays in a thin surface layer throughout the cycle.

Periodic operation adds a separate requirement distinct from the validity condition. The convolution kernel decays slowly, so the memory is not short and the integral formally spans the whole past record. A real record begins at a finite time and carries cycle-to-cycle variability from suction conditions, valve dynamics, and noise. The input must therefore represent the periodic steady-state waveform, not any single noisy cycle. Ensemble averaging over many consecutive cycles, after confirming thermally steady-state operation, meets this requirement (Fig. 3.3). It yields a smooth reproducible periodic surface temperature and suppresses random variability that would otherwise propagate into the heat flux. The practice is well established in engine work. Surface temperature averaged over 198 cycles in a spark-ignition engine showed variability largest at the earliest flame-arrival events [15].

The one-dimensional assumption, that conduction proceeds normal to the surface with no lateral component, needs separate justification in the cylindrical bore. For non-planar boundaries and durations short relative to the solid thermal time scale, the problem is locally one-dimensional to good approximation [71]. Here the active layer is about 1 mm deep against a bore radius of 50 mm, a ratio that makes the curvature correction negligible. The one-dimensional approximation is thus well founded.

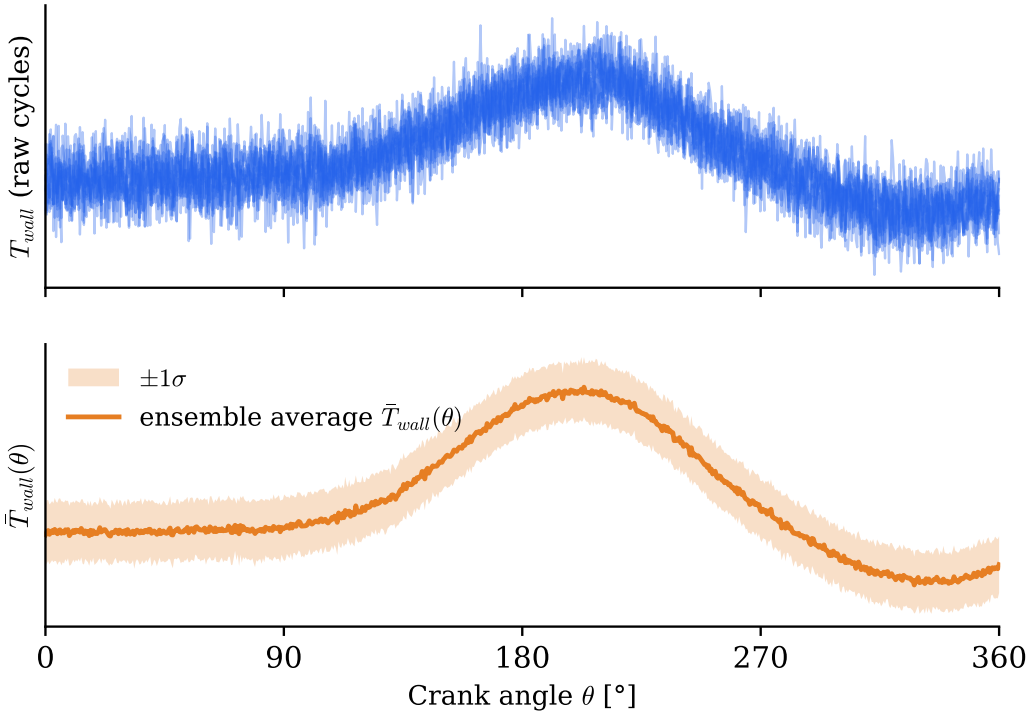

Figure 3.3 Ensemble averaging. Individual noisy cycles and the resulting periodic mean waveform $\pm 1\sigma$.

When the penetration depth approaches the wall thickness, at lower speeds, in thinner sections, or over extended time windows, the semi-infinite model fails and the reflected wave from the rear face must be included. A finite-thickness solution is available for such cases [13], but the penetration depth here stays far below the wall thickness, so the semi-infinite inversion (Section 3.3) is used.

3.3 Heat Flux Calculation Methods

The convolution relation of Section 3.2 defines the forward problem. Given a prescribed heat flux history, the surface temperature follows by integration. Measurement requires the inverse, finding the heat flux consistent with the model from the recorded surface temperature. Direct inversion of the convolution gives [65], [67]:

$$\dot{q}(t) = \frac{\beta}{\sqrt{\pi}} \cdot \left[\frac{T_{wall}(t)}{\sqrt{t}} + \int_0^t \frac{T_{wall}(t) - T_{wall}(\tau)}{(t-\tau)^{3/2}}\, d\tau\right] \tag{3.8}$$

which has a singularity in the integrand at the terminal instant. Continuous evaluation thus needs special treatment of the terminal interval, and several discrete schemes address this.

One approach avoids the singularity by approximating the surface temperature as piecewise linear and integrating each segment analytically [72]. In terms of the values at uniform time steps, the discrete Cook–Felderman (CF) formula is [72]:

$$\dot{q}(t_n) = \frac{\beta}{\sqrt{\pi}} \cdot \sum_{i=1}^{n} \frac{T_{wall}(t_i) - T_{wall}(t_{i-1})}{\sqrt{t_n - t_{i-1}} + \sqrt{t_n - t_i}} \tag{3.9}$$

where the final term includes the current temperature. The continuous singularity is absent because each segment is integrated analytically, and the final denominator is finite and non-zero for any positive step. With 10 intervals the error against the exact solution is about 0.4 % for constant flux, below 0.1 % at 20 intervals, with superior accuracy to earlier methods for non-constant waveforms [72].

The interpretation is simple (Fig. 3.4). Each past temperature increment contributes with a weight, so recent changes count more than remote ones. The formula was derived for a thin-film resistance thermometer, its original context [72]. It applies equally to a coaxial thermocouple, since the semi-infinite model is identical and only the thermal product β differs. Heat flux inferred from a coaxial E-type thermocouple and from a platinum thin-film gauge agreed closely under identical flow [73].

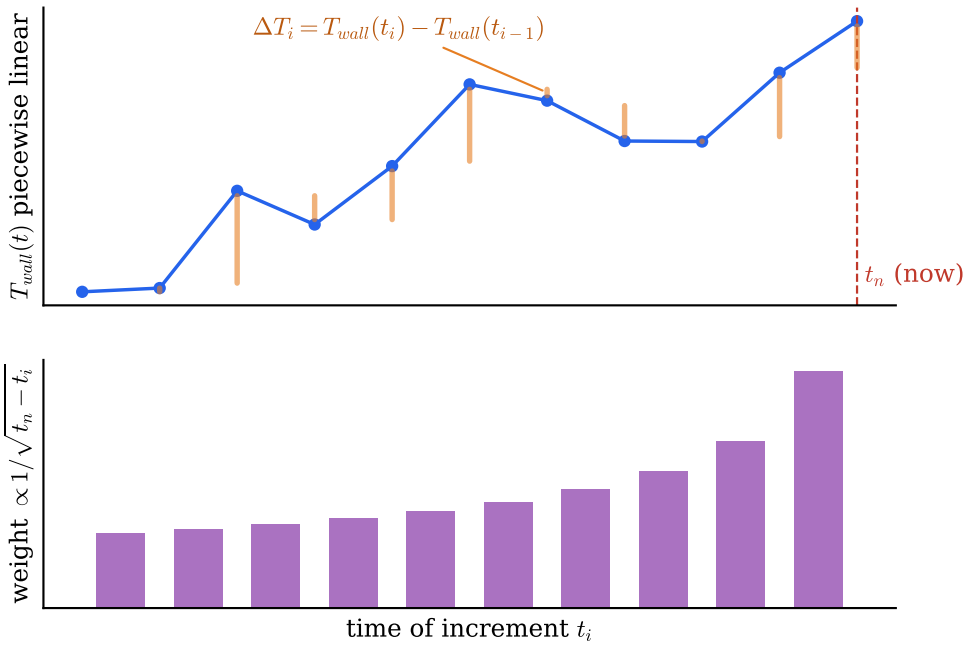

Figure 3.4 Cook–Felderman discretisation. Piecewise linear surface temperature and $1/\sqrt{(t_n - t_i)}$ weighting of past increments.

The main limitation is sensitivity to high-frequency noise. The weight diverges toward the terminal instant, so the most recent increment carries the largest weight and any high-frequency noise in the temperature is amplified by the same factor in the heat flux. This is intrinsic to the inversion. Inverse heat conduction is ill-posed, so noise amplification is unavoidable, not a defect of the approximation, and some form of regularisation is needed [74]. The mitigation is a low-pass filter on the ensemble-averaged temperature before the calculation, removing rather than amplifying components above the physically meaningful range. An alternative with built-in noise suppression is spectral deconvolution [75]. The record is transformed to the frequency domain, inverted spectrally with the known semi-infinite transfer function, multiplied by a

Wiener filter that attenuates frequencies where noise power exceeds signal power, and transformed back. It equals CF in the noise-free limit but degrades more gracefully, since regularisation is applied optimally in frequency rather than at a single cut-off.

CF rests on the semi-infinite assumption. The sum formally spans the whole past surface temperature, and any event so old that its disturbance has reflected from the rear face of the sensing element is treated incorrectly. Two limits apply, the Childs validity criterion [65] and, physically distinct, the arrival of the first reflected wave from the rear face of the thermocouple body, estimated from the finite-slab characteristic time.

A second-order formulation (Equation 3.10) follows from the same governing equation through the Laplace transform, using a piecewise Taylor expansion in time, so the discrete sum extends CF with a quadratic term [13]. The finite-wall reflection series of the full Reichelt solution is negligible here, because the wall diffusion time far exceeds the cycle. Computing both inversions in parallel (Fig. 3.5) cross-validates the discretisation and confirms the recovered flux is free of the first-order CF error. It does not by itself test the semi-infinite assumption, which rests on the penetration-depth criterion above.

$$\dot{q}(\tau_i) = 2\frac{\lambda}{\delta}\sqrt{\frac{\Delta\tau}{\pi}}\sum_{k=0}^{i-1}\left(\left(t'_{S,k} + t''_{S,k}\Delta\tau\left(i - \frac{2k+1}{2}\right)\right) \times R_{i,k} - t''_{S,k}\frac{\Delta\tau}{3}S_{i,k}\right) \tag{3.10}$$

$$R_{i,k} = (i-k)^{\frac{1}{2}} - (i-k-1)^{1/2} \tag{3.10a}$$

$$S_{i,k} = (i-k)^{\frac{3}{2}} - (i-k-1)^{3/2} \tag{3.10b}$$

$$t'_{S,k} = \frac{t_{S,k+1} - t_S}{\Delta\tau} \tag{3.10c}$$

$$t''_{S,k} = \frac{(t_{S,k+2} - t_{S,k+1}) - (t_{S,k} - t_{S,k-1})}{\Delta\tau} \tag{3.10d}$$

For a coaxial thermocouple in diesel spray-wall experiments, the method was validated numerically and applied under conditions comparable to the present work [76].

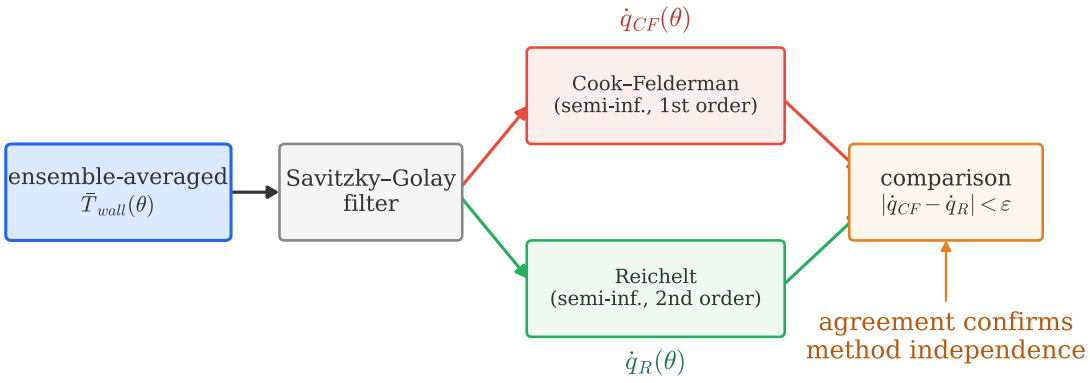

Figure 3.5 Parallel heat flux evaluation by the Cook–Felderman (first order) and Reichelt (second order) methods, both semi-infinite, as a cross-validation of the inversion scheme. The two schemes differ by one sampling interval.

3.4 Coaxial Thermocouples

The calculation methods take the surface temperature history as their sole input. The instrument providing it, and setting the temporal resolution, the validity of the semi-infinite assumption, and the accuracy of the inferred flux, is preferably coaxial surface-junction thermocouple.

The coaxial surface-junction thermocouple is the standard sensor for instantaneous surface temperature in high-frequency transient environments. By the Seebeck effect, two dissimilar conductors joined at one end generate an electromotive force (EMF) proportional to the temperature difference between that junction and the reference end. The junction is the polished flush end face where both materials meet the wall thermal field [77]. Being flush, it doesn't disturb fluid flow and reads the undisturbed boundary-layer condition. The heat flux calculation is valid only if conduction within the body is one-dimensional, with heat flowing axially through both materials and no significant lateral exchange at the junction. This requires closely matched thermal properties of the two electrodes [78], [79]. The body then responds to surface flux like a homogeneous semi-infinite solid, and Sections 3.2 and 3.3 apply unchanged. Neither condition holds perfectly for any pair, but the thermal product dominates the calculation, so matching it between the two electrodes is a sufficient practical approximation.

The construction follows from this requirement (Fig. 3.6). The inner electrode sits concentrically inside the outer, separated by a thin insulating layer that prevents short-circuiting while leaving the junction at the tip. The layer is formed by furnace oxidation of the rod or by a thin epoxy, Teflon coating [77]. For the swaged coaxial design used here it is about 10 µm thick [78]. Grinding and polishing the end face creates the junction, inducing a 20 to 24 µm zone of microplastic deformation where the materials make intimate metallic contact [77]. This gives planarity and forms the junction without welding or soldering. Junction quality is critical [80]. A grind-type junction raised surface roughness that enhanced local convection, so the inferred flux exceeded the true value by about 18 % in hypersonic tunnel tests, whereas an impact-type junction, which displaces material without removing it, stayed within 5 %.

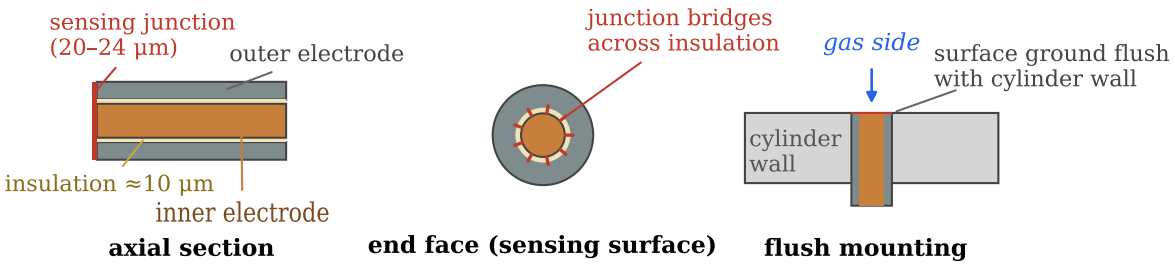

Figure 3.6 Coaxial surface-junction thermocouple. Axial section, end face with junction bridges, and flush mounting in the cylinder wall.

Among the standard thermocouple types that can be implemented in the coaxial geometry, Type E is the preferred choice (Table 3.2).

First, the Seebeck coefficient of the Chromel-Constantan pair is the highest of all standard base-metal types. Fabricated probes calibrate somewhat below the reference tabulation but keep the

relative advantage over Type K [73], [81]. This highest sensitivity directly improves the signal-to-noise ratio at the millivolt signals from the small surface temperature oscillations expected inside the cylinder.

Second, the thermal response time, the lag between a step in applied flux and the output, is shortest for Type E [81].

Third, the thermal products of the two Type E electrodes are closely matched, while the Type K pair is less well matched and the Type J pair the most mismatched (Table 3.2). This near matching minimises lateral exchange across the junction and most closely satisfies the one-dimensional requirement on which the calculation depends.

Table 3.2 Properties of candidate thermocouple types for the coaxial surface junction

Property	Type E	Type K	Type J
Seebeck coefficient (NIST, 20 °C)	63 μV/K	41 μV/K	52 μV/K
Response time τ_r [81]	36 μs	40 μs	46 μs
Thermal product ratio β_+/β_-	1.007	0.75	1.90
1D validity [67]	Best	Intermediate	Poor
Sensitivity advantage vs Type K	×1.32 – ×1.54	Reference	×1.27 (NIST)

The assembled thermal product (Equation 3.1) cannot be assigned from material data alone, because it depends on the electrode alloy composition, junction interdiffusion, and contact-zone geometry. Each sensor needs individual calibration. Three established methods suit different laboratory capabilities (Table 3.3). The water droplet method exposes the heated flush-mounted thermocouple to a characterised impinging drop of known thermal product [77], [82]. The measured contact temperature is compared with the two-body contact formula (Equation 3.11) to yield the thermal product.

$$\frac{T_{surf} - T}{T_{surf} - T_{ref}} = \frac{\beta_{ref}}{\beta_{ref} + \beta} \tag{3.11}$$

The water plunging method applies a temperature step by rapid immersion in hot water and fits the exponential response for the thermal product [77]. The laser pulse method applies a measured step flux from a calibrated laser and computes the thermal product from the surface temperature rise via the semi-infinite formula [78]. Cycle-averaged heat transfer agrees well across methods despite scatter in individual values, so thermal product uncertainty affects the temporal distribution of the flux within the cycle more than its integrated magnitude [77]. The effective value can also depend on the time scale of interest, so a millisecond-scale calibration matches the compressor cycle [82].

The semi-infinite validity condition stated above for the cylinder wall applies equally to the thermocouple body. The body has finite length, and if the surface-driven disturbance reaches its rear face within the measurement window the model is violated, independently of whether the surrounding wall satisfies the condition.

Table 3.3 Calibration methods for the thermal product β

Method	Principle	Note
Water droplet [77], [82]	contact with a characterised water drop, two-body contact formula	direct, sensitive to contact resistance
Water plunging [77]	step immersion in hot water, exponential response fit	simple, slower transient
Laser pulse [81]	calibrated CW-laser step heat flux	within 0.5 % of analytical prediction

The one-dimensional assumption carries two systematic errors tied to the thermocouple geometry (Fig. 3.7). The first is lateral exchange between the electrodes through the thin insulating layer at the junction. Even with matched bulk thermal products, the finite layer thickness creates a small region of lateral rather than axial heat flow. This raises the junction temperature above the one-dimensional prediction, termed junction overheating [83]. Simulation of an E-type thermocouple with a 10 µm layer gives a positive flux error of about 2 to 3 %, proportional to layer thickness. The peak junction temperature shifts laterally toward the Chromel electrode as loading proceeds, and the electrode diameter ratio gives a further degree of freedom, with an optimised ratio cutting the error below 0.5 % [84].

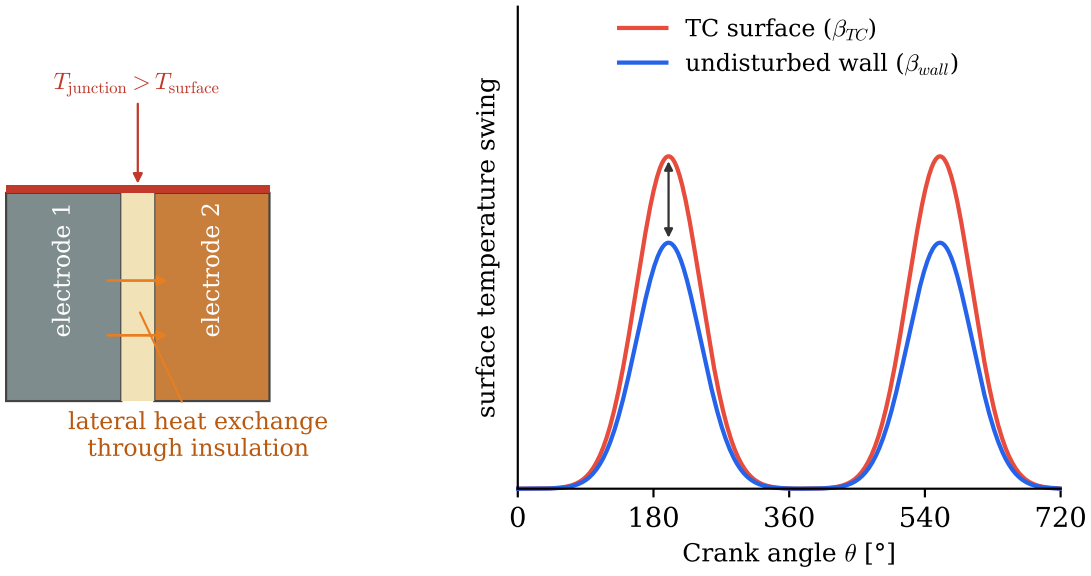

Figure 3.7 Systematic errors of the coaxial thermocouple. Junction overheating gives a positive bias of about 2 to 3 % [83]. The installed error follows from the thermal product mismatch $\beta_{wall}/\beta_{TC} \approx 1.36$ [79].

The second error is more fundamental. Any body in a wall whose thermal product differs from that of the wall modifies the temperature field it measures. This installed error was characterised for Type E, J, and K coaxial thermocouples in a steel piston [79]. For Type E the body overestimates the surface temperature swing by about 57 %, because its lower thermal product stores less energy per unit temperature rise and reaches higher peaks for the same flux. The

overestimation grows with the mismatch ratio, reaching 79 % for an aluminium piston. Small temperature errors amplify in the flux calculation. A peak temperature error of only +1.3 % produced a 23 % peak flux overestimation, because the inversion is sensitive to the temperature rate of change, not the absolute value [85]. Correction algorithms partly mitigate this, but the magnitude depends on the specific thermocouple and wall combination [79].

A practical constraint is electromagnetic interference. The millivolt signal is susceptible to inductive and capacitive coupling from the motor drive and valve actuation nearby. In diesel engine spray experiments, injector-drive artefacts could not be removed without corrupting the thermal signal [76]. Mitigation requires shielded coaxial cables, grounding the sensor body to measurement earth, routing signal leads away from power cables, and where necessary differential acquisition to reject common-mode interference.

4 RESEARCH GAPS AND OBJECTIVES

4.1 Research Gaps

The reviewed work shows a field marked by a fundamental imbalance. A substantial and growing body of numerical and analytical models stands against a scarcity of the experimental ground truth needed to evaluate them. This section identifies the gaps that motivate the experimental programme of this dissertation, separates those it addresses directly from those left open, and explains the connections between them.

The most consequential gap is the absence of direct experimental measurements of the instantaneous HTC inside the cylinder under actual operating conditions. Every comparative study in Section 2.5 evaluates the correlations against each other, against global performance parameters, against steady-state component temperatures, or against other numerical simulations. None compares predictions against measured instantaneous heat flux at the cylinder wall. The demand for such validation was raised by Brok [25], reiterated by Disconzi [9], and restated by Tuhovcak [11]. The consequence is that no consensus exists on which correlation best represents the physical reality of in-cylinder heat transfer.

A prerequisite for determining the HTC is the instantaneous bulk gas temperature, the reference against which the wall temperature is compared (Equation 2.3). This quantity is not directly accessible. Standard thermocouples in the gas stream suffer thermal inertia that prevents them from resolving the rapid variations at valve events and during compression. The uncorrected signal underestimates the true amplitude of the gas temperature variation by roughly a third [17]. The consequence is severe, because the denominator of the coefficient passes periodically through zero during revolution as the gas temperature crosses the wall temperature, and modest errors in the reference produce unrealistic coefficients in these transition regions. The instantaneous gas temperature was identified as a central difficulty in extracting meaningful coefficients from measured data [41], and the field has not satisfactorily resolved it since. A physically appropriate gas temperature reference is therefore a methodological challenge of fundamental importance.

The existing evidence is limited in spatial coverage as well as quantity. The standard compressor-specific correlation was derived from a single fast-response thermocouple in the cylinder head, capturing one location only [6]. Three-dimensional CFD finds that both the magnitude and the direction of the instantaneous heat flux differ between the wall, the piston, and the valve plate at a given crank angle [10]. Each surface's contribution changes through the cycle as valve-induced flow redistributes the convective load [48], and valve port geometry further modifies the distribution in ways single-point measurement cannot capture [57]. Any experimental reference for correlation validation must measure simultaneously at multiple locations on different surfaces.

A further prerequisite is the validity of the semi-infinite approximation under compressor con-

ditions, established for engine work but not yet verified for the lower operating frequency, the oil film, and the wall of a reciprocating compressor.

Beyond the gaps directly addressed by this dissertation, the literature review has identified two physical phenomena whose existence has been established numerically but whose quantitative characteristics under actual compressor operating conditions remain without direct experimental confirmation.

The first is the valve-induced flow enhancement of heat transfer during suction and discharge. CFD shows that the gas jet entering through the suction valve creates convective rates far higher than piston motion alone, which explains why kinematic correlations systematically underestimate suction-phase heat transfer [9]. The fluid-structure interaction between valve dynamics and the internal flow is itself complex [37]. No direct experimental measurement of this enhancement has been reported. The predictions have been validated against each other and against global performance data, but not against local instantaneous heat flux during the valve-open phases.

The second is the phase lag between the gas-wall temperature difference and the resulting heat flux. It was identified in engine measurements [41] and confirmed experimentally in engine cylinders [14], [44]. In high-pressure compressor data it appears as a systematic residual in the correlation fit of Hsieh [8]. A rigorous framework was given through the complex Nusselt number [47], and a practical approximation was incorporated into the first compressor-specific dynamic correlation [58]. Despite this, the lag has not been directly quantified under actual compressor operating conditions, as opposed to the motored engine or gas-spring configurations in which most evidence was gathered.

Evidence on both phenomena would emerge naturally from the crank-angle-resolved heat flux and temperature data of the present work, even if their systematic quantification lies beyond its primary scope. They are the most important directions for subsequent experimental investigation.

The reviewed evidence marks a specific gap distinct from the mere absence of data. Crank-angle-resolved surface heat flux measurements have existed since the work of Overbye [41] and Adair [6] and were extended to compressor conditions by Hsieh [8]. What is missing is the combination of three requirements at once. These are measurement at multiple locations on different surfaces, systematic coverage of a range of operating conditions including varied pressure ratios, and a physically grounded gas temperature reference adequate for computing meaningful coefficients. Each has been addressed individually, but not together. No study has produced a dataset of experimentally determined Nusselt numbers across multiple surfaces and operating conditions for direct comparison against the available correlations. This combination is what this dissertation targets.

4.2 Objectives, Research Questions and Hypotheses

The dissertation pursues three objectives.

- **O1:** Identify the heat fluxes in the cylinder of a reciprocating compressor.
- **O2:** Determine the heat transfer coefficients on selected surfaces of the cylinder.
- **O3:** Verify the dimensionless correlations used for the prediction of the in-cylinder heat transfer coefficient.

Three research questions follow from the objectives and from the gaps identified in Section 4.1.

- **Q1:** How large are the instantaneous heat fluxes on the individual surfaces of the cylinder, and how do they evolve over the cycle and with the pressure ratio?
- **Q2:** Can the heat transfer coefficient be determined reliably from flush-mounted coaxial thermocouples at the speed of a small production compressor?
- **Q3:** Which of the available correlations describes the measured in-cylinder heat transfer best, and in which phases of the cycle do the correlations fail?

Three hypotheses are formulated.

- **H1:** The instantaneous heat flux changes direction at least twice in each revolution. Its cycle average on the cylinder wall and on the valve plate is directed from the wall into the gas, so it feeds the suction gas superheating directly.
- **H2:** Quasi-static kinematic correlations underestimate the heat transfer during the valve-open phases, most severely at the valve plate, because they do not represent the flow induced by the valves.
- **H3:** The disagreement between the correlations and the measurement is structural. It depends on the phase of the cycle and on the surface. It cannot be removed by adjusting the leading constant alone.

5 EXPERIMENTAL SETUP

The experimental programme described in this dissertation was carried out on a purpose-built test rig centred on the Orlík EK 4-2 reciprocating compressor. The objective of the experiment is the determination of the instantaneous wall heat flux at the cylinder wall and valve plate over the operating range, and the comparison of the experimental results with the predictions of the five correlations reviewed in Chapter 2. The experimental heat flux is inferred directly from the surface temperature measured by flush-mounted coaxial thermocouples, using the semi-infinite solid inversion described in Chapter 3. This step does not require knowledge of the gas temperature. The evaluation of the correlation predictions, however, requires the instantaneous bulk gas temperature, which enters through the thermophysical gas properties needed to compute the Reynolds and Prandtl numbers and through the temperature difference that relates the Nusselt number to heat flux. Since the bulk gas temperature cannot be measured directly in the present configuration, it is reconstructed from the measured instantaneous cylinder pressure and the known cylinder geometry through a zero-dimensional thermodynamic model.

This chapter describes the complete experimental methodology in the order of the measurement and processing chain. It covers the test rig and its instrumentation, the signal processing steps that convert the raw thermocouple signal to surface temperature, and the thermodynamic model that reconstructs the gas temperature and identifies the phase boundaries of the cycle. It then describes the evaluation of the heat flux, the HTC, and the Nusselt number, including the comparison with the correlation predictions. The chapter closes with the uncertainty analysis that establishes the confidence limits on the experimental results.

5.1 Test Rig and Instrumentation

Test Rig Description

The compressor at the centre of the test rig is the Orlík EK 4-2 (Orlík, Czech Republic), a single-cylinder, single-stage, air-cooled reciprocating compressor operating with air as the working fluid. The principal geometric parameters of the compressor are summarised in Table 5.1, taken from the manufacturer's catalogue (DNKP01800002) and consistent with those reported by Tuhovčák [24] for the same compressor unit, which was used in the comparative correlation studies of Tuhovčák [11], [64] that provide the methodological foundation for this work. The assembled test rig is shown in Figure 5.1.

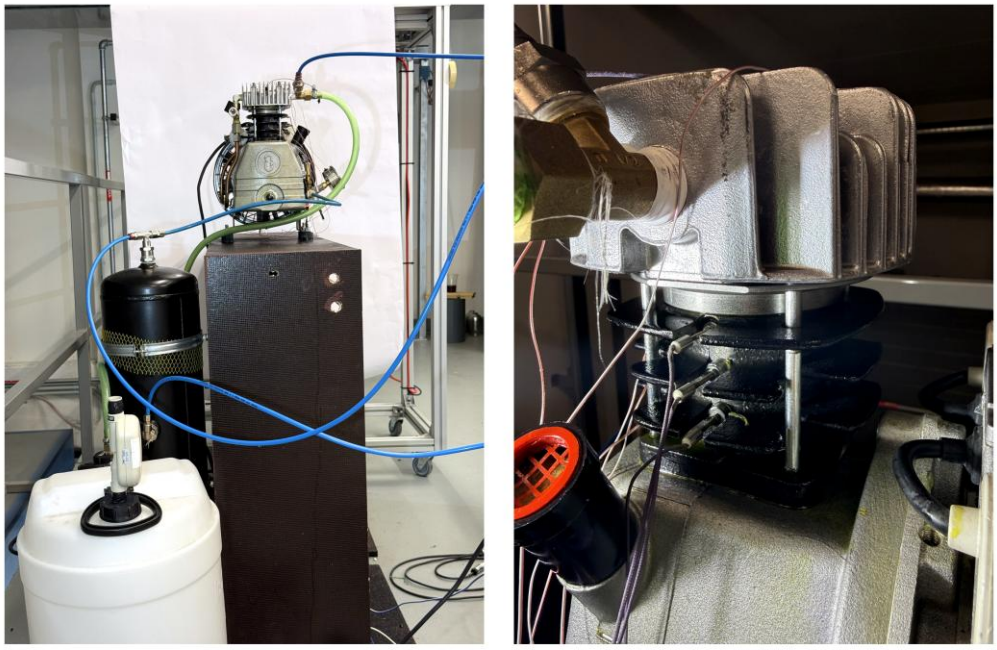

(a) (b)

Figure 5.1 The test rig. (a) Overview of the Orlík EK 4-2 compressor with the discharge vessel and the connecting lines. (b) The instrumented cylinder head with the coaxial surface-junction thermocouples.

Table 5.1 Main parameters of the Orlík EK 4-2 compressor

Parameter	Value	Unit
Cylinder bore	50	mm
Piston stroke	45	mm
Swept volume	88.4	cm^3
Crank radius	22.5	mm
Connecting rod length	86.1	mm
Clearance ratio	3.9	%
Nominal speed	1415	min^{-1}
Max. discharge gauge pressure	10	bar
Shaft power	0.68	kW

The test rig connects the compressor discharge to a regulated pressure vessel, with a manually adjustable throttle valve used to set the discharge pressure and so the operating pressure ratio. The suction side draws air from the laboratory environment through an inlet filter and flow measurement section. Measurement points for absolute pressure and temperature are located on both the suction and discharge sides of the compressor, enabling determination of the thermodynamic operating point independently of the in-cylinder instrumentation. The same experimental platform has been used in the preceding studies [11], [64], [86], which established the

basic measurement methodology and validated the synchronisation and processing chain adopted in the present work. A schematic diagram of the test rig is shown in Figure 5.2, with both the temperature head configuration and the pressure head configuration.

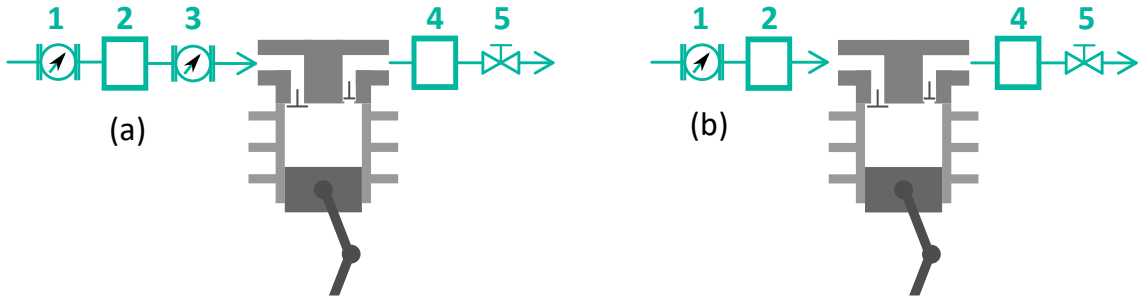

Figure 5.2 Flow circuit of the test rig, drawn for (a) the temperature head and (b) the pressure head. Air is drawn from the laboratory through the suction line and its flow instrumentation, compressed in the cylinder, and delivered to a regulated pressure vessel through a throttle valve that sets the discharge pressure. 1 – TSI flow meter; 2 – flow dampening vessel; 3 – Sensirion flow meter; 4 – pressure vessel; 5 – manual throttle valve

Instrumentation

The instrumentation of the test rig serves two distinct measurement objectives that cannot be satisfied at once with a single cylinder head configuration. The first objective is the determination of instantaneous surface temperature and heat flux at the cylinder wall and valve plate. The second is the measurement of instantaneous cylinder pressure together with discharge chamber pressure. These two objectives require different sensors to be installed at the same locations in the cylinder head. The valve plate does not offer sufficient space to accommodate both a coaxial thermocouple and a pressure transducer simultaneously, and while combined sensors capable of measuring both surface temperature and pressure at a single point exist, their reliability and measurement accuracy are considered insufficient for the purposes of the present work. The two objectives were therefore pursued in two separate measurement configurations using interchangeable cylinder heads. Both heads are original manufacturer-supplied components with identical external geometry and mounting interface, ensuring that the thermodynamic operating conditions are reproducible between configurations. The sensor layout of the two heads is shown in Figure 5.3.

In the first configuration, hereafter the temperature head, the cylinder head is equipped with three coaxial type-E thermocouples for instantaneous surface temperature measurement. Two Dr. Müller Instruments MT19 sensors are mounted flush in the cylinder wall at axial distances of 9.04 mm and 24.65 mm from top dead centre, measuring the inner wall temperatures $T_{wall,C1}$ and $T_{wall,C2}$ respectively. A Dr. Müller Instruments MCT19 sensor is mounted flush in the valve plate at the centre of the compression space, measuring $T_{wall,VP}$. The individually calibrated thermal products and sensitivities are listed in Table 5.2. The temperature head also carries type-T thermocouples for measurement of the surface temperature of the compressor head at the suction and discharge chamber positions ($T_{surf,suc}$, $T_{surf,dis}$), and a type-T probe inserted directly into the discharge chamber gas (T_{dis}).

In the second configuration (pressure head) the cylinder head is equipped with three Kulite piezoresistive pressure transducers for crank-angle-resolved measurement of instantaneous cylinder (p_{cyl}), discharge chamber (p_{dis}), and suction chamber ($p_{suc,hs}$) pressures. The specifications of all three transducers are listed in Table 5.2. All three use a fully active four-arm Wheatstone bridge on a dielectrically isolated silicon-on-silicon sensing element, and their bridge output is conditioned by a dedicated signal amplifier that simultaneously provides the 10 VDC bridge excitation and delivers a 0–10 V voltage output to the data acquisition system. The pressure head also carries a type-T thermocouple inserted directly into the suction chamber gas (T_{suc}).

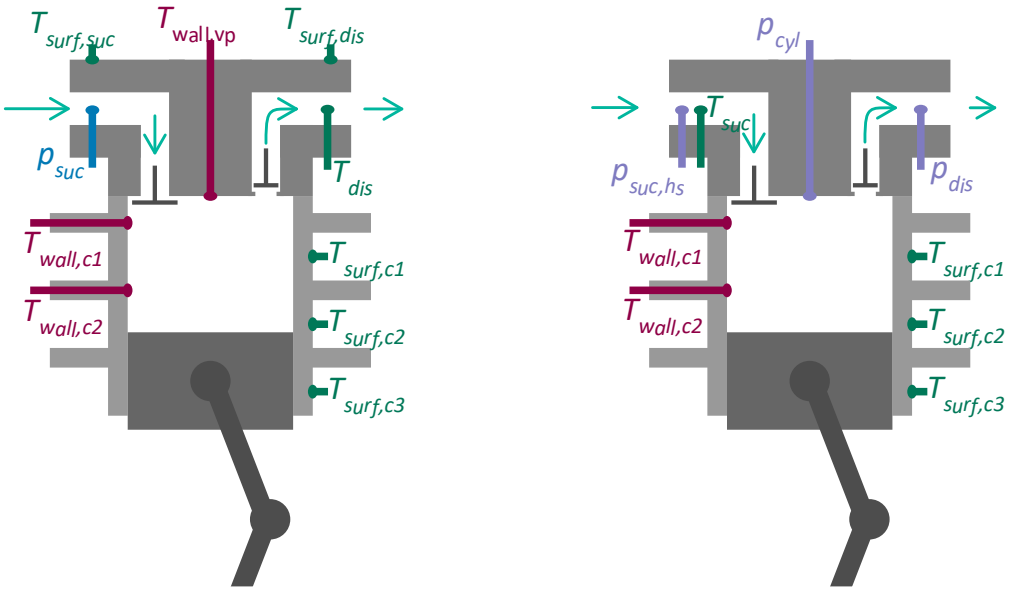

Figure 5.3 Cylinder-head instrumentation. (a) The temperature head carries the three coaxial thermocouples, two in the cylinder wall and one at the valve plate, with the surface and gas thermocouples. (b) The pressure head carries the three Kulite transducers for the cylinder, suction, and discharge pressures.

Instrumentation common to both configurations is listed in Table 5.2. The three coaxial type-E thermocouples have certified thermal products of 8573, 8611, and 8614 $W \cdot s^{0.5} \cdot m^{-2} \cdot K^{-1}$ for $T_{wall,C1}$, $T_{wall,C2}$ and $T_{wall,VP}$ respectively, together with the class-1 tolerance of the type-E pair. A Wachendorff WDGI 58B incremental shaft encoder mounted on the compressor crankshaft extension provides the crank-angle reference for all measurements. Only the index channel N is used, producing a single voltage pulse in each revolution aligned with top dead centre. On the suction side, a Sensirion SFM3000 bidirectional digital flow meter captures the pulsating instantaneous flow and is synchronised with the compressor cycle in post-processing through the pressure pulsations recorded on the suction line. Type-T thermocouples are distributed at three axial positions on the outer surface of the cylinder wall ($T_{surf,C1}$–$T_{surf,C3}$), in the immediate vicinity of the cylinder, and at the cold-junction reference location of the coaxial thermocouples.

Table 5.2 Test-rig instrumentation, with the model, measured value, range and accuracy of each instrument and the configuration in which it is used.

Instrument	Model	Measured Value	Range	Accuracy	Configuration
Coaxial type E $T_{wall,C1}$	Dr. Müller MT19	Surface temperature cylinder wall	900 °C		Temperatures
Coaxial type E $T_{wall,C2}$	Dr. Müller MT19	Surface temperature cylinder wall	900 °C		Temperatures
Coaxial type E $T_{wall,VP}$	Dr. Müller MCT19	Surface temperature valve plate	900 °C		Temperatures
Pressure transducer	Kulite HKS-11HP-375	Cylinder pressure	35 barG	±0.1 % FSO	Pressures
Pressure transducer	Kulite HKL-375M-250D	Discharge chamber pressure	17barD	±0.1 % FSO	Pressures
Pressure transducer	Kulite HKL-375M-50D	Suction chamber pressure	3.5 barD	±0.1 % FSO	Pressures
Encoder	Wachendorff WDGI 58B	TDC position	720 PPR		Both
Flow meter	TSI 4040	Suction flow	300 SLPM	±2 % R	Both
Flow meter	Sensirion SFM3000	Suction flow	200 SLPM	±1.5 % R	Pressures
Pressure transmitter	Airflow PTLA K120	Suction pressure	120 kPa		Temperatures
Pressure transmitter	BD Sensors DMP331	Vessel (reference) pressure	20 barG	±0.35 % FSO	Both

Thermocouple installation

The validity of the heat flux calculation rests on the assumption that the sensing surface of each coaxial thermocouple is flush with the inner surface of the cylinder wall, so that no cavity or

protrusion disturbs the local flow and the thermoelectric signal represents the true wall surface temperature. Achieving this condition requires that the thermocouple tip is ground to the precise radius of curvature of the bore after installation, and that no adhesive layer or filler material is interposed between the sensor body and the gas. The installation procedure adopted in the present work mounts each thermocouple body into an SLA-printed plastic screw, which is in turn threaded into the cylinder wall or valve plate. The plastic screw electrically insulates the thermocouple body from the cast iron cylinder wall, providing shielding against the electromagnetic interference generated by the electric motor in the immediate vicinity of the sensors. At the same time, the low thermal conductivity of the plastic material reduces the thermal coupling between the thermocouple body and the surrounding wall, which may affect the local temperature field at the sensing surface.

The thermal product β of each thermocouple, the parameter that enters directly into the heat flux calculation, cannot be assigned reliably from tabulated material data because it depends on the specific alloy composition, the geometry of the sensing junction, and any interdiffusion at the contact zone. The values used in the present work are those provided by the manufacturer (Dr. Müller Instruments) as part of the individual sensor certificate for each probe. The recovered flux is sensitive to the wall thermal product and to the exact placement of the junction [87]. The close agreement between the three values (spanning only 41 $W \cdot s^{\wedge}½ \cdot m^{-2} \cdot K^{-1}$, or 0.5% of the mean) confirms the consistency of the manufacturing and certification process and provides confidence that sensor-to-sensor variability in β is negligible relative to other sources of uncertainty in the heat flux determination.

Data Acquisition System

All measurement channels are acquired through two parallel but synchronised data acquisition systems, summarised in Table 5.3. The primary system uses a 24-bit NI 9238 module on a ±500 mV range. The Graphtec modules are 16-bit, with a voltage accuracy of ±0.25 % of full scale on the high-speed and voltage modules and a thermocouple accuracy of ±(0.05 % of reading + 1 °C) with internal cold-junction compensation on the voltage/temperature module. The encoder N signal is routed simultaneously to both systems, providing a common TDC reference that allows the two data streams to be aligned in post-processing.

The encoder HTL output voltage (5 V) exceeds the input range of the NI 9238 and is therefore passed through a resistive voltage divider before connection to the module input. The resulting scaled voltage signal is recorded continuously, and the TDC instants are identified in post-processing by peak detection. Signal acquisition and data logging on the NI system are implemented in LabVIEW, which saves the data as an LVM file. The Graphtec system records and saves its data independently as a binary GBD file, without passing through LabVIEW. The higher sampling rate of 100 kHz on the Graphtec system is chosen to ensure that no encoder N pulse is missed. The Sensirion SFM3000 acquires data independently through its own I²C interface and dedicated sensor bridge. It is synchronised with the compressor cycle in post-processing through the pressure pulsations recorded on the suction line.

Table 5.3 Data acquisition systems and recorded signals

System	Hardware	Sampling Rate	Acquired Sensor Signal
Primary	NI 9238 in cDAQ-9171	50 kHz	$T_{wall,C1}$; $T_{wall,C2}$; $T_{wall,VP}$; Encoder N
Secondary	GraphtecGL7000 (HSV + M + V)	100 kHz	Kulite transducers, BD Sensors DMP331, TSI 4040, encoder N, type-T TCs, PTLA K120
Flow Sensor	Sensirion SensorBridge	2 kHz	Sensirion SFM3000

Operating conditions and Measurement Procedure

Measurements were performed over several discharge pressure ratios at nominally fixed compressor speed. The asynchronous motor maintains a speed close to 1415 min^{-1}, though a small degree of slip is natural to the motor type and the actual speed varies slightly with the operating load. The encoder-derived instantaneous speed is therefore recorded at each operating point rather than assumed constant. The pressure ratio was set by adjusting a needle valve located on the outlet of the discharge pressure vessel, which provides fine control of the backpressure against which the compressor operates. Prior to each measurement, the compressor was allowed to run at the target operating condition until the discharge temperature, and the p-V diagram showed no visible trend, typically requiring at least 30 minutes of warm-up.

5.2 Signal Processing and Surface Temperature

The raw thermocouple signals acquired by the NI 9238 module require a sequence of processing steps before they can serve as input to the heat flux calculation. These steps are applied in the fixed order described below, preserving the physical meaning of each transformation.

The first step is reference subtraction. Before each measurement at a given operating condition, a reference record is acquired with the compressor at rest and the thermocouple signals at thermal equilibrium with the laboratory environment. This idle record establishes the zero-flow EMF baseline for each channel, which encodes the thermoelectric contribution of the signal cables, connections, and any residual electrical offsets in the acquisition hardware. Subtracting this reference from the measurement record removes these static contributions and ensures that the subsequent EMF-to-temperature conversion reflects only the thermal variation induced by the compression cycle.

The second step is conversion of the EMF signal to surface temperature. The total thermoelec-

tric EMF at the instrument terminals is the sum of the junction EMF and the cold-junction contribution from the reference temperature at the terminals of the NI 9238 module. The cold-junction temperature is measured continuously by a dedicated type-T thermocouple at the module terminals. The conversion follows the NIST ITS-90 polynomial for type-E thermocouples in both directions. The cold-junction temperature is converted to an equivalent EMF, which is added to the measured differential EMF to recover the absolute junction EMF, and the resulting value is converted to temperature using the inverse NIST polynomial. This procedure is fully consistent with the IEC 60584 standard for thermocouple calibration and avoids any linearisation error that would result from applying a fixed sensitivity coefficient.

The third step is ensemble averaging. The semi-infinite solid theory on which the heat flux calculation rests requires the input surface temperature to represent the periodic steady-state waveform of the thermal cycle, rather than any individual noisy revolution. Cycle-to-cycle variability, arising from fluctuations in suction conditions, valve dynamics, and signal noise, must be suppressed before the convolution is evaluated. Individual compression cycles are identified from the encoder N signal by peak detection, which marks the passage through top dead centre and defines the start of each revolution. The signal is resampled to a uniform crank-angle grid of 1440 points in each revolution (0.25° resolution) by linear interpolation between the TDC-defined cycle boundaries, and the ensemble average is computed over all complete revolutions in the record. The standard deviation across cycles is computed simultaneously at each crank-angle position as a diagnostic of cycle-to-cycle variability. The measurement duration was approximately 10 seconds for each operating point. At the nominal speed of 1415 min^{-1}, a 10-second record contains approximately 235 complete revolutions, which is sufficient for the ensemble average to converge to a stable periodic waveform.

The fourth step is Savitzky-Golay filtering of the ensemble-averaged temperature signal prior to the heat flux calculation. The inversion of the convolution integral that relates surface temperature to heat flux is an ill-posed operation that amplifies high-frequency noise. The weight applied to the most recent temperature increment in the CF formula is proportional to $1/\sqrt{\Delta t}$ and diverges as the time step decreases. Any high-frequency noise carried over from the 50 kHz acquisition into the resampled ensemble average, on which the inversion operates, is therefore strongly amplified relative to the contribution from one full cycle earlier. Smoothing the temperature signal before inversion is not optional but a methodological necessity. A Savitzky-Golay filter of polynomial order 3 with a window of 11 samples is applied to the ensemble-averaged temperature signal. This filter fits a cubic polynomial to each window of 11 consecutive points and replaces the central point with the polynomial value, which preserves the shape of smooth features, including the physically meaningful temperature extrema near valve events, while attenuating high-frequency noise. The same filter type is used by Dr. Müller Instruments in their Heat Flux Calculator (HFC) software supplied with the MT and MCT sensor series, providing an independent validation of this choice for the present class of measurement.

5.3 Thermodynamic Model and Gas State Reconstruction

The instantaneous bulk gas temperature $T_{gas}(\theta)$ is required as the reference temperature for evaluation of the HTC (Equation 2.3). This quantity is not directly measurable by any sensor in the present experimental configuration. Fine-wire thermocouples placed in the gas stream are subject to thermal inertia that prevents resolution of the rapid temperature variations associated with valve events [17], and the gas temperature is instead reconstructed from the measured instantaneous cylinder pressure $p(\theta)$ and the known cylinder geometry $V(\theta)$ through a zero-dimensional thermodynamic model.

Before the reconstruction, the absolute level of the cylinder pressure is corrected for the zero drift of the piezoresistive transducer, which varies between runs by −0.4 to +0.3 bar because the cold-measured reference is subtracted from a sensor operating warm. The correction is applied in two stages. Stage one anchors the pressure at inlet valve closing to the suction pressure minus a small throttling depression, $p_{cyl}(\mathrm{IVC}) = p_{suc} - \Delta p_{dep}$ with $\Delta p_{dep} = 0.08$ bar. Stage two refines the additive offset from the condition that the reconstructed mass difference $m_{comp} - m_{exp}$ equals the mass delivered in each cycle according to the TSI 4040 reference flow meter. The Sensirion flow signal itself serves only diagnostically, because its absolute reading saturates under the pulsating conditions. Its waveform is scaled to the TSI reference.

The model treats air as an ideal gas with specific gas constant $R = 287$ J/(kg·K) and exploits the distinct character of each phase of the compression cycle. During the compression phase - inlet valve closing (IVC) to discharge valve opening (EVO) - and the expansion phase - discharge valve closing (EVC) to inlet valve opening (IVO) - the cylinder is a closed system with constant gas mass. The ideal gas law then yields the instantaneous temperature directly (Equation 1.4).

For compression, the trapped mass m_{comp} is evaluated from the reference state at inlet valve closing (Equation 1.4) and refined by the cycle-closure iteration described below. For expansion, m_{exp} follows from the measured p_{EVC} and V_{EVC} together with the temperature T_{EVC} delivered by the discharge-phase energy balance. This approach requires no assumption about the polytropic exponent n, which varies continuously as the balance between compression work and heat transfer shifts, and relies only on the directly measured pressure trace and the well-defined compressor geometry.

During the discharge phase (EVO to EVC) and the suction phase (IVO to IVC) the gas mass changes, and $T_{gas}(\theta)$ is obtained from an open-system energy balance integrated step by step across the phase. The balance uses the measured heat flux (Section 5.4) as the heat input, temperature-dependent specific heats, and the instantaneous mass change computed from the pressure trace. During discharge the balance accounts for outflow and for backflow through the closing valve. Backflow is detected as $\mathrm{d}m/\mathrm{d}\theta > 0$ within a window before EVC and is assigned the enthalpy of the gas in the valve pocket. The returning gas is the gas discharged a moment earlier, which sits in the valve pocket, so its temperature is close to the gas temperature of the discharge phase. The slow thermocouple in the discharge line reads a mixed temperature and

is therefore not used for this purpose. During suction the incoming gas enters with the enthalpy of the suction state. The cycle is closed by a bisection on the temperature at inlet valve closing, which sets the trapped compression mass m_{comp}. The mass at IVC delivered by the suction-phase balance must equal the trapped mass of the following compression. All four phase boundaries are continuous by construction, and the closed-phase energy balance, no longer used as an estimator, serves as an independent consistency check.

Because the model applies a different formulation to the closed and open phases of the cycle, the crank angles at which the valves open and close must be determined from the measurement data. The four phase boundaries are identified from the pressure head measurements and subsequently applied to the temperature head data. This approach is possible because the two configurations are operated at identical thermodynamic conditions, and it avoids the need to infer phase boundaries from the thermocouple signals alone. The boundaries are detected by different methods, each exploiting the physical character of the corresponding valve event, with fallback methods applied when the primary signal is unavailable.

IVC is identified from the instantaneous flow signal of the Sensirion SFM3000. After bottom dead centre the suction valve remains open briefly, and IVC is assigned to the final peak of the valve flow before its decline to zero. The estimate is refined by the onset of the sustained rise of the fast suction pressure $p_{suc,hs}$ as the valve closes.

EVO is detected from the instantaneous discharge chamber pressure $p_{dis}(\theta)$. The onset of valve opening is identified as the crank angle at which the gradient $\mathrm{d}p_{dis}/\mathrm{d}\theta$ first rises significantly above the baseline, confirmed by the corresponding local maximum in the cylinder pressure as gas begins to escape through the opening valve.

IVO is identified from the fast suction pressure signal $p_{suc,hs}$. At valve opening, a pressure wave propagates into the suction chamber, causing a sustained drop in $p_{suc,hs}$. IVO is assigned to the onset of this drop.

EVC is identified from the cylinder pressure alone. During the discharge phase, p_{cyl} oscillates due to valve dynamics. After valve closure the cylinder becomes an isolated system and p_{cyl} transitions to a smooth monotonic decrease. EVC is assigned to the last pressure reversal before this transition.

5.4 Heat Flux, Heat Transfer Coefficient, and Nusselt Number

The instantaneous heat flux at each thermocouple position is computed from the ensemble-averaged, filtered surface temperature $T_{wall}(\theta)$ using the CF discrete approximation to the semi-infinite solid inversion formula (Equation 3.9) [72]. The Reichelt [13] inversion is computed in parallel as a cross-validation using the same temperature input. It is a second-order accurate form of the same semi-infinite solution, evaluated with a piecewise Taylor expansion in time rather than the first-order CF kernel. The finite-wall series in the full Reichelt solution is negligible here, because the wall diffusion time far exceeds the cycle, so both inversions describe

the same semi-infinite solid and differ only in their order of accuracy. Their close agreement thus confirms that the recovered flux is independent of the inversion scheme and free of the first-order discretisation error of the CF formula. It does not test the semi-infinite assumption itself, which rests separately on the thermal penetration depth remaining far below the wall thickness.

The CF inversion is non-local in time. The heat flux at a given instant depends on the entire preceding history of the surface temperature, weighted by a kernel that decays only as the inverse square root of the elapsed time. Truncating this history to a short window loses the cycle-averaged flux, which is carried by the slowly decaying tail of the kernel (Table 5.4). The error decays only as the inverse square root of the window length, so even a five-revolution window leaves the estimate essentially zero-mean. Only the peak amplitude converges quickly. The cycle-averaged flux is recovered only with the full periodic history, beyond the wall diffusion time of about 1.35 s, roughly 33 revolutions at the present speed. Both the CF and the Reichelt formulations are therefore evaluated with a periodic extension of 500 preceding cycles, equivalent to the exact steady-periodic solution.

Table 5.4 Error of the Cook–Felderman heat flux caused by truncating the surface temperature history to a window of L_w crank angle degrees. Measured valve plate data. The reference is the steady-periodic solution

History window L_w [°CA]	**RMS error [% of $\sigma(q)$]**	**Peak flux error [%]**	**Cycle-mean flux**
5	77	−60	lost
30	54	−10	lost
360 (1 revolution)	21	−12	lost
1800 (5 revolutions)	10	−5	lost
full periodic (steady state)	0.6	< 1	recovered

The instantaneous HTC is then expressed from equation 2.3. The denominator passes through zero several times each revolution, at the crank angles where the gas temperature crosses the wall temperature in each direction. HTC values near these crossings are excluded from the analysis, because the signal-to-noise ratio in the denominator becomes insufficient for physically meaningful interpretation.

Five correlations are carried into the quantitative evaluation. They were selected on three grounds. They span the structural criteria identified in Chapter 2, namely the characteristic velocity, the valve-open treatment, and the phase lag. They require only the measured pressure trace, the rig geometry, and quantities derived from these, namely the gas temperature and the valve mass flow. And they include the correlations of greatest historical and practical weight.

Annand [4] and Woschni [5] are the canonical engine in-cylinder forms, and Adair [6] is the first compressor-specific correlation. All three recur as benchmarks throughout the comparative literature reviewed in Chapter 2 [11], [46], [56]. Disconzi [9] and Aigner [10] are added as the only reviewed forms that resolve the valve-open flow. The remaining correlations reviewed in Chapter 2 are not included. The early dimensional and engine-swirl forms [42], [43] predate the Nusselt-Reynolds framework used here, and the compressor-era forms excluded in Chapter 2 would not add independent information.

The Nusselt number predictions of the five correlations reviewed in Chapter 2 are computed under identical conditions. All five use the same measured pressure trace, the same geometric parameters, and the same air property correlations. The characteristic velocities and length scales are defined for each correlation exactly as specified in Chapter 2, without adjustment. The Annand correlation is evaluated in its Peclet-number form (Equation 2.4b), which appends a Prandtl-number factor to the original mean-piston-speed expression, as is standard in compressor studies [11]. The Adair correlation uses the reduced swirl constant of Brok [25], appropriate to the open-type compressor tested here. The gas temperature is treated in two complementary modes. In the first, each correlation drives its own open-system energy balance, so that its HTC and gas temperature are mutually consistent, exactly as the correlation would behave inside a predictive compressor model. In the second, all correlations are evaluated with the common experimental gas temperature of Section 5.3, which isolates the comparison of the HTCs themselves. The mode used for each presented result is stated in Chapter 6. This ensures that differences between the experimental Nusselt number and the correlation predictions reflect genuine physical discrepancies rather than implementation choices.

The instantaneous mass flow rate through the valves is a derived output of the thermodynamic model that is required for the evaluation of the Disconzi et al. (2012) correlation, in which the characteristic velocity during the suction and discharge phases is defined by Equation (5.1). u_{char} enters only in the suction and discharge branches of the correlation. During compression and expansion, the Reynolds number is based solely on the piston mean velocity. During discharge, $\dot{m}(\theta)$ is estimated from the rate of change of the reconstructed cylinder gas mass, consistent with the determination of T_{gas} described above. The accuracy of this estimate is limited by determination of T_{gas} during discharge and by the assumption of uniform instantaneous gas properties within the cylinder. Since $\dot{m}(\theta)$ enters the Disconzi et al. (2012) correlation through the characteristic velocity, uncertainties in the mass flow rate propagate directly into the Reynolds number and hence into the predicted Nusselt number for the valve-open phases.

$$u_{char}(\theta) = \frac{\dot{m}(\theta)}{\rho(\theta) \cdot A_c} \tag{5.1}$$

The five correlations are evaluated both as published and after a global fit of their leading constants. The constants are obtained by minimising the root-mean-square deviation between the predicted and the measured heat flux, summed over all crank angles and operating points, with the constants shared across runs and the surface-by-surface flux reconstructed from a single gas-side coefficient and the surface temperature difference.

5.5 Spectral Analysis of Pressure Pulsations

The suction pressure carries pulsations that must be separated into the kinematic orders forced by the piston motion and the acoustic resonance of the suction line. The fast suction pressure $p_{suc,hs}$ and the suction flow are each transformed to the frequency domain by Welch's method [88], which averages the periodograms of overlapping segments so that the scatter between segments gives the error bars on the order amplitudes.

The spectrum is organised by engine order. The k^{th} order lies at

$$f_k = \frac{k \cdot N}{60} \tag{5.2}$$

Where N is the shaft speed in revolutions per minute, so the first order coincides with the shaft frequency near 24 Hz and the second with 48 Hz. Their amplitudes are denoted A1 and A2.

The suction line behaves as a tube open at the vessel and closed at the valve (Section 1.5), whose quarter-wave acoustic modes lie at

$$f_m = \frac{(2m-1) \cdot c_s}{4L_s} \tag{5.3}$$

A coincidence in frequency does not by itself prove an acoustic resonance, because the second order is also present as a kinematic harmonic. The two are separated by a mode-shape test. A standing acoustic wave has a pressure antinode and a velocity node at the closed valve, so the resonant order is amplified in the pressure signal relative to the flow signal, whereas a kinematic harmonic appears in the same proportion in both. The discriminator is the ratio of the second to the first order measured in pressure against the same ratio measured in flow,

$$\Phi = \frac{\left(\frac{A_2}{A_1}\right)_p}{\left(\frac{A_2}{A_1}\right)_V} \tag{5.4}$$

where the subscripts denote pressure and flow. A value well above unity identifies a standing acoustic wave [34].

5.6 Cycle-Derived Indices and Leakage

The in-cylinder polytropic exponent is taken as the negative slope of p_{cyl} against V, fitted separately over compression (IVC to EVO) and re-expansion (EVC to IVO). The indicated work is the area of the indicator loop, and the volumetric, isentropic and electromechanical efficiencies defined in Section 1.3 are evaluated from the delivered mass measured by the TSI flow meter, the isentropic reference between the suction and discharge states, and the electrical and

shaft powers of the drive.

An independent check on the reconstruction and on leakage is the energy residual of the closed phases,

$$E_{miss} = \frac{c_v}{R} \Delta(pV) + W + Q \tag{5.5}$$

formed from the measured cylinder pressure, volume and wall heat flux, where the first term is the change of internal energy of the trapped gas. A non-zero residual signals an enthalpy flux that the closed-system balance does not account for, that is, leakage or backflow through a nominally closed valve [23].

Comparing the three in-cylinder pressures first requires removing the independent zero offset of each transducer, which is done on the open-valve phases where the cylinder pressure equals the chamber pressure. The piston-ring blow-by is then computed with the clearance-flow model introduced in Section 1.6 [40],

$$\dot{m}_{ring} = \pi D \rho \left(C_u \cdot g \cdot u_p \; + \; C_p \cdot g^3 \cdot \frac{(p_{cyl} - p_h)}{\mu \cdot L_r} \right) \tag{5.6}$$

shear-driven and a pressure-driven flow through the annular gap between piston and cylinder, where C_u and C_p are the gap shape factors, g the radial clearance and L_r the ring land length. Subsequent numerical studies have used the same clearance-flow model [38], [39]. The valve backflow is treated as a compressible orifice flow driven by the trans-valve pressure difference [24],

$$\dot{m} = C_d A p \sqrt{\frac{2\kappa}{(\kappa - 1)RT} \left(r_p^{\frac{2}{\kappa}} - r_p^{\frac{\kappa+1}{\kappa}} \right)} \tag{5.7}$$

with discharge coefficient C_d, effective area A, upstream pressure p and pressure ratio r.

The discharge-valve backflow during re-expansion is quantified by three independent routes that are required to agree. The energy residual above, the integral of the orifice driving across the valve, and the deviation of the re-expansion exponent from the adiabatic value.

5.7 Uncertainty Analysis

The experimental heat flux reported in this work is the end product of a multi-step calculation chain. The surface temperature signal is converted from EMF to temperature, ensemble-averaged over approximately 235 revolutions, filtered, and inverted to heat flux by the CF formula. The comparison with correlation predictions then requires the additional step of reconstructing the instantaneous gas temperature T_{gas}, from which the gas properties and the driving temperature difference are derived. Uncertainties from several independent sources enter at different

stages of this chain and propagate to the final result. This section identifies and quantifies the individual contributions, so that the confidence with which the experimental results can be interpreted, and compared with correlation predictions, is established before the results are presented. The contributions are grouped, following the established convention, into Type A uncertainties evaluated statistically from the measured data, namely the cycle-to-cycle scatter and the calibration residual. Type B uncertainties evaluated from instrument specifications and calibration certificates, namely the sensor and acquisition accuracies, the thermal product, the cold-junction compensation, and the pressure reference. The combined standard uncertainty is the root sum of squares of the two.

Thermocouple Thermal Product

The thermal product enters the CF inversion as a multiplicative prefactor. The heat flux is directly proportional to β, so that a relative uncertainty $\delta\beta/\beta$ propagates as

$$\frac{\delta\dot{q}}{\dot{q}} = \frac{\delta\beta}{\beta} \tag{5.8}$$

The spread among the three sensors is less than 0.5 %, which suggests good manufacturing consistency but provides no information about the absolute accuracy of the calibration. In the absence of an independent calibration or a manufacturer-stated tolerance, the uncertainty in β cannot be rigorously quantified. As a practical estimate, a ±5 % uncertainty in β, a value broadly consistent with the scatter reported in the literature for similar coaxial thermocouple constructions, would translate directly into a ±5 % uncertainty in the experimental heat flux. The thermal product thus represents a systematic scale factor that shifts all heat flux values by the same proportion. It does not affect the shape of the crank-angle-resolved profiles.

Junction Overheating

The finite thickness of the insulating layer between the two thermocouple electrodes introduces lateral heat exchange between them, causing the junction temperature to deviate from the true surface temperature. This effect, junction overheating, produces a systematic positive bias in the inferred heat flux. For coaxial thermocouples with typical insulation thicknesses, this bias is of the order of 2 to 3 % of the peak heat flux [83]. The effect is built into the coaxial thermocouple construction and cannot be eliminated without reducing the insulation thickness below practical manufacturing limits. In the present work, no correction for junction overheating is applied. The bias is acknowledged as a systematic contribution of the order of +2 to +3 % on the heat flux amplitude.

Installed Error

The thermocouple body has a thermal product of approximately 8600 $W \cdot s^{1/2} \cdot m^{-2} \cdot K^{-1}$, whereas

the surrounding cylinder wall, cast iron, has a substantially higher thermal product, estimated at approximately 11 700 $W \cdot s^{1/2} \cdot m^{-2} \cdot K^{-1}$ from published material data. The ratio $\beta_{wall}/\beta_{TC} \approx 1.36$ means that the thermocouple surface responds with a larger temperature swing than the undisturbed wall would experience under the same heat flux, because the lower thermal inertia of the thermocouple body allows it to heat up and cool down more readily. This mismatch introduces a systematic overestimation of the surface temperature amplitude, and consequently of the inferred heat flux.

The magnitude of this effect depends on the exact thermal properties of both materials and on the frequency content of the heat flux waveform. An analytical correction would require independent knowledge of the wall thermal product, which is not available from calibration but only from tabulated material data with its own uncertainty. For this reason, no correction is applied in this work. The installed error is reported as an identified systematic effect. Its implications for the comparison between the experimental and the correlation-predicted heat flux are examined in the discussion.

Pressure Measurement

The cylinder pressure does not enter the experimental heat flux calculation, which is derived solely from the surface temperature via the CF inversion. It does, however, play a central role in the reconstruction of T_{gas} and therefore in the evaluation of the correlation predictions.

The cylinder pressure is measured by a Kulite HKS-11HP-375 transducer (35 bar full scale, ±0.1 % FSO BFSL typical, ±0.5 % FSO maximum). The maximum specification corresponds to an absolute uncertainty of ±0.175 bar. More important for the reconstruction is the zero level. It is anchored by the two-stage zero-level correction of Section 5.3, whose residual is approximately ±0.05 bar, about ±5 % of the cylinder pressure at the IVC reference state. It propagates directly into the trapped mass and the level of the reconstructed temperature. The relative uncertainty in T_{gas} due to pressure alone follows from Equation (5.11). The suction and discharge chamber pressures, measured by Kulite HKL-375M differential transducers (3.45 bar and 17.2 bar full scale, ±0.1 % FSO BFSL typical), enter the phase boundary detection and the Disconzi correlation through the characteristic velocity [9].

$$\frac{\delta T_{gas}}{T_{gas}} = \frac{\delta p}{p} \tag{5.9}$$

The voltage-to-pressure relation of each transducer was obtained by an in-situ calibration against the vessel pressure, measured by a BD Sensors DMP331 transmitter (0 to 20 bar, ±0.35 % FSO) read through a 0.01 % precision shunt resistor on a 1 to 5 V channel. The calibration spanned eleven pressures from 0 to 11.5 bar and is linear to a residual of 17 mbar root mean square (43 mbar maximum) for the cylinder transducer. Because the relation is fitted against the vessel reference, the gain of the transducer and amplifier is removed. The absolute pressure scale is limited instead by the reference transmitter. This is a Type B uncertainty of about ±0.07 bar over its range, rather than by the Kulite or the amplifier, whose own specifica-

tion is not available. The fitted residual is the only Type A contribution from the pressure chain. The fast suction transducer was not part of this calibration and retains its nominal scale, because it is used only for the oscillation and phase analysis, where the absolute scale is immaterial. For the gas-temperature reconstruction the zero anchor acts as an offset on the trapped-mass reference and dominates. The reference scale acts only as a proportional factor of about 0.35 %. This is of the order of 2 K at the peak, and instead governs the absolute-pressure quantities, the pressure ratio, the indicator diagram, and the polytropic exponent.

Table 5.5 Sensitivity of the reconstructed gas temperature to the principal input uncertainties

Perturbation	**Effect on T_{gas} level**	**Effect on peak T_{gas}**
Pressure zero anchor ±0.05 bar	±9 to 18 K	±26 to 47 K
EVC position ±1°	±2 to 5 K	±2 to 4 K
Thermal product β ±5 %	±0.1 to 2.2 K	±0.2 to 4.1 K
Suction temperature T_{suc} ±0.5 K	±0.7 to 0.8 K	±0.9 to 1.2 K

The sensitivity of the reconstruction to these inputs was quantified by repeating the full calculation with each input perturbed within its uncertainty band. Table 5.5 summarises the resulting spread of the gas temperature. The suction-temperature row reflects the ±0.5 K thermocouple tolerance alone. Its full measurement uncertainty of about ±1.5 °C, which includes the Graphtec module and its internal cold-junction compensation, scales these figures by roughly three, to about ±2 to 4 K, still well below the pressure contribution.

Cycle-to-cycle variability

The surface temperature and pressure signals are ensemble-averaged over few hundred complete revolutions for each measurement, and the standard deviation across cycles is computed at each crank-angle position. For a typical standard deviation of the surface temperature of the order of 0.1 K, the standard uncertainty of the mean is approximately $0.1/\sqrt{235} \approx 0.007$ K, negligible compared to the systematic contributions discussed above. The cycle-to-cycle variability is not a dominant source of uncertainty in the ensemble-averaged heat flux, though an unusually large standard deviation at a particular crank angle may serve as a diagnostic of physical instabilities such as valve flutter or intermittent leakage.

The resolution of the two acquisition systems was also examined. The fast surface-temperature channels are digitised by a 24-bit NI 9238 module on a ±500 mV range, a quantisation step of about 0.001 K that is negligible against the 0.3 to 1.0 K temperature swing. The Graphtec modules are 16-bit, which corresponds to about 0.001 bar on the pressure channels and is also negligible. The ability to resolve the sub-kelvin swing therefore rests on the acquisition resolution together with the ensemble averaging over approximately 235 revolutions, not on either alone.

Reconstruction of Gas Temperature

The instantaneous bulk gas temperature $T_{gas}(\theta)$ is not required for the experimental heat flux but is essential for the correlation comparison. The gas properties entering the Reynolds and Prandtl numbers are evaluated at T_{gas}, and the temperature difference ($T_{gas} - T_{wall}$) converts the correlation-predicted Nusselt number to heat flux. The uncertainty in T_{gas} therefore affects the correlation side of the comparison rather than the experimental side. T_{gas} is reconstructed from the measured cylinder pressure, the cylinder volume, and the gas mass determined from the ideal gas law at a reference state, with three primary contributions to its uncertainty.

First, the gas mass is derived from the reference state at IVC. Uncertainties in p_{IVC} (from the Kulite transducer), in V_{IVC} (from the crank mechanism geometry), and in T_{suc} (whose measurement uncertainty is about ±1.5 °C, combining the type-T tolerance of ±0.5 K with the Graphtec module accuracy and its internal cold-junction compensation). These propagate multiplicatively into m and hence into T_{gas} at every crank angle during the closed-valve phases.

Second, the cylinder volume $V(\theta)$ depends on the crank angle through the crank-slider kinematics. The crank angle is assigned by dividing each revolution, bounded by the encoder index pulse, into 1440 equal steps. The small sensitivity of the cylinder volume to angular error near TDC makes the volume uncertainty a minor contributor to the overall T_{gas} uncertainty.

Third, during the valve-open phases the gas mass is not constant and T_{gas} cannot be determined from the ideal gas law with a fixed mass. During suction, the mass profile is reconstructed from the Sensirion SFM3000 instantaneous flow measurement scaled to the TSI 4040 time-averaged reference (Section 5.3). During discharge, T_{gas} is obtained by linear interpolation between the last compression point and the first expansion point. Both approaches introduce additional uncertainty that is difficult to quantify rigorously, and the valve-open phases are the portions of the cycle where T_{gas} carries the highest uncertainty.

Correlation Sensitivity to Gas Temperature

The comparison between the experimental heat flux and the correlation predictions depends on T_{gas} in two distinct ways. It enters through the gas properties that enter the correlation Reynolds and Nusselt numbers, and through the driving temperature difference that converts the correlation-predicted HTC to heat flux. The temperature difference passes through zero twice in each revolution, and the correlation-predicted heat flux becomes indeterminate in the immediate vicinity of these crossings regardless of the quality of the correlation itself.

Even far from the crossings, the uncertainty in T_{gas} propagates significantly. At crank angles where the temperature difference is large (for example, near TDC, where $T_{gas} - T_{wall}$ may exceed 50 K), a ±5 K uncertainty in T_{gas} produces a relative uncertainty of approximately ±10 % in the correlation-predicted heat flux. Near the zero crossings, the same uncertainty renders the comparison physically meaningless, which is why these regions are excluded from the analysis (Section 5.4). T_{gas} is therefore the single most influential parameter in the uncertainty of the correlation comparison [89]. The sensitivity is particularly pronounced at low pressure ratios,

where the gas temperature swing is small and the temperature difference remains close to zero over a larger fraction of the cycle.

The sensitivity to the reconstruction scheme itself was checked by repeating the entire chain, from the gas temperature to the global fit of the correlation constants, with the alternative scheme that integrates the energy balance over the whole cycle. The fitted leading constants change by 10 to 17 %. The ranking of the correlations and the trends with pressure ratio are preserved. The only scheme-sensitive parameter is the inflow Stanton number of the Aigner correlation, which changes by a factor of about five. It depends on the bulk gas-to-wall temperature difference during suction, and that is the quantity in which the two schemes differ most. The conclusions about the structure of the correlations do not rest on the choice of the reconstruction scheme.

Table 5.6 Principal contributions to the uncertainty of the experimental heat flux and heat transfer coefficient

Contribution	**Magnitude**	**Character**
Thermal product β	±5 % (estimated)	proportional effect on $\dot{q}$ (Equation 5.8)
Junction overheating	+2 to +3 %	systematic positive bias, not corrected
Installed error (β mismatch)	systematic overestimation	identified, not corrected
Cylinder pressure	zero level corrected for each run (Section 5.3), residual ±0.05 bar (≈±5 % of p_{IVC})	enters the gas-temperature reconstruction
Savitzky–Golay filter	window-width sensitivity	affects temporal distribution of $\dot{q}$
Cycle-to-cycle variability, encoder resolution	negligible	suppressed by ensemble averaging
Combined (closed-valve phases)	±10 to ±15 %	higher during valve-open phases and near ΔT crossings

The uncertainty in the experimental heat flux is governed by three systematic contributions (Table 5.6). These are the thermal product β, junction overheating, and the installed error due to the β mismatch between the thermocouple and the cylinder wall. Two model assumptions enter in addition. The gas is treated as well mixed, with a single bulk temperature at each crank angle, and the piston surface, which is not instrumented, is treated as adiabatic in the heat input to the energy balance. Both are assessed in Chapter 6. A further Type B contribution is the

pressure reference, the BD Sensors vessel transmitter against which the cylinder transducers are calibrated, at about ±0.07 bar on the absolute pressure but only a proportional effect of the order of 2 K on the reconstructed temperature. In the figures the statistical, Type A, uncertainty is drawn as a band on the crank-angle-resolved results, whereas the systematic, Type B, uncertainty, which shifts all values together, is stated in the text rather than drawn, to avoid a false impression of point-to-point scatter.

The correlation comparison introduces a largely independent source of uncertainty through the reconstruction of T_{gas}. During the closed-valve phases, where T_{gas} is well constrained and the temperature difference is large, the combined uncertainty is of the order of ±10 to ±15 %. During the valve-open phases and near the gas-wall temperature crossings, it is considerably higher.

6 RESULTS AND DISCUSSION

This chapter presents the experimental results in the order of the processing chain of Chapter 5 and then compares them with established heat transfer correlations. It opens with a preliminary steady-state characterisation of the compressor across the full range of operating conditions. These data come from cycle-averaged measurements that preceded the crank-angle-resolved campaign. A numerical validation of the thermocouple installation follows, with its consequences for how the HTC is evaluated. The remaining sections give the crank-angle-resolved results for all measured pressure ratios, so the effect of the pressure ratio on in-cylinder heat transfer can be assessed. Most of the supporting sections serve a single purpose, the reconstruction of the instantaneous gas temperature, which is the central challenge of the work. The HTC and every correlation are referenced to a temperature that cannot be measured. The cylinder pressure, the valve timing, the leakage, and the suction flow are each needed to close the mass and energy balance from which it follows. A few of these analyses were forced by the data, where an unexplained feature had to be resolved before the correlation comparison could be trusted.

6.1 Preliminary Steady-State Characterisation

This section draws on a preliminary campaign [86] that characterised the compressor across nineteen operating conditions (PR = 1.05–11.05) at 70 and 71 S/s. The campaign was designed to test whether crank-angle-resolved measurement is needed. As a steady-state measurement methodology it serves well, but it cannot resolve the instantaneous gas temperature or the within-cycle heat flux. The instrumentation consisted of coaxial type-E thermocouples on the inner surface ($T_{wall,C1}$ (top), $T_{wall,C3}$ (bottom), $T_{wall,VP}$ (valve plate)), a type-T discharge gas thermocouple (T_{dis}), and a thermoelectric heat flux sensor on the outer wall. A re-analysis of the raw data has shown findings not reported in the previous publication. These are the actual shaft frequency, the 50 Hz mains interference, and a corrected phase-averaging procedure that recovers the crank-angle temperature swing.

The compressor is driven by a single-phase asynchronous motor with a rated speed of 1405 RPM. The publication ([86] assumed this speed to be constant across all operating conditions. The phase-folding procedure assigns the crank angle to each sample by Equation (6.1). An error in f_{shaft} builds up a drift over the roughly 700 averaged revolutions and smears the phase-averaged profile. The actual shaft frequency was found from a zero-padded fast Fourier transform (FFT) of the coaxial thermocouple signals. Because these signals are electromagnetically shielded, they show a clear spectral peak at the shaft frequency for PR > 2.

$$\theta = 360° \cdot frac(t \cdot f_{shaft}) \tag{6.1}$$

The extracted shaft speed varies from 1478 RPM (slip 1.5 %) at no-load to 1403 RPM (slip

6.5 %) at maximum load (Fig. 6.1), following the classical torque–slip characteristic. The rated value of 1405 RPM corresponds to the maximum-load operating point. At all intermediate conditions the actual speed exceeds the rated speed by 1–5 %, i.e. a frequency offset of 0.3–1.2 Hz. As shown below, this offset is sufficient to degrade the phase-averaged profiles substantially.

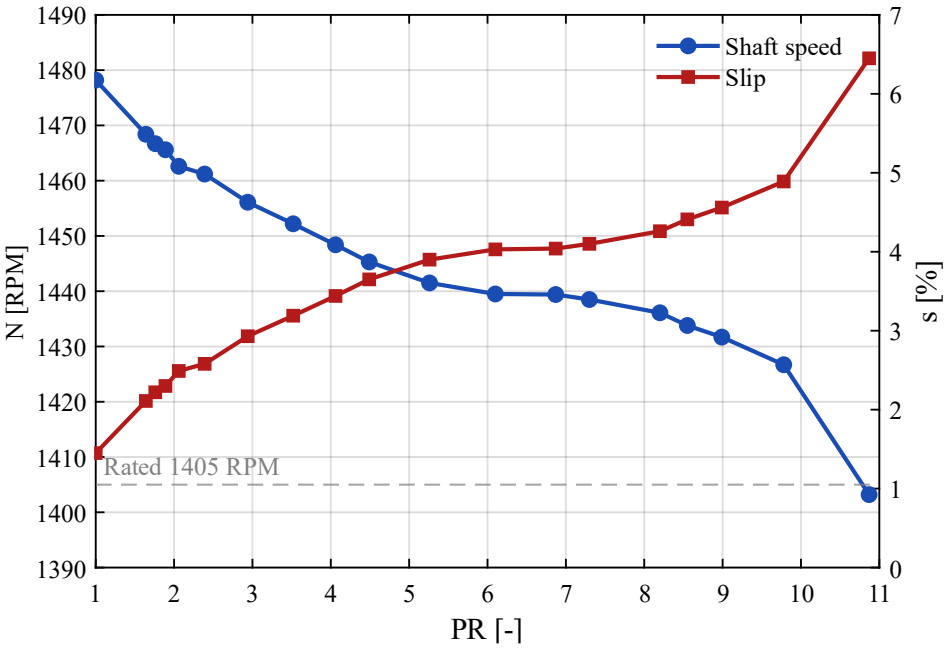

Figure 6.1 Measured shaft speed and motor slip as a function of pressure ratio, extracted from spectral analysis of the coaxial thermocouple signals. The dashed line indicates the rated speed of 1405 RPM

A point-by-point evaluation of the polytropic exponent shows a systematic variation with pressure ratio (Fig. 6.2), in contrast with the single value $n = 1.22$ reported in the previous publication [86]. The preliminary rig carried no pressure sensor inside the cylinder. The exponent is therefore evaluated from the polytropic temperature relation, using the measured suction temperature, the discharge line temperature T_{dis} and the pressure ratio. The result is an apparent exponent of the whole suction-to-discharge process, not the exponent of the in-cylinder compression alone. A fitted exponent of this kind absorbs the combined effect of gas-to-wall heat transfer, friction and real-gas behaviour [23]. The present value also contains the valve throttling and the partial cooling of the gas upstream of the T_{dis} sensor. At low pressure ratios the apparent exponent reaches $n = 1.64$ and exceeds the isentropic value $\kappa = 1.4$. The useful compression work is small there, so friction, throttling and re-expansion raise the discharge temperature well above the polytropic prediction. As the pressure ratio increases, the compression work dominates and the apparent exponent decreases monotonically to $n = 1.22$. An exponent below κ corresponds to net heat rejection from the gas [57].

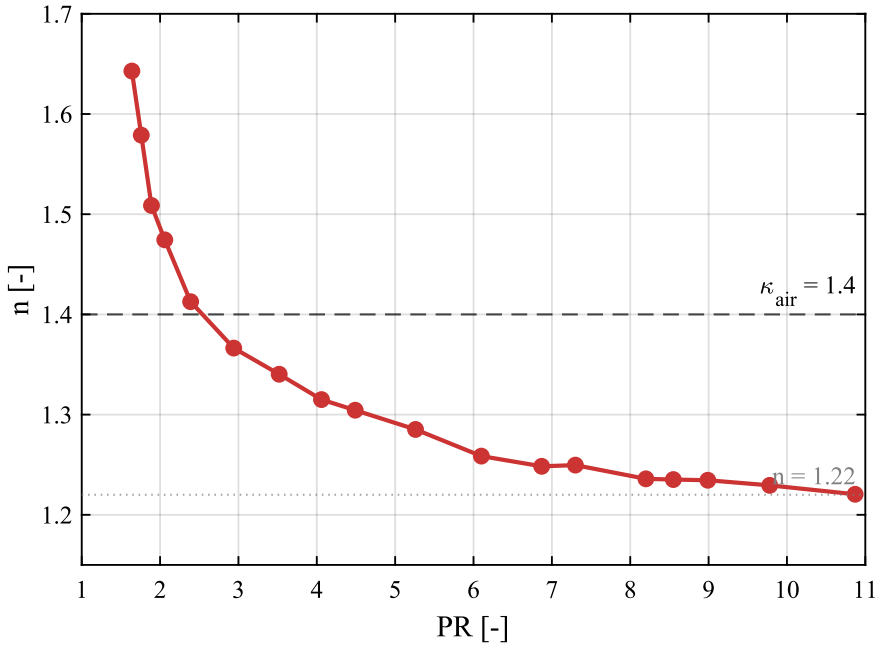

Figure 6.2 Apparent polytropic exponent of the suction-to-discharge process as a function of pressure ratio. The horizontal dashed line indicates the isentropic exponent for air (κ = 1.4). At low pressure ratios the apparent exponent exceeds κ because parasitic losses dominate. At high pressure ratios it approaches n = 1.22, consistent with net heat rejection from the gas. (Re-analysis of data from [86])

All cycle-averaged temperatures increase monotonically with pressure ratio, with an axial gradient consistent with the dominant heat source at the cylinder head (Fig. 6.3). The outer surface temperature exceeds the inner surface temperature at all operating conditions. This counterintuitive inversion is explained by axial conduction through the cylinder wall from the hot valve plate and cylinder head. The inner surface is periodically cooled by the incoming suction charge (near ambient temperature), while the outer surface temperature is sustained by the axial heat flux from the head end. This interpretation is consistent with published thermal models [23], [58].

The near equality of the suction and discharge chamber surface temperatures on the cylinder head indicates substantial suction gas superheating before the gas enters the cylinder, consistent with the measurements of Morriesen [3].

At low and moderate pressure ratios, the discharge gas temperature (T_{dis}) exceeds the valve plate surface temperature ($T_{wall,VP}$), as expected. Above PR ≈ 9, however, the valve plate temperature rises above the discharge gas temperature (Fig. 6.4). The crossover occurs because the valve plate accumulates thermal energy during the discharge phase and retains it through its thermal mass and the heat input from the cylinder head. The sensor T_{dis}, by contrast, sits downstream of the discharge valve, where partial cooling has already occurred. At high pressure ratios the valve plate thus becomes a direct source of suction gas superheating, representing a second pathway in addition to the axial wall conduction discussed above. This finding is consistent with the CFD analysis of Pereira [48] and the lumped-parameter model of Ooi [51].

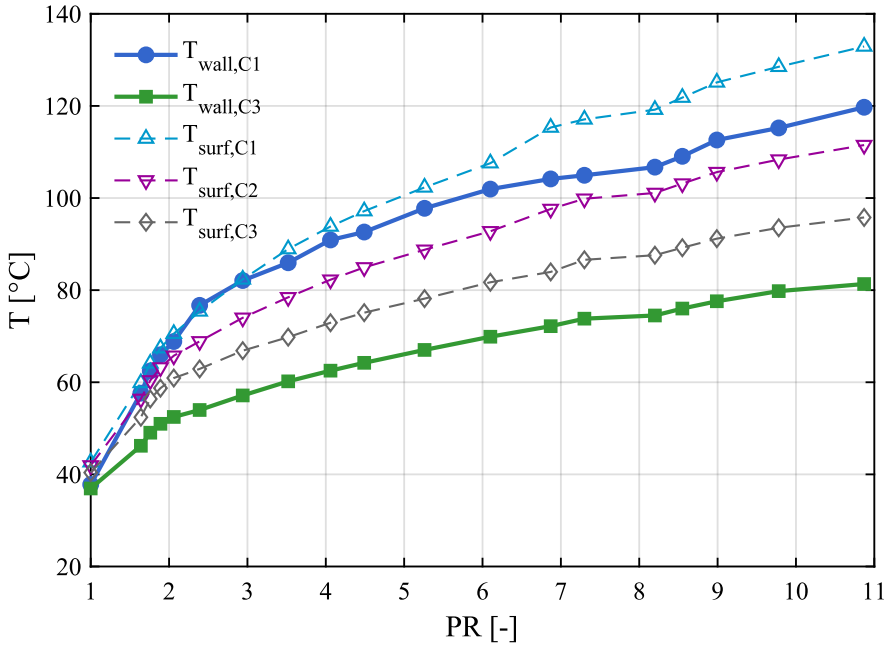

Figure 6.3 Cycle-averaged surface temperature at inner ($T_{wall,C1}$, $T_{wall,C3}$) and outer ($T_{surf,C1}$–$T_{surf,C3}$) positions on the cylinder wall as a function of pressure ratio (Re-analysis of data from [86])

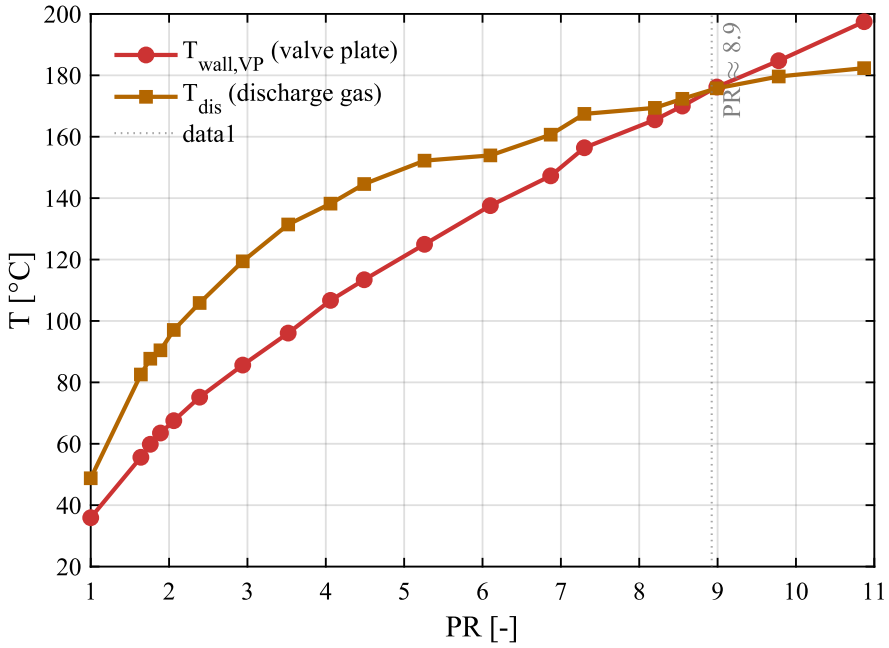

Figure 6.4 Comparison of valve plate inner surface temperature ($T_{wall,VP}$) and discharge gas temperature (T_{dis}) as a function of pressure ratio, showing the crossover at approximately PR ≈ 9. (Re-analysis of data from [86])

A thermoelectric heat flux sensor (gSKIN-XM, greenTEG) on the outer cylinder surface at mid-height measured the external heat flux (Fig. 6.5), converted using an individual temperature-dependent calibration. The measured heat flux increases from approximately 0.8 kW/m² at no-load to approximately 3.5 kW/m² at maximum pressure ratio. The sensor's time constant ($\tau \approx 0.53$ s, spanning ~13 shaft revolutions) limits the measurement to the cycle-averaged heat flux. Even so, it provides the only direct quantification of the external thermal boundary con-

dition and anchors the overall energy balance.

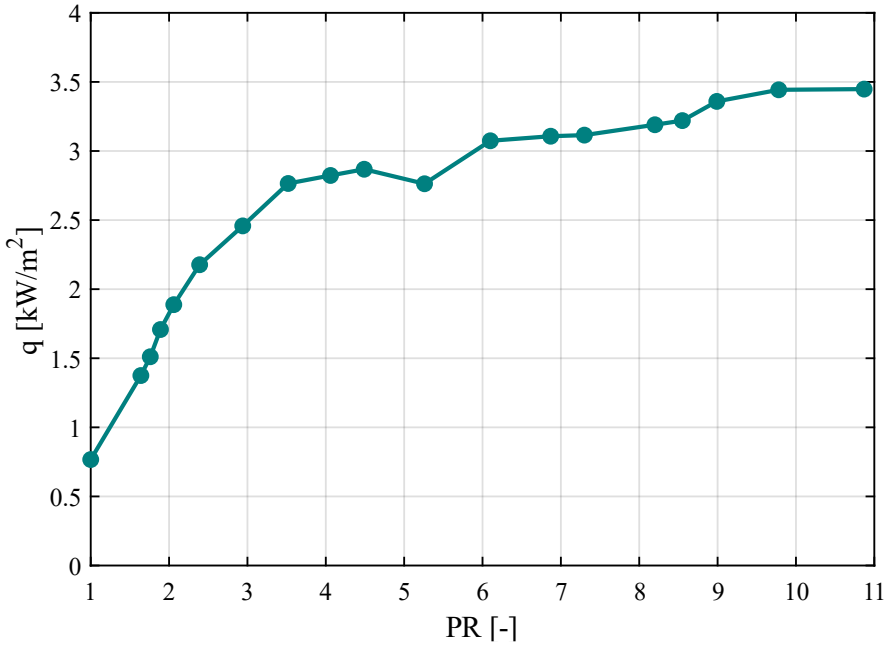

Figure 6.5 Heat flux from the outer cylinder surface to the ambient, measured by the thermoelectric heat flux sensor (gSKIN-XM), as a function of pressure ratio [86]

The previous publication [86] reported no statistically significant crank-angle dependence of the wall temperature. A spectral re-analysis shows that this conclusion was partly caused by unrecognised 50 Hz mains interference aliased into the measurement bandwidth. At f_s = 70 S/s the 50 Hz component folds to $|70 - 50| = 20$ Hz. At f_s = 71 S/s it shifts to 21 Hz, which matches the observed dominant peaks in the type-T thermocouple spectra. The 1 Hz shift between datasets confirms the aliasing mechanism, because the shaft-frequency peak stays at the same position in both spectra while the alias shifts by exactly 1 Hz. The aliased component has an amplitude comparable to the expected physical temperature swing, so it masks any cycle-coherent fluctuation in the unshielded type-T signals. The coaxial thermocouples are electromagnetically shielded by their geometry, so they are much less susceptible to the 50 Hz interference. Their shaft-frequency component is identifiable above the noise floor at all conditions above about PR = 2.

Using the correct shaft frequency for phase-averaging, a systematic crank-angle-dependent temperature swing emerges at each operating condition (Fig. 6.6). The valve plate sensor ($T_{wall,VP}$) has the largest swing, increasing from 0.38 °C at PR = 5.26 to 1.03 °C at PR = 9.78 (Fig. 6.7). The cylinder top sensor ($T_{wall,C1}$) shows a consistently smaller swing of 0.27–0.66 °C. This spatial hierarchy ($T_{wall,VP} > T_{wall,C1}$) reflects the stronger thermal forcing at the valve plate, which remains in direct contact with the gas throughout the cycle. The cylinder bottom sensor ($T_{wall,C3}$) has a negligible swing, consistent with piston shielding during the compression and expansion phases. This position is excluded from the subsequent heat flux evaluation. The mid-height coaxial thermocouple failed during the campaign. It would have given the most informative comparison with the external heat flux sensor at the same axial position. The high-speed sensor layout was designed to ensure redundant coverage of this position.

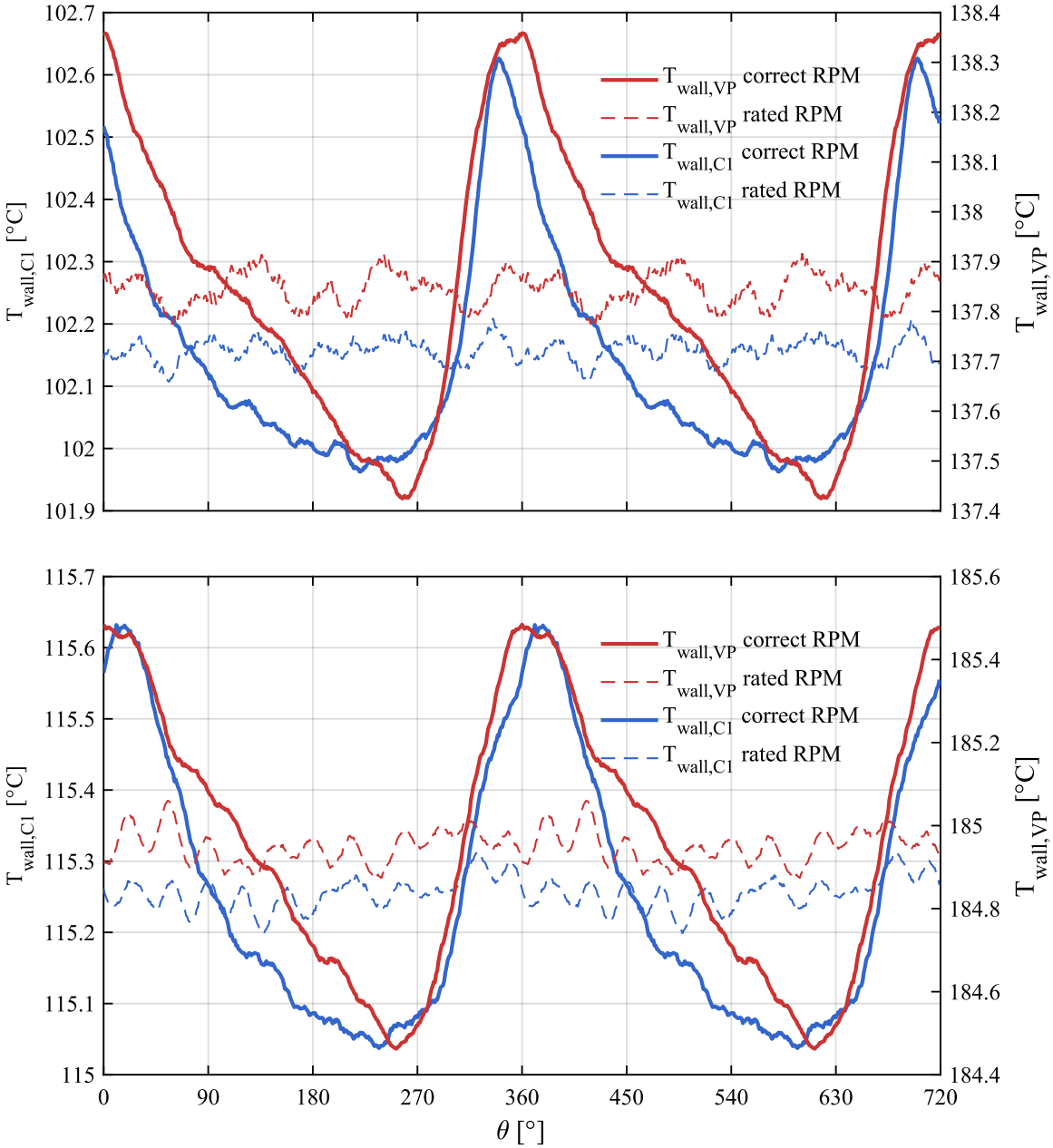

Figure 6.6 Phase-averaged temperature profiles as a function of crank angle for the three coaxial thermocouple positions ($T_{wall,C1}$, $T_{wall,C3}$, $T_{wall,VP}$), reconstructed using the correct shaft frequency (solid lines) and the rated shaft frequency (dashed lines). (a) PR = 6.10; (b) PR = 9.78. (Re-analysis of data from [86])

At moderate pressure ratios (e.g. PR = 6.10, Fig. 6.6a), the $T_{wall,VP}$ profile gives a gradual rise during compression and discharge ($\theta \approx 0$–$180°$) and a decline during expansion and suction ($\theta \approx 180$–$360°$), consistent with the expected thermal response of a semi-infinite solid to periodic heat flux [13]. At PR = 9.78 (Fig. 6.6b), the swing exceeds 1 °C on the valve plate, within the range of 0.5–2 K reported by Disconzi [9] and Reichelt [13] for comparable machines.

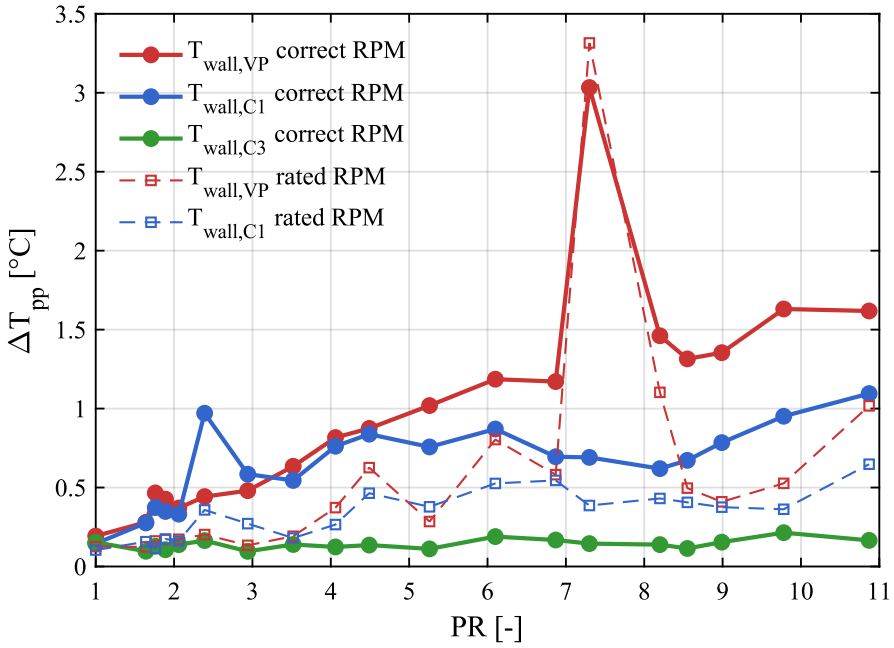

Figure 6.7 Peak-to-peak temperature swing as a function of pressure ratio for all three coaxial thermocouple positions $T_{wall,VP}$ (valve plate), $T_{wall,C1}$ (cylinder top), and $T_{wall,C3}$ (cylinder bottom). Both the swing obtained with the correct shaft frequency (filled symbols) and the swing obtained with the rated rpm (open symbols) are shown. (Re-analysis of data from [86])

At maximum pressure ratio (PR = 10.87, 1000 kPa), the reconstruction degrades significantly due to the shortest measurement duration, a spectral inconsistency between the two sampling rates, and the near coincidence of actual and rated speed (1403 vs 1405 RPM) that eliminates the benefit of the shaft frequency correction. Consequently, PR = 9.78 is used as the reference condition for the highest-quality reconstruction from this dataset.

The importance of the shaft frequency correction is shown by a direct comparison of the phase-averaged profiles (Fig. 6.6). The rated-speed profiles appear substantially flatter, with a reduced swing and loss of waveform shape. The smearing factor, the ratio of correct to rated swing, ranges from 1.2 at low pressure ratios (small motor slip) to 3.1 at PR = 9.78 (large slip). At this condition, the valve plate swing is 1.03 °C with the correct frequency but only 0.53 °C with the rated speed. This smearing mechanism, combined with the 50 Hz interference contaminating the type-T thermocouples, explains why the study [86] concluded that no crank-angle dependence was detectable. This re-analysis shows that this conclusion, while consistent with the procedure used at the time, does not reflect the actual physical behaviour. The cycle-averaged temperatures, polytropic analysis, and external heat flux reported by Bouchal [86] remain unaffected, because these quantities are computed from time-averaged signals independent of the phase reference.

Given the recovered temperature profiles, an attempt was made to evaluate the instantaneous heat flux using the spectral formulation of the semi-infinite heat flux inversion [67], [90]. At 70 S/s and $f_{shaft} \approx 24$ Hz, however, only ~2.9 samples in each revolution are available, limiting the resolvable harmonics to $n_{max} = 1$ (compared with $n_{max} \approx 1041$ at the 50 kHz rate used in the high-speed campaign). The resulting heat flux estimates of 50–180 kW/m² are clearly non-

physical, because the Fourier decomposition attributes residual scatter to higher harmonics, which the amplification factor magnifies. The conclusion is clear. The low-frequency sampling can detect the existence and the approximate magnitude of the temperature swing. It cannot provide the spectral bandwidth required for a quantitative heat flux evaluation. This is consistent with the fact that all successful studies in the literature used sampling rates at least two orders of magnitude above the shaft frequency [6], [8], [13].

The re-analysis yields four conclusions with direct implications for the high-speed campaign. First, the shaft speed variation across the operating range must be accounted for in phase-averaging. The high-speed campaign eliminates this issue through a shaft encoder. Second, the original report of no detectable temperature swing resulted from the combination of 50 Hz interference and rated-speed smearing. When both are corrected, a physically plausible swing consistent with the literature is recovered. Third, quantitative heat flux evaluation requires the spectral bandwidth provided by the 50 kHz system. Fourth, only the valve plate and cylinder top yield useful crank-angle data. The high-speed sensor layout addresses the remaining limitations. The preliminary campaign therefore provides the steady-state context for the high-speed results of the following sections. The re-analysis establishes the quantitative limitations that the new acquisition system was designed to overcome.

6.2 Validation of Thermocouple Installation

Before interpreting the high-speed surface temperature measurements quantitatively, the influence of the coaxial thermocouple installation on the measured temperature and the derived heat flux must be assessed. This section summarises the findings of a dedicated numerical study [89], extends the analysis with a literature comparison, and discusses the implications for the data processing adopted in subsequent sections.

The study [89] used a transient CFD simulation (ANSYS Fluent 2024 R1) of a simplified geometry. Air flows at a constant velocity of 2.5 m/s, equal to the mean piston speed of the EK 4-2 compressor, along a 3 mm thick cast iron wall. The wall contains three cylindrical inserts flush with the inner surface. The first insert is of the same material as the wall and serves as the reference. The second has the thermal properties of an MCT-19 type E coaxial thermocouple mounted directly (TC_1). The third has the thermocouple separated from the wall by a plastic (SLA resin) insert (TC_2). The inlet air temperature oscillated sinusoidally between the suction and discharge temperatures at the shaft frequency, simulating two operating conditions, PR = 4.1 (T_{peak} = 105 °C) and PR = 8.7 (T_{peak} = 170 °C). The outer surface was set to free convection (h = 10 W/m²K). Full details of the mesh (615k polyhedral cells), boundary conditions, and convergence criteria are given in the previous publication [89].

The sinusoidal temperature boundary condition is a simplification. However, the Morriesen [3] measurements confirm that the fundamental harmonic dominates the actual gas temperature waveform, and the thermocouple installation error depends on the ratio of material properties rather than on the waveform details.

The semi-infinite solid assumption underlying the CF formulation requires that the thermal penetration depth be substantially smaller than the wall thickness. For periodic heating at ω = 141.4 rad/s, the penetration depth at which the surface oscillation is damped to one thousandth of its amplitude is 3.0 mm for cast iron and 2.2 mm for the thermocouple material. The 3 mm cylinder wall therefore satisfies the condition marginally for cast iron and comfortably for the thermocouple. The MCT-19 thermocouple body, with a length of approximately 10 mm, exceeds the required 2.2 mm by a factor of 4.5. These results confirm that the semi-infinite treatment is valid for both the wall material and the thermocouple at the operating frequencies of the present compressor.

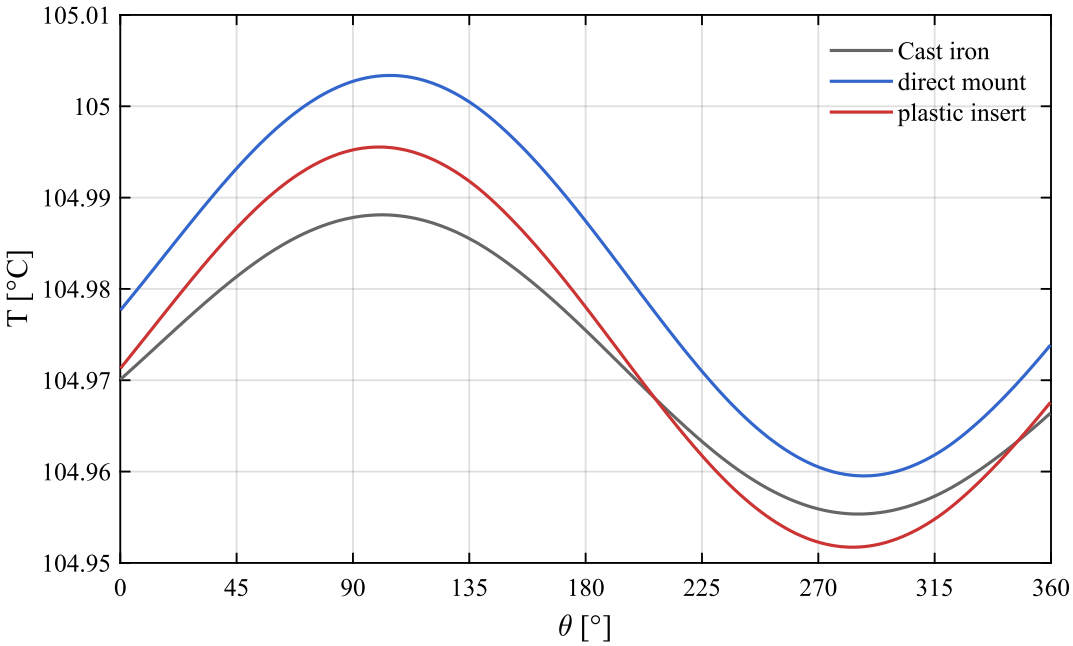

Figure 6.8 Surface temperature over one cycle from the CFD simulation (PR = 8.7, T_{peak} = 170 °C) for the undisturbed cast iron surface, the directly mounted thermocouple, and the thermocouple with plastic insert. The differences between installations are of order 10 mK, well below the sensor resolution. [89]

The CFD results show that the differences in surface temperature between the undisturbed cast iron surface and both thermocouple installations are of order 10 mK, well below the thermocouple resolution and three orders of magnitude below the imposed gas temperature amplitude of 65 K. The thermocouple surface shows a slightly larger temperature swing than the undisturbed cast iron (about 44 mK versus 33 mK for the 170 °C peak case), because it has a lower thermal effusivity. A material with lower thermal product responds with a larger surface temperature amplitude to the same imposed heat flux. This 30 % difference in swing amplitude is, however, irrelevant for the temperature measurement itself, because both amplitudes are far below the sensor resolution. The conclusion is that the thermocouple installation does not introduce a measurable bias in the surface temperature reading (Fig. 6.8).

The effect on the calculated heat flux is larger (Fig. 6.9). The re-analysis of the CFD data gives peak-to-peak heat flux swing ratios of q_{dir}/q_{CI} = 0.98 and q_{ins}/q_{CI} = 0.98. The oscillating component of the heat flux, which carries the crank-angle-resolved information, is therefore nearly unaffected by the thermocouple installation. The mean (DC) component, however, differs more

substantially. The direct mount underestimates the cast iron mean heat flux by about 40 %, and the plastic insert by about 30 %. This decomposition shows that the installed error is mainly a bias in the cycle-averaged heat flux, not a distortion of the instantaneous waveform. That is a favourable outcome for the crank-angle-resolved analysis of the following sections.

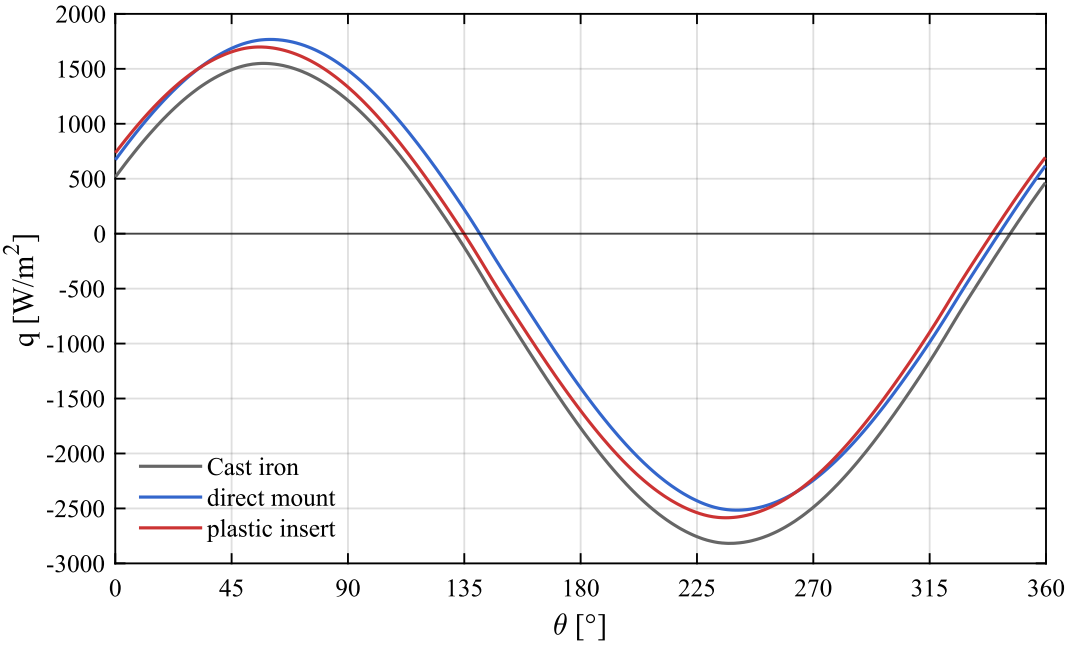

Figure 6.9 Instantaneous heat flux over one cycle from the CFD simulation (PR = 8.7, T_{peak} = 170 °C) for the undisturbed cast iron surface, the directly mounted thermocouple, and the thermocouple with plastic insert. The oscillating component is nearly identical for all three installations. The systematic offset is concentrated in the mean value [89]

To quantify the pointwise distortion, the ratio of the heat flux computed from the thermocouple surface temperature (using the thermocouple thermal product) to the heat flux through the undisturbed cast iron surface (using the cast iron thermal product) is evaluated at each crank angle. This ratio q/q_{CI} is not constant through the cycle. During the positive heat flux phase, it ranges from about 1.1 to 1.2. During the negative phase it drops to 0.6–0.9. Near the heat flux zero crossings the cast iron and thermocouple signals change sign at slightly different phase angles, an offset of 4–10°, and the ratio diverges. A single multiplicative correction factor is therefore not enough for pointwise correction (Fig. 6.10). However, given that the AC component is preserved to within 2 %, this limitation is of secondary importance for the present work.

One practical point is the choice of material properties. If the cast iron thermal product were used by mistake to process the thermocouple signal, the heat flux would be overestimated by a factor of β_{CI}/β_{TC} = 1.36 (36 % systematic error). In the present work, the manufacturer-calibrated thermal product of the MCT-19 thermocouple is used throughout, following the recommendation of Buttsworth [82] that the effective thermal product should be determined by calibration rather than from tabulated bulk material properties. Later coaxial thermocouple studies follow the same practice and treat the calibration of the effective thermal product as a necessary step for accurate heat flux evaluation [73], [77].

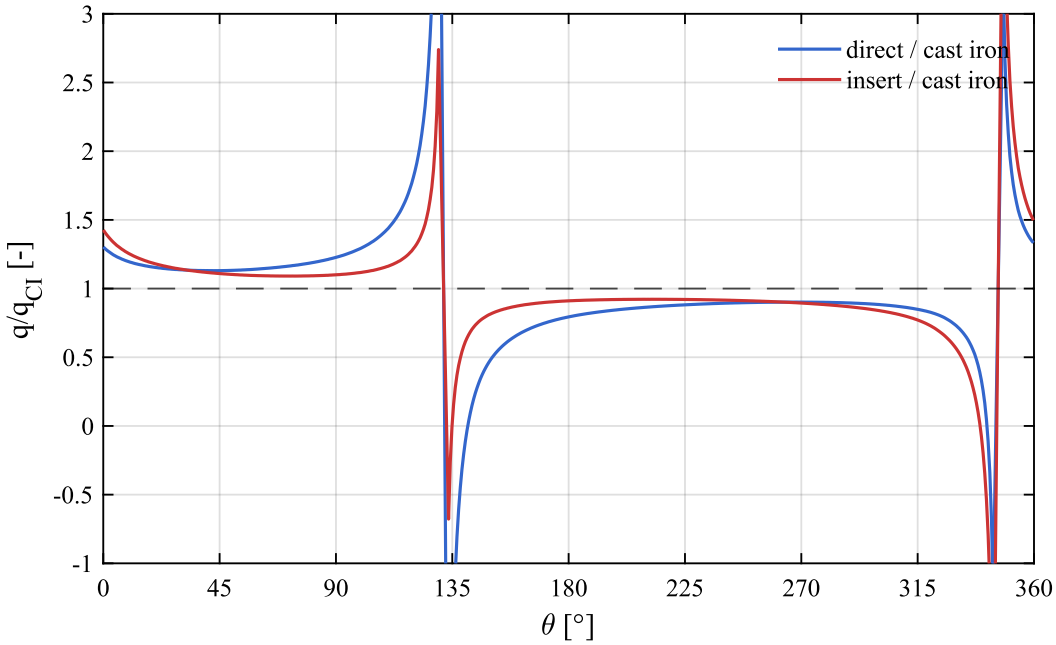

Figure 6.10 Instantaneous heat flux ratio q/q_{CI} over one cycle (T_{peak} = 170 °C)

The numerical study also showed a basic difficulty in evaluating the instantaneous HTC directly from Equation (2.3). When the gas temperature crosses the wall temperature, the denominator passes through zero and the calculation diverges, producing non-physical spikes. This singularity is not an artefact of the thermocouple installation but a limitation of the conventional HTC definition in oscillating flows. Several approaches have been proposed. The complex Nusselt number formulation of Kornhauser [47] absorbs the phase lag between heat flux and temperature difference into the correlation structure. Indirect fitting of Nusselt number correlations to the measured heat flux [14], [44] avoids pointwise HTC evaluation altogether. The implications for the present experimental evaluation are discussed in Section 6.9.

6.3 Cylinder Pressure, Valve Events, and Polytropic Exponents

Before the heat flux and the correlations, the gas state inside the cylinder has to be established. The HTC and every dimensionless group are referenced to the instantaneous gas temperature. That temperature cannot be measured and is reconstructed from the cylinder pressure through a mass and energy balance over the cycle. The balance is only as good as its inputs. The valve events bound the closed and open phases and set the trapped mass. The polytropic exponents test whether the closed phases are adiabatic. The leakage and the backflow that cross the valves and the piston rings change the mass and the energy the balance carries. The cylinder pressure, the valve timing, the polytropic exponents, and the leakage are therefore established first as the foundation for the gas temperature and through it the heat flux.

The measured cylinder pressure is presented in two forms. The indicator diagram gives the pressure against the cylinder volume for all pressure ratios in shared axes, with the pressure normalised by the suction pressure (Fig. 6.11). The absolute cylinder, suction, and discharge

pressures over two revolutions at a representative load, with the cycle phases and valve events marked, are shown in Fig. 6.12.

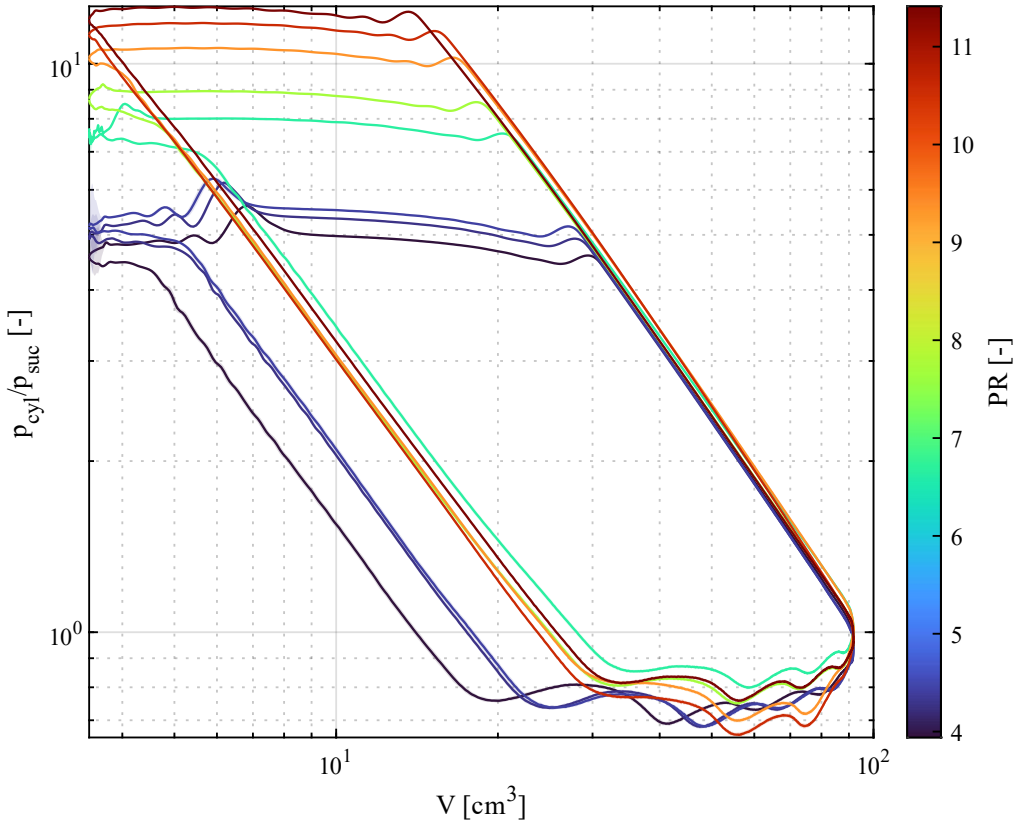

Figure 6.11 Indicator diagrams in log–log coordinates for all pressure ratios, p_{cyl}/p_{suc} versus V. Compression and re-expansion appear as straight lines. $\pm 1\sigma$ cycle band.

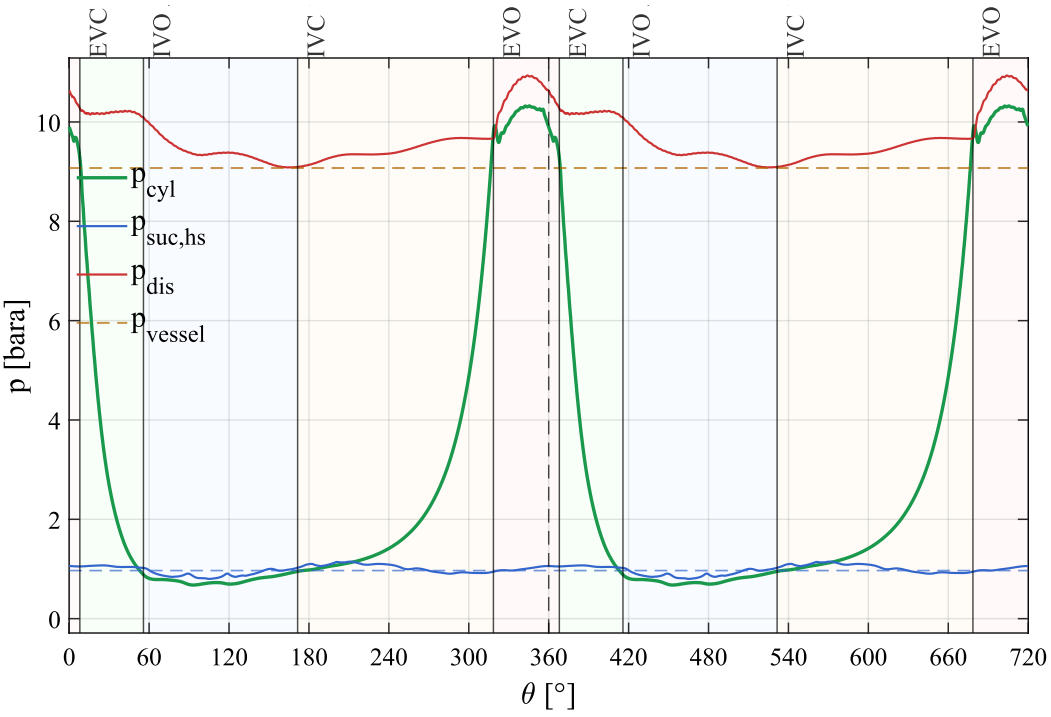

Figure 6.12 Cylinder, fast suction, discharge, and vessel pressures over two revolutions at a representative pressure ratio (PR ≈ 9.4), with the cycle phases shaded and the valve events IVO, IVC, EVO, and EVC marked.

At the lower pressure ratio, the cylinder pressure carries a small tooth in the middle of the discharge plateau, between the opening and the closing of the discharge valve, that is absent at the higher loads (Fig. 6.11). The feature is physical. The non-physical transducer spike near top dead centre has already been removed by the spike filter applied to the cylinder pressure, and what remains is a genuine fluctuation. The most likely cause is flutter of the discharge reed valve. The lift of the valve follows the discharge flow, which weakens as the piston slows towards top dead centre, so once the lift falls low enough the reed enters an underdamped regime and the cylinder pressure ripples. At a low pressure ratio, the margin between the cylinder pressure and the discharge pressure is small, the valve sits at a low lift through most of the discharge, and the flutter sets in already in the middle of the plateau. At a high pressure ratio, the cylinder pressure is well above the discharge pressure, the strong flow holds the valve open, and the plateau stays smooth. The discharge heat flux at the lower loads therefore carries a valve dynamic signature and is not quasi-steady discharge convection alone, a behaviour that the published correlations cannot represent.

The detected valve events are summarised as functions of the pressure ratio (Fig. 6.13). The closing of the discharge valve shifts with the load and shows the effect of valve sticking. The closing angle moves earlier with rising pressure ratio, from about 16 degrees after TDC at moderate loads to about 3 degrees at the highest loads. Less gas remains to be discharged, and the larger pressure difference reseats the valve faster. The zero-level correction of the cylinder pressure is reported for every run. Its systematic trend with the pressure ratio traces the drift of the transducer zero.

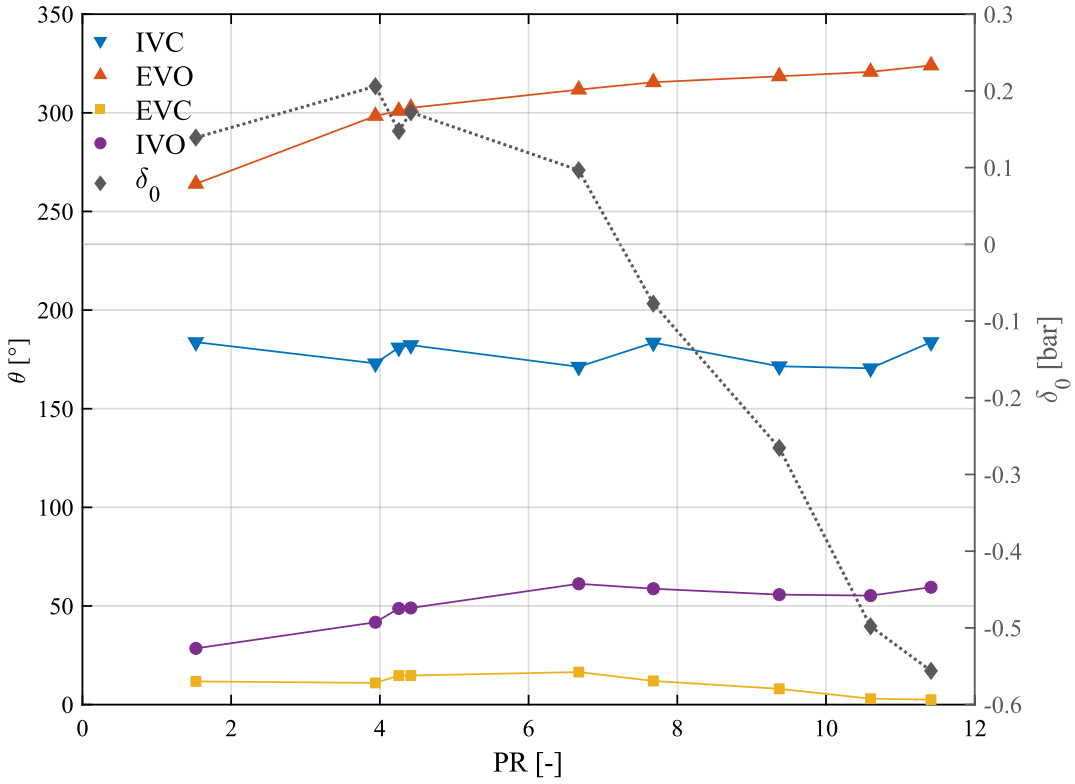

Figure 6.13 Valve event angles versus pressure ratio with uncertainty bars. Secondary axis with the zero-level correction for each run.

The in-cylinder polytropic exponent (Section 5.6) is evaluated from the log-log indicator diagram between IVC and EVO (Fig. 6.14). Its value lies between $n = 1.39$ and 1.42 and is nearly independent of the pressure ratio. The exponent of the re-expansion behaves differently. It falls from about 1.57 at the lowest load to about 1.07 at the highest load, which supports the valve leakage candidate quantified in Section 6.4. This contrasts with the apparent suction-to-discharge exponent of Section 6.1 and confirms that the trend observed there belongs to the overall process, not to the compression itself. The mass balance closes with the residual mass from the re-expansion. The residual mass fraction grows with the pressure ratio and links directly to the volumetric efficiency.

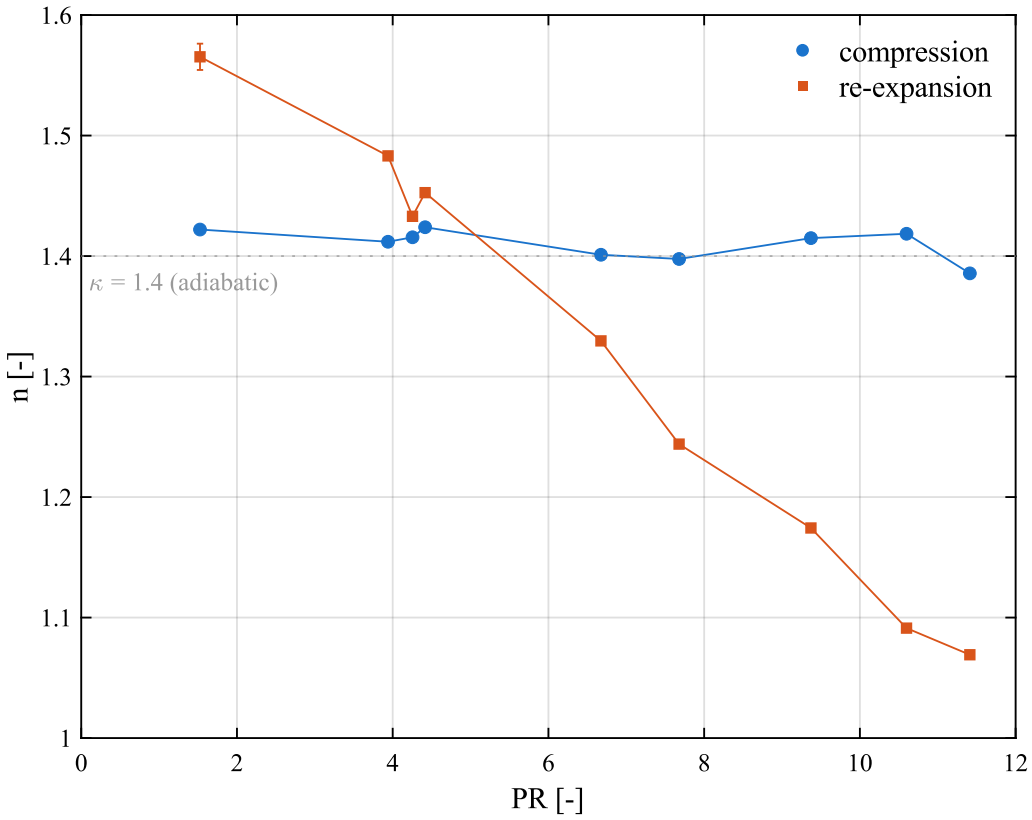

Figure 6.14 In-cylinder polytropic exponent versus pressure ratio.

6.4 Leakage and Backflow

Leakage matters here because it enters the mass balance behind the gas-temperature reconstruction, and a misjudged leak would be read as heat. The re-expansion of the clearance gas gives the most direct sign of leakage. A tight discharge valve would make this re-expansion almost adiabatic, with an exponent near 1.4. The measured exponent, introduced in Section 6.3, instead falls from about 1.57 at the lowest load to about 1.07 at the highest. The re-expansion is thus sub-adiabatic, so gas from the discharge side flows back into the cylinder through the discharge valve.

Figure 6.15 collects the leak paths as a fraction of the trapped charge. The backflow into the cylinder through the discharge valve grows from about 0.7 % at the lowest load to about 8.5 % at the highest. The blow-by past the piston rings, an upper bound from the annular-gap model [24], [40], grows from about 0.3 to about 2.1 %. The compression energy residual is negative at high load, an independent sign of outward leakage during compression (Section 6.8). The outflow through the suction valve during compression follows the same rising trend. The gas thus leaks outward through the rings and the suction valve during compression and discharge and flows back through the discharge valve during re-expansion. The inward backflow reaches about 8.5 % at the highest load, while the ring blow-by stays much smaller, near 2 %.

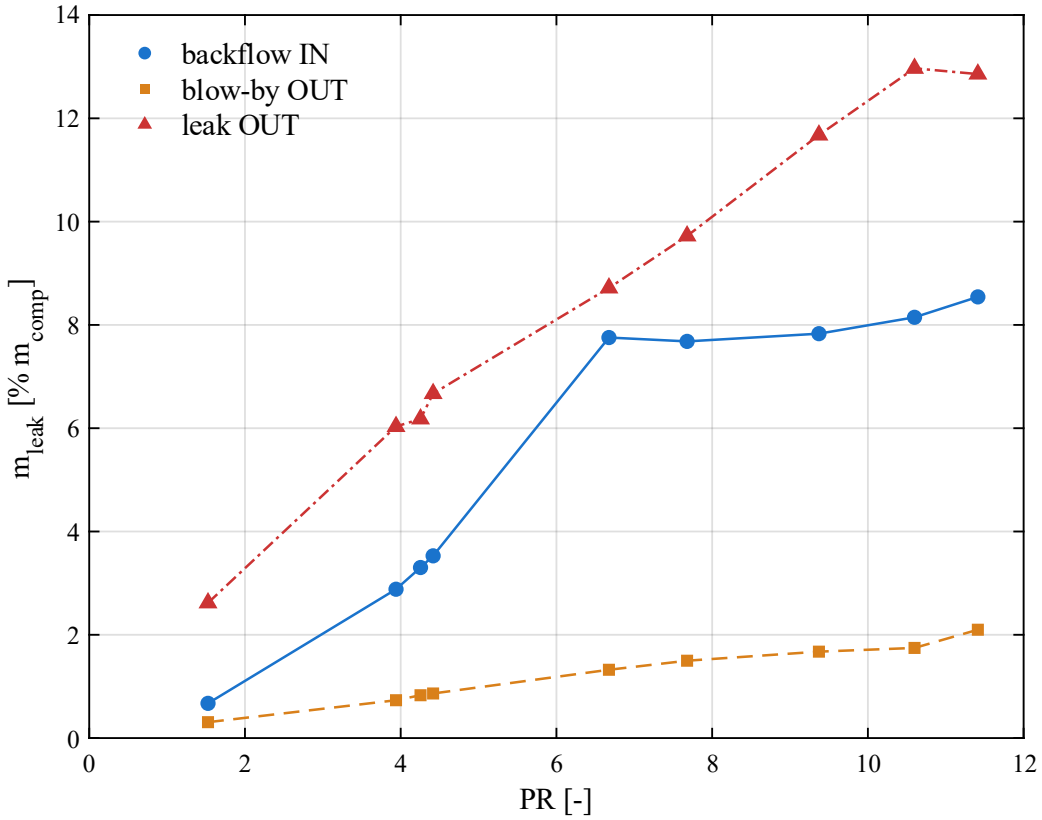

Figure 6.15 Leak mass as a percentage of the trapped charge against pressure ratio. The curves show the backflow into the cylinder through the discharge valve, the blow-by past the piston rings as an upper bound, and the leakage out through the suction valve, the last scaled by the leak fraction calibrated on the discharge valve.

The estimates rest on a careful treatment of the transducer offsets. The three pressures cannot be compared by their absolute values because each transducer carries its own offset. The offset is removed on the open-valve plateaus, where the cylinder and the line pressures must equalise. Figure 6.16 shows the three pressures over one cycle. On the discharge plateau the discharge pressure reads higher than the cylinder pressure, which is the opposite of a real outflow and so marks the offset. The correction brings the discharge trace onto the cylinder trace while the valve is open. One run shows an anomalous offset near −3.6 bar, consistent with its known pressure drift.

The backflow is estimated three ways, as set out in Section 5.6. The energy residual gives the returning mass. The pressure difference across the closed valve gives a second estimate, scaled to the energy residual. The volume overshoot of the re-expansion gives a third. Figure 6.17 compares them. They agree up to a pressure ratio of about seven, which supports the estimate. Above that they spread, with the orifice estimate climbing faster and the overshoot estimate scattering, while the energy estimate levels off near 8 %. The energy residual is therefore taken as the most robust measure.

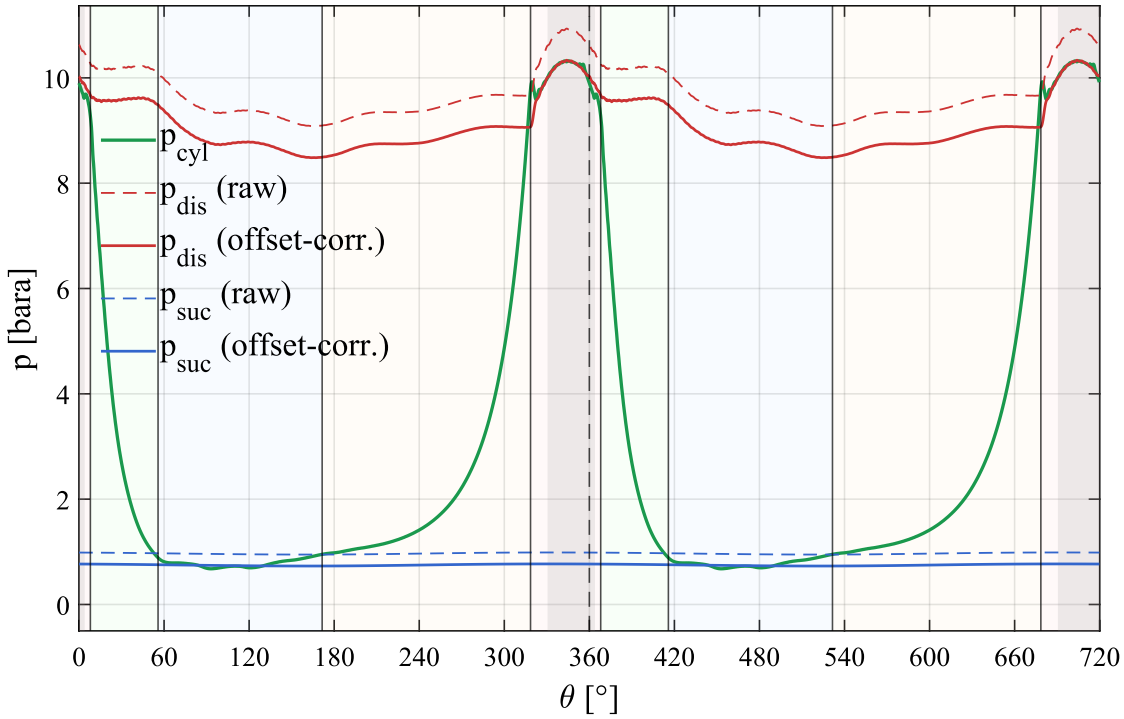

Figure 6.16 Cylinder, discharge and suction pressures over one cycle at a high load, raw and offset-corrected. On the discharge plateau (in grey) the discharge pressure reads about 0.6 bar above the cylinder pressure, which fixes the offset.

The leakage feeds back into the cycle reconstruction. The mass balance does not close without it, so the reconstruction reads part of the lost mass as heat. Part of the apparent in-cylinder superheating above a pressure ratio of about seven is blow-by counted as heating rather than a real temperature rise (Section 6.5). The polytropic index carries the same ambiguity. It absorbs the gas-to-wall heat transfer and the leakage in the same way, so a single exponent cannot separate the two [23].

The size of the leakage is in line with the literature. Loss breakdowns for small compressors place leakage at a few % of the thermodynamic losses [2]. The present measurements show it rising with load (Section 6.4), in line with the leakage models of Lohn [39] and Braga [38]. The ring blow-by here is an upper bound because it uses the full piston-cylinder clearance and scales with the cube of that gap. The real ring leakage is likely smaller, which leaves the discharge-valve backflow as the leading inward path at high load.

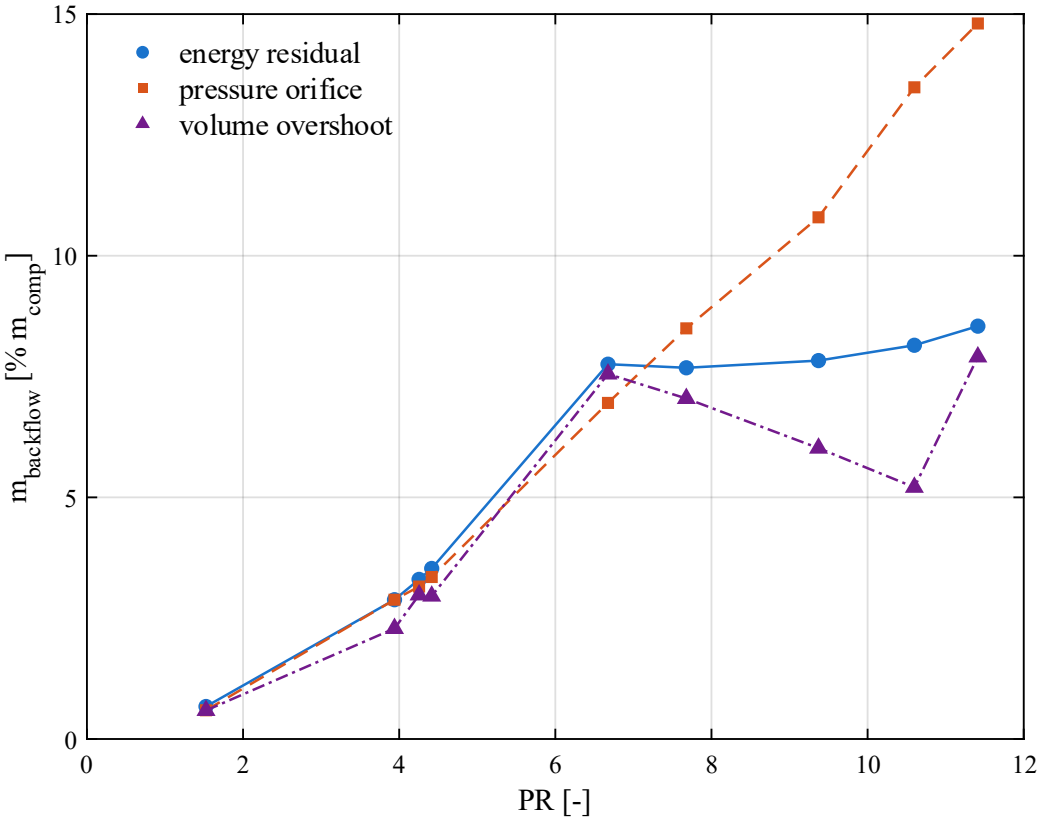

Figure 6.17 Backflow into the cylinder against pressure ratio from three estimates, the energy residual, the pressure-driven orifice scaled to it, and the volume overshoot of the re-expansion.

The clearance-flow model used here is the same formulation that Tuhovčák [24] applied to this compressor. The corrected blow-by stays below about two percent of the trapped charge at the highest load, in line with the piston-leakage loss of roughly one percent reported for small compressors [22]. The correction also reorders the outward paths. During compression the suction valve carries more outward flow than the rings, on the assumption that it leaks at the same fractional area as the discharge valve. At the highest load the negative compression energy residual is of the same size as these two outward paths together.

6.5 In-Cylinder Superheating

The temperature at the closing of the suction valve exceeds the suction chamber temperature by 35 to 85 K (Fig. 6.18). This in-cylinder superheating is a separate quantitative result. It extends the superheating chain measured by Morriesen [3] from the suction path into the cylinder.

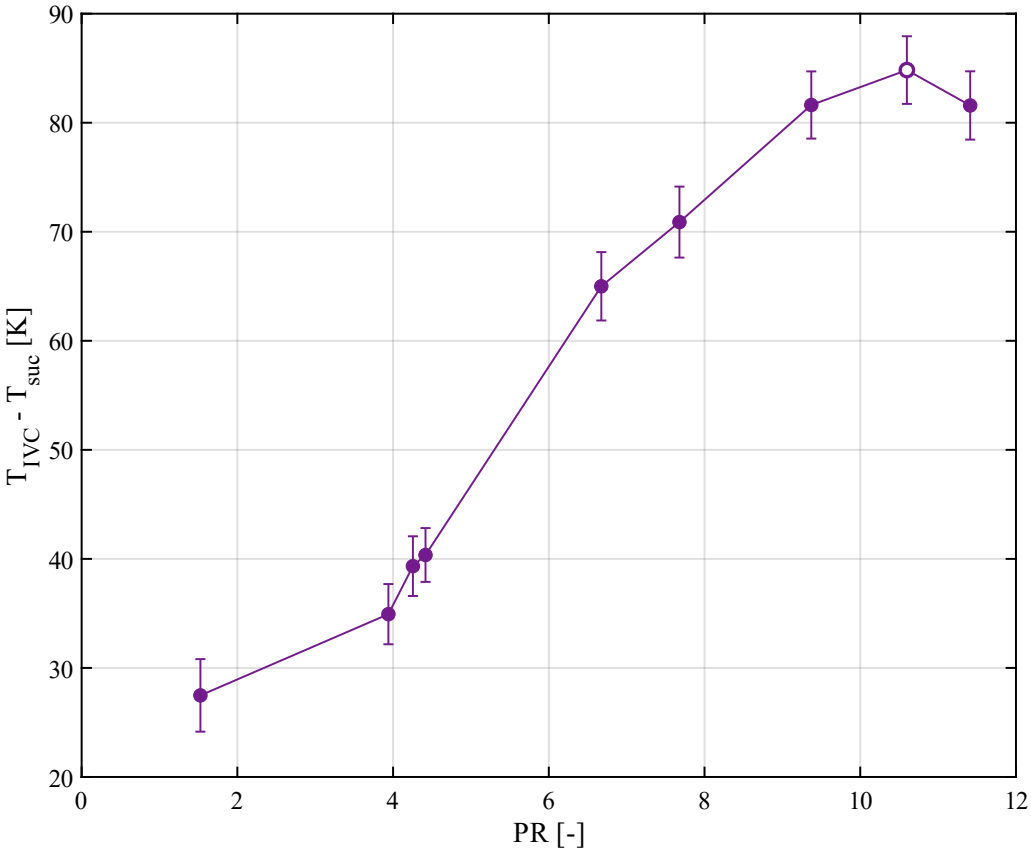

Figure 6.18 In-cylinder superheating $T_{IVC} - T_{suc}$ versus pressure ratio with error bars. The open symbol marks the point at PR ≈ 10.6, whose operating state had not fully settled.

The reconstructed gas temperature is shown for all pressure ratios in one overlay in the dimensionless form Θ. Two reference points fix the scale. Θ is zero at the suction temperature and one at the gas temperature when the discharge valve opens, so the very different absolute temperatures of the individual loads collapse onto a common axis and can be compared on one plot. The dimensionless overlay separates two families (Fig. 6.19). At low pressure ratios the charge falls to $\Theta \approx 0.05$ during suction. At high pressure ratios it falls only to $\Theta \approx 0.15$, so the relative superheating of the charge grows with the load. The spread between the two reconstruction schemes of Section 5.7 is shown as a band. The band is widest during suction, where the dimensionless spread reaches 0.15 to 0.2, and narrow during the closed phases. The uncertainty of the reconstruction is therefore concentrated exactly where the mixing acts. At the opening of the suction valve the reconstructed gas temperature does not return to the suction temperature. It stays above it by 40 to 43 K at the low pressure ratios and by 96 to 150 K above PR ≈ 6.7. At that instant the cylinder still holds the re-expanded clearance gas, so the fresh charge enters an already superheated volume. In dimensionless form, Θ at suction-valve opening lies between 0.16 and 0.32 and follows the same threshold between PR 4.4 and 6.7 as the other stratification indicators of Section 6.9.

The size of this in-cylinder superheating places it within a long-standing efficiency concern. Suction superheating carries a loss of a few percent of the compressor efficiency [22], [23],

[91]. Component-resolved heat flux measurements in a small hermetic compressor locate the gas heat-up both along the suction system and inside the compression chamber, with the suction-muffler surface carrying a heat flux of the same order as the electrical motor [68]. The 35 to 85 K measured here extends that chain to the wall of the cylinder itself and gives the in-cylinder share directly, rather than as the residual of a suction-line balance.

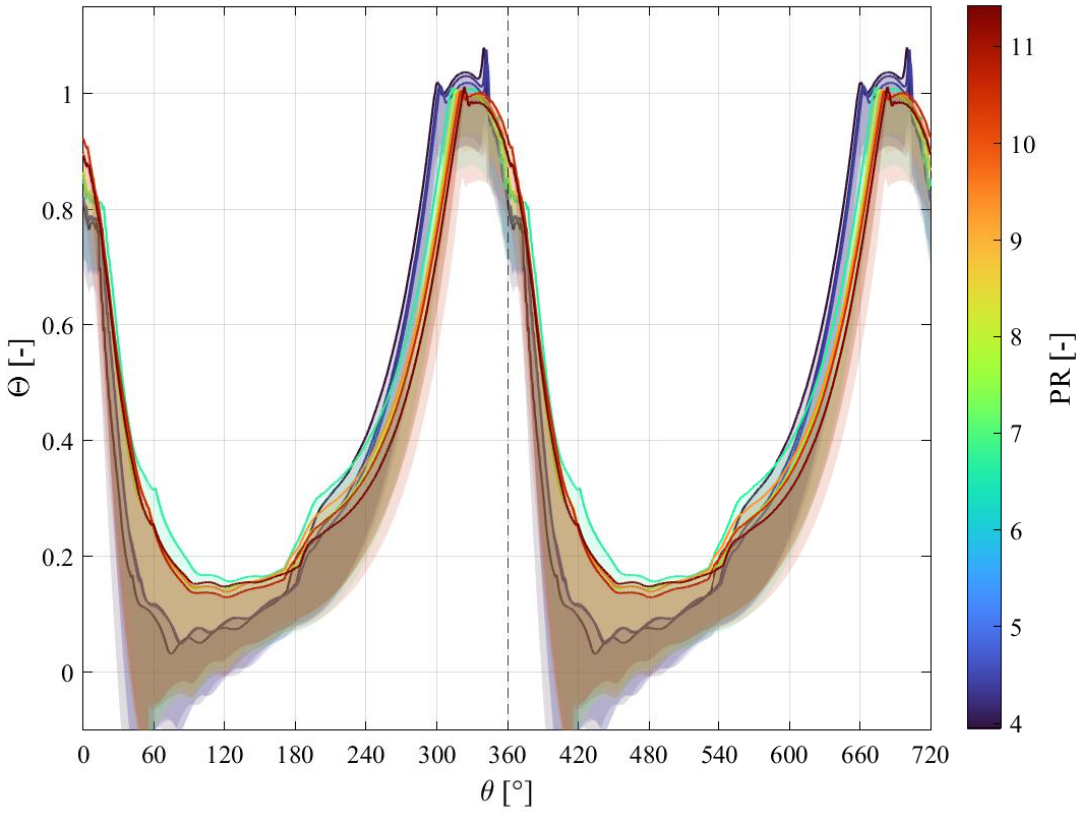

Figure 6.19 Dimensionless gas temperature Θ versus crank angle for all pressure ratios. Θ is scaled to zero at the suction temperature and one at the gas temperature when the discharge valve opens, so the different loads share one axis. The curves stay above zero during suction, which is the in-cylinder superheating. Scheme spread as shaded band.

Not all of the high-load rise is wall heating. The re-expansion exponent falls toward 1.1 at the two highest loads and the mass balance does not close without leakage (Sections 5.6 and 6.4), so part of the apparent superheating above PR 6.7 is blow-by read as heat, as quantified below. This distinction is invisible to the integral models that the field relies on. The polytropic index absorbs the combined effect of the heat transfer between the gas and the wall and the leakage in the same way, so a single exponent cannot separate wall heating from a leaking valve [23]. The instantaneous reconstruction separates them, because the closed-phase flux and the open-phase mass balance are measured independently.

The model assumptions of Section 5.7 are assessed next. The piston face is not instrumented, and the energy balance treats it as adiabatic. Near TDC the piston forms about half of the exposed area, so this is the largest single systematic of the reconstruction. A sensitivity run that assigns the piston the valve plate flux as an upper bound and the lower liner flux as a lower

bound brackets the reconstructed gas temperature (Fig. 6.20). This interval is not small and grows with the load, from about ±5 K on the suction-valve-closing temperature and ±8 K on the discharge temperature at the lowest pressure ratios to about ±18 K and ±34 K at the highest. The unmeasured piston flux is therefore an important systematic of the reconstructed high-load temperatures, because the piston enters the open-phase energy balance and sets the trapped mass that scales the whole reconstructed temperature.

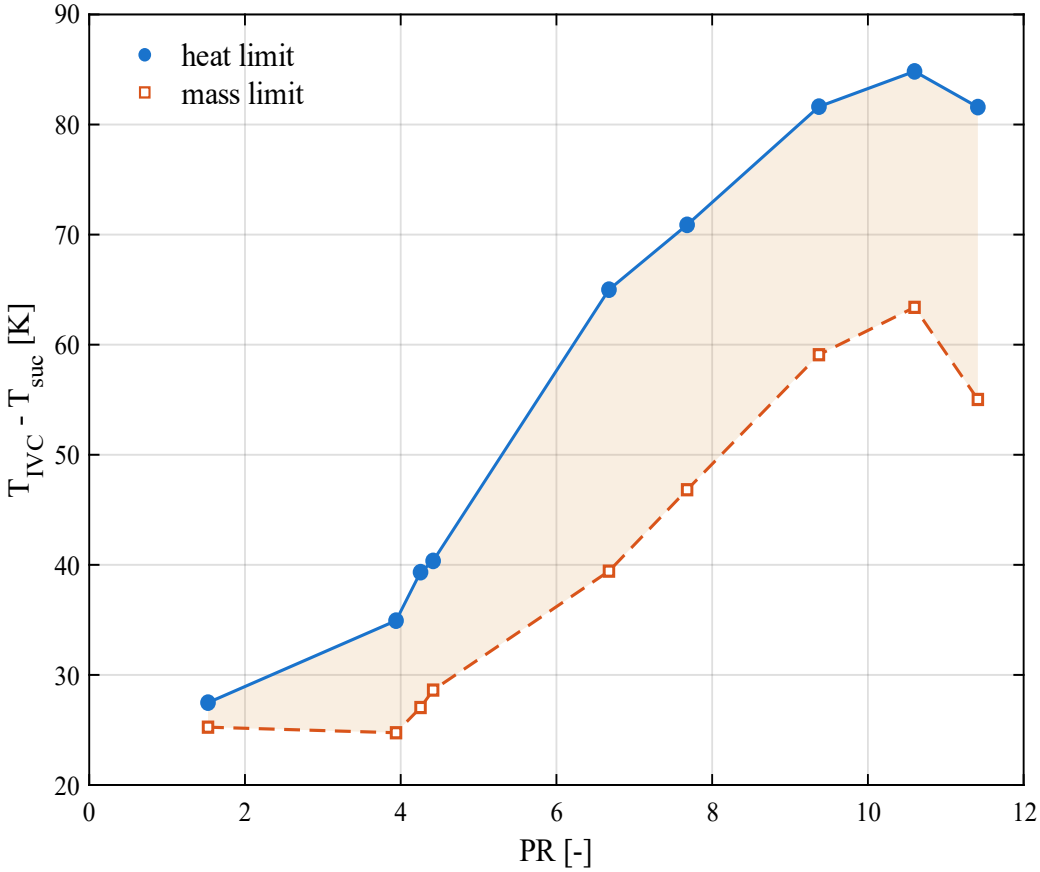

Figure 6.20 In-cylinder superheating $T_{IVC} - T_{suc}$ versus pressure ratio, shown as the sensitivity of the reconstruction to the reading of the closed-phase energy residual. The heat limit is the reconstruction used throughout this chapter, which carries the residual as a temperature rise. The mass limit assigns the same residual to the discharge-valve backflow as trapped mass. The true value lies within the shaded band, which widens with load as the leak grows.

Leakage is not part of the closed-phase model. The cycle closure then converts any blow-by into an apparent heating of the charge, so a part of the reconstructed in-cylinder superheating may be an artefact of this kind. An independent estimate places the discharge-valve blow-by between 0.7 % of the trapped mass at the lowest load and 8.5 % at the highest, rising monotonically with the load. This magnitude matches the 9 % mismatch between the CF and the flow-meter mass balances, so a comparable fraction of the apparent high-load superheating is due to leakage rather than to wall heating. At the two highest loads the effective exponent of the re-expansion falls to 1.06 to 1.16, which is consistent with a small leak at the discharge valve at a pressure difference around 10 bar. The clearance volume changes by about 14 % per 5 degrees

of crank angle near TDC, so the reconstruction keeps its documented sensitivity to the closing angle of the discharge valve. The uncertainty of the cylinder pressure has to be referred to the pressure at the suction valve closing, not to the transducer full scale, because the trapped mass is anchored there.

The closed-phase energy residual that drives the high-load superheating can be read two ways, and the two readings bound the result. The reconstruction of this chapter keeps the trapped mass fixed in the closed phases and lets the residual raise the gas temperature, so the residual is carried as heat. The largest unmeasured heat source is the piston face, whose flux is not instrumented and which forms about half the exposed area near top dead centre, giving the ±18 to ±34 K bracket noted above. The opposite reading assigns the same residual to the discharge-valve backflow as trapped mass. Re-running the full reconstruction in this mass limit lowers the apparent in-cylinder superheating by up to about 22 K at the highest loads (Fig. 6.20) and the reconstructed peak gas temperature by up to about 45 K, while the low-load values barely move. The same limit raises the fitted heat-transfer constants by under ten percent and the measured Nusselt number by up to about a quarter. It leaves the ranking of the five correlations, the common residual floor, the complex-Nusselt phase of Section 6.9, and the three efficiencies of Fig. 6.21 unchanged, and the correlation fit is no worse. Because the unmeasured piston flux and the valve backflow act on the same residual, the present instrumentation cannot separate them, and the true reconstruction lies between the two limits. The heat-transfer conclusions of this chapter therefore hold across the whole interval. The leak, or the equivalent unmeasured heat, shifts the absolute level of the coefficient by at most a tenth and changes none of the qualitative findings.

6.6 Compressor Performance

The performance map (Fig. 6.21) places the heat-transfer results in their thermodynamic context. The three efficiencies follow distinct trends with load and cross near a pressure ratio of seven. The volumetric efficiency falls from about 80 % at the lightest load to about 55 % at the heaviest, a decline of 25 %. The isentropic efficiency holds near 60 % across the working loads. The electromechanical efficiency rises the other way, from about 50 % at the lower working loads to about 65 % at the highest, because the motor and friction losses are largely fixed and take a smaller share of the indicated power as the load grows. The lightest run is excluded from the correlation analysis because its fitted constants collapse to zero, and at that point the isentropic and electromechanical efficiencies fall toward 33 %, the indicated power being small against the fixed losses. The two highest loads carry a documented inconsistency in the flow scaling and are flagged accordingly, and the electrical input at two moderate loads is an estimate from a fit rather than a direct reading.

The fall of the volumetric efficiency with pressure ratio follows the behaviour established for this class of machine. A detailed decomposition attributes it to three coupled mechanisms [22]. The first is the re-expansion of the gas trapped in the clearance volume, which grows with the

pressure ratio and becomes the dominant term at high load. The second is the reduced suction-gas density that follows from the in-cylinder and suction-path superheating. The third is the loss of trapped charge through valve backflow and piston-ring blow-by. The measured values match the range reported for a comparable small reciprocating compressor, in which the volumetric efficiency falls from 73.7 % at a pressure ratio of 2.6 to 60.3 % at 12.9 [22], [24].

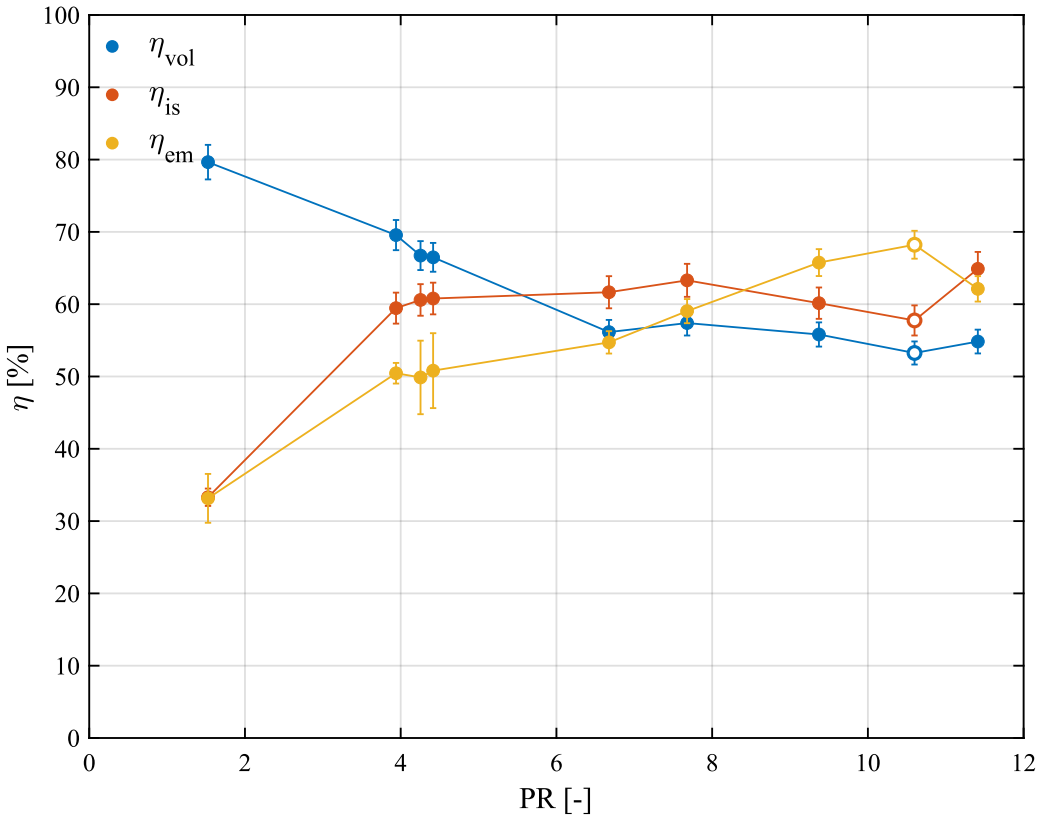

Figure 6.21 Volumetric, isentropic and electromechanical efficiency versus pressure ratio

The isentropic efficiency of about 60 % sits below the 80 to 83 % quoted for optimised hermetic refrigeration compressors [2], [22]. The difference is one of machine class rather than of measurement. The test compressor is an open, air-cooled machine in which a few percent of blow-by past the piston rings is tolerated, whereas the sealed refrigeration machines that set the higher benchmark admit no leakage and run with correspondingly tighter clearances and valves. The value reported here is also referred to the delivered mass and spans pressure ratios up to eleven, so it carries the full penalty of the re-expansion and leakage losses that an indicated compression efficiency would omit. Taken together, the two thermodynamic efficiencies confirm that the dominant degradation in this machine is thermal and leakage-related, the two processes that the instantaneous measurement was designed to separate (Sections 6.4 and 6.5).

6.7 Suction Flow and Valve Dynamics

The suction flow measured by the fast thermal flow sensor provides the timing reference of the

cycle and an independent picture of the valve dynamics (Fig. 6.22). The shape of the flow signal is reliable. The absolute scale is anchored to the reference flow meter because the sensor saturates and underestimates the absolute level.

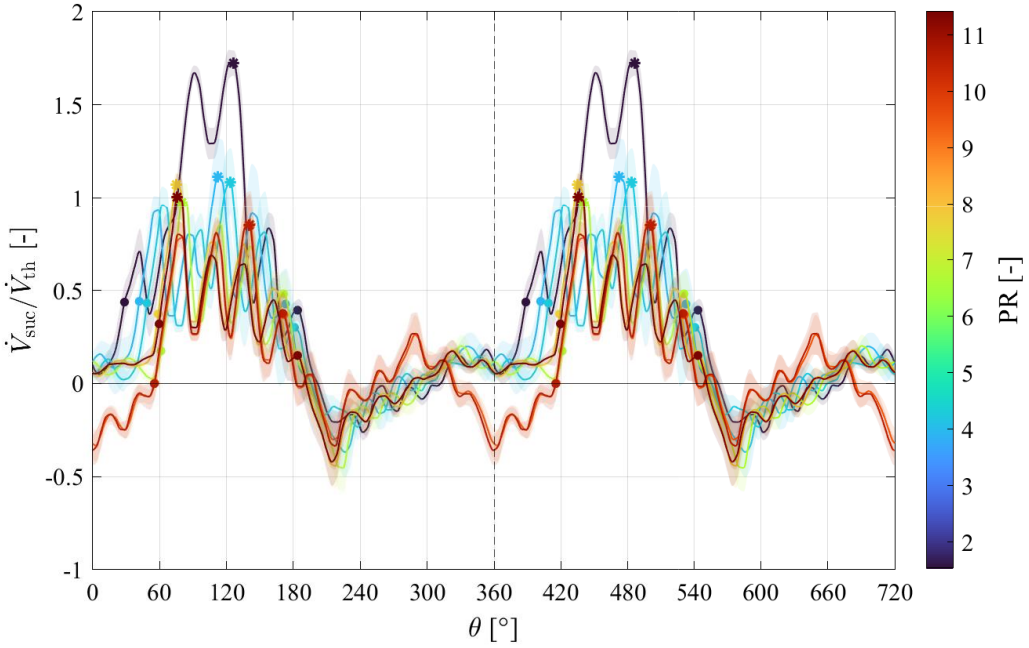

Figure 6.22 Phase-averaged suction flow for all pressure ratios, normalised by the displaced volume flow. $\pm 1\sigma$ cycle band. IVO, flow peak and IVC marked.

A spectral analysis of the suction flow (Section 5.5) shows that it oscillates at the running-speed orders, integer multiples of the rotational frequency of about 24 Hz, rather than at a free acoustic frequency. Its spectrum coincides with that of the fast suction pressure (Fig. 6.23), so only the pressure is shown. The measured peaks fall on integer orders to within 1 %. The energy is carried by the first order, the once-a-revolution suction pulse, and by the second order near 48 Hz. The overall amplitude falls with the pressure ratio as the volumetric efficiency drops and the suction pulse weakens. The second order, by contrast, gains in relative weight and overtakes the first at the two high loads PR 9.4 and 10.6, where the dominant frequency steps from 24 to 48 Hz. The highest load returns to first-order dominance, consistent with the documented anomaly of that operating point.

The second order lies near the quarter-wave band of the suction line. Its closed-valve-to-vessel length of about two metres places the fundamental in the forties of hertz. The running-speed order nearest this resonance is therefore amplified, and the suction unsteadiness becomes acoustically resonant at high load. This is confirmed by the fast suction pressure, which sits at the pressure antinode of the quarter-wave near the valve, while the flow sensor sits at the velocity node. At PR 9.4 and 10.6 the pressure carries the second order about 1.8 times more strongly than the flow, with a second-to-first-order ratio near 2.0 against 1.1. A purely kinematic second harmonic of the induction pulse would instead appear equally in both. This stronger response in the pressure is the signature of a standing acoustic wave (Fig. 1.10). Since the quarter-wave fundamental coincides with the second running-speed order, the mode shape identifies the resonance, not the frequency.

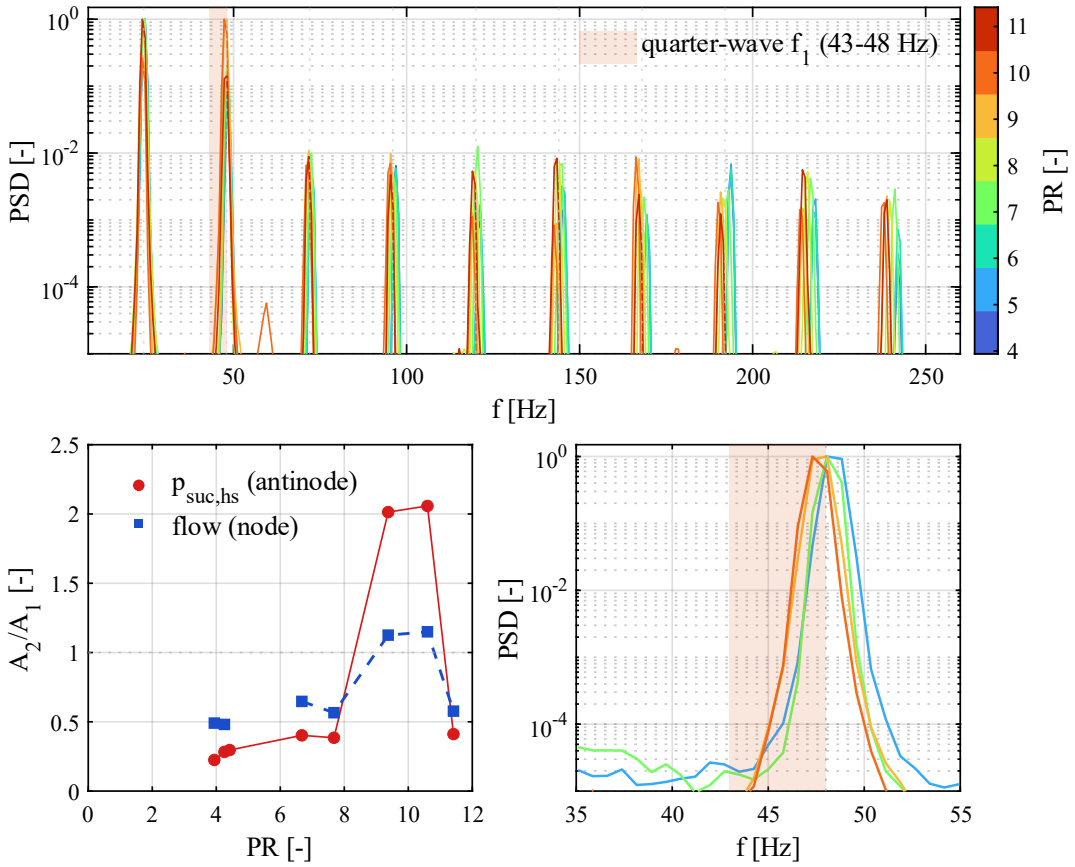

Figure 6.23 Fast suction pressure (Kulite, 100 kHz). (a) Power spectra for all pressure ratios; (b) second-order mode-shape test versus pressure ratio, comparing the pressure antinode at the valve with the velocity node at the flow sensor; (c) zoom on the quarter-wave band near 48 Hz.

This behaviour is the textbook picture of compressor gas pulsations. Soedel [34] describes the slider-crank mechanism as a source with an infinite set of harmonics of the rotational frequency that fall in amplitude with the harmonic number, which is the running-speed-order spectrum seen here. He treats the gas in the suction and discharge lines with one-dimensional acoustic wave theory and notes that high amplitudes arise whenever a natural frequency of the line coincides with an excitation frequency, a coincidence that designers normally detune away. Manifold gas-column models reproduce the same effect, predicting that the dominant pulsation harmonic follows whichever acoustic mode of the line lies closest to a running-speed order, so the response can jump from one harmonic to another as that alignment shifts [29]. This suction line is not detuned, since its quarter-wave fundamental sits on the second running-speed order at the two highest loads. The mode-shape test used above rests on the same acoustic structure that Soedel sets out, in which a standing mode carries its pressure maximum where the velocity passes through zero, which is why the pressure sensor at the antinode and the flow sensor at the node see the second order with such different strength. The temperature side of the same waves appears in the cold-wire records of Morriesen [3], whose suction-chamber temperature oscillated in step with the pressure pulsations rather than with any slow exchange at the wall.

The resonance appears only at the two highest loads. At lower pressure ratios the suction oscillation stays a first-order induction pulse. The delayed reattachment of the suction valve near

340° generates oscillations that persist through the discharge. A self-acting suction reed can bounce and oscillate several times before it finally closes, so part of the oscillation after nominal closing reflects the valve's own dynamics rather than the prescribed motion assumed in the model [30].

Disconzi [9] report the opposite distribution of the unsteadiness. Their CFD shows oscillations of the flow and of the heat flux during the discharge, caused by intermittent recirculation in the valve passage, and a stable suction valve that remains on the seat until it closes. The data here show strong suction-side oscillations on a real self-acting valve. The difference points to the valve dynamics and to the suction line acoustics, which a simulation with a stable valve cannot reproduce. A fluid-structure interaction model that allows the valve plate to move couples the valve motion to the suction-side pressure pulsation, capturing the interaction that a fixed-valve calculation omits [37].

6.8 Surface Temperature and Heat Flux

The phase-averaged surface temperature swings are presented for each surface and pressure ratio with the cycle mean removed, which allows a direct overlay (Fig. 6.24). The amplitudes fall within the range of 0.5 to 2 K reported by the experimental studies reviewed in Chapter 2 [9], [13].

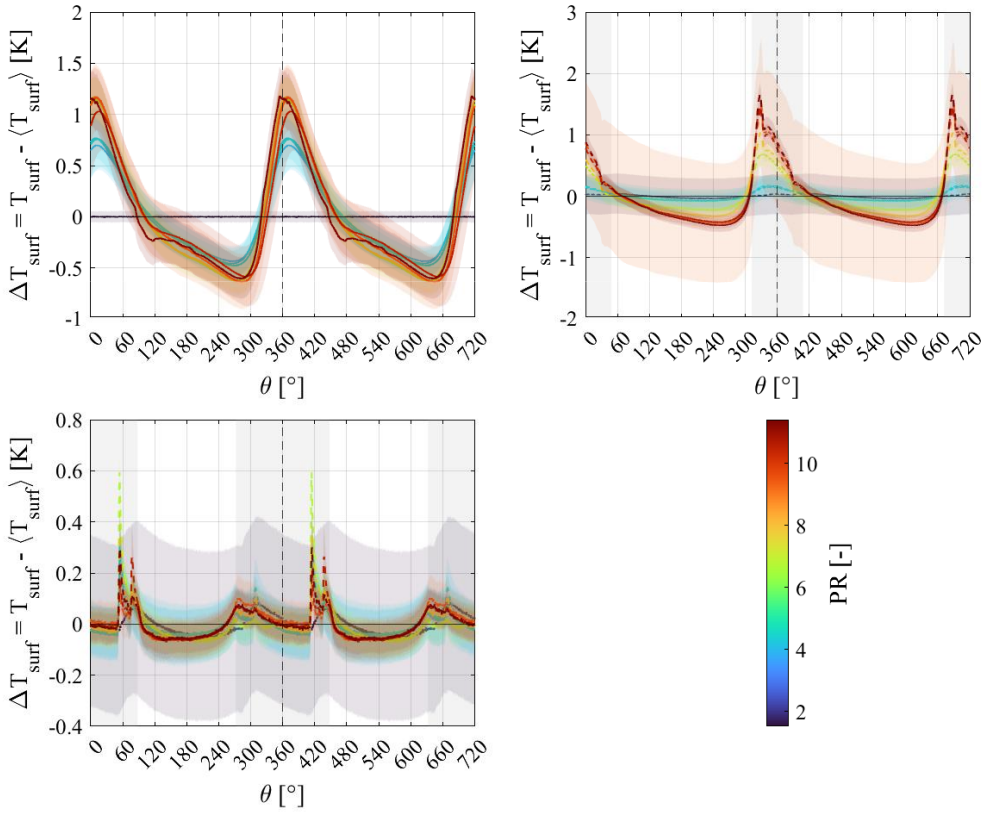

Figure 6.24 Surface temperature swing for each surface, cycle mean removed, ±1σ cycle band. (a) valve plate, (b) upper cylinder thermocouple, (c) middle cylinder thermocouple. Shaded regions mark crank angles where the thermocouple is covered by the piston.

The valve plate swing grows with the load and saturates near 1.8 K above PR ≈ 7, because the mean plate temperature rises together with the heat flux. The swing at the upper liner sensor rises sharply once the discharge pressure peaks reach its axial position. The full-cycle records of the liner sensors also contain the passage of the piston rings, which produces a contact artefact unrelated to the gas. Only the exposed part of the cycle is therefore evaluated and plotted.

The instantaneous heat flux changes direction at least twice in each revolution at every surface. The discharge phase carries the positive peak. The suction phase carries a sustained negative flux (Fig. 6.25). The CF and Reichelt evaluations agree within 2.5 to 4.2 % at the valve plate. At the liner sensors the difference reaches 23 %, because the contact spikes of the piston passage raise the share of high harmonics, where the two formulations differ most. The agreement at the valve plate confirms the semi-infinite treatment under operating conditions.

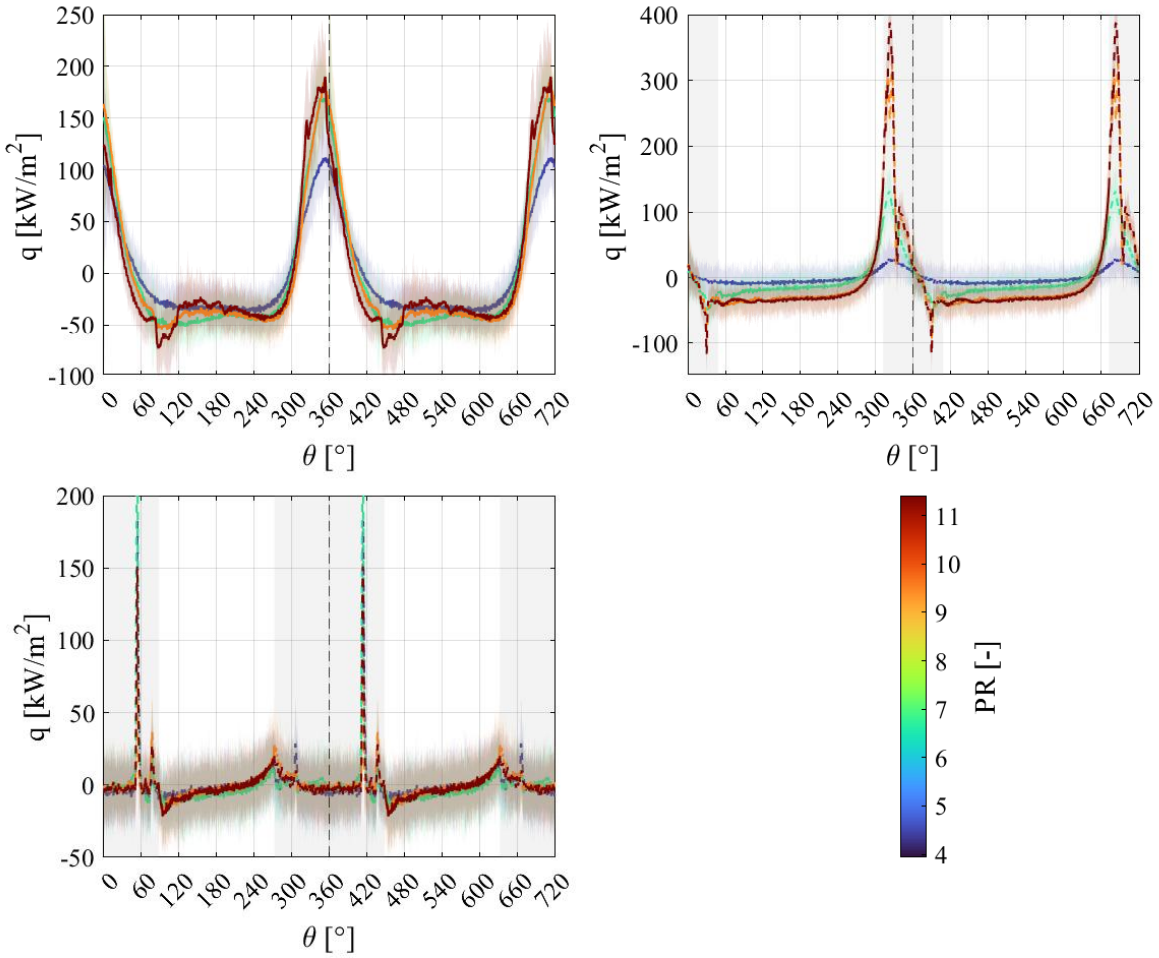

Figure 6.25 Instantaneous heat flux for each surface for selected pressure ratios over two revolutions, shared scale for each surface; ±1σ cycle band. (a) valve plate, (b) upper cylinder thermocouple, (c) middle cylinder thermocouple. Grey bands mark crank angles where the thermocouple is covered by the piston.

The energy residual of the closed phases (Section 5.6) is reported for each run. During compression it remains between −1 and −21 % of the phase work and grows with the pressure ratio, which is consistent with leakage (Section 6.4). During expansion it reaches +43 to +51 % at all loads and indicates an inflow of mass or heat through the closing discharge valve, discussed in Section 6.3.

The cycle-averaged flux is compared with the external heat flux sensor, which anchors the overall energy balance (Fig. 6.26). The inner surfaces show negative means while the external sensor shows positive values that grow with the load. The liner thus receives heat by conduction from the head end and releases it both inward into the charge and outward to the surroundings.

The shaded bands in the cycle-resolved figures show the variability of a single cycle. Its standard deviation is 20 to 23 kW/m² and is practically constant across runs, surfaces, and crank angles. The noise is therefore dominated by the white temperature noise amplified by the inversion, not by the flow variability. The standard error of the averaged curve is 1.3 to 1.5 kW/m² for the ensemble of roughly 240 cycles.

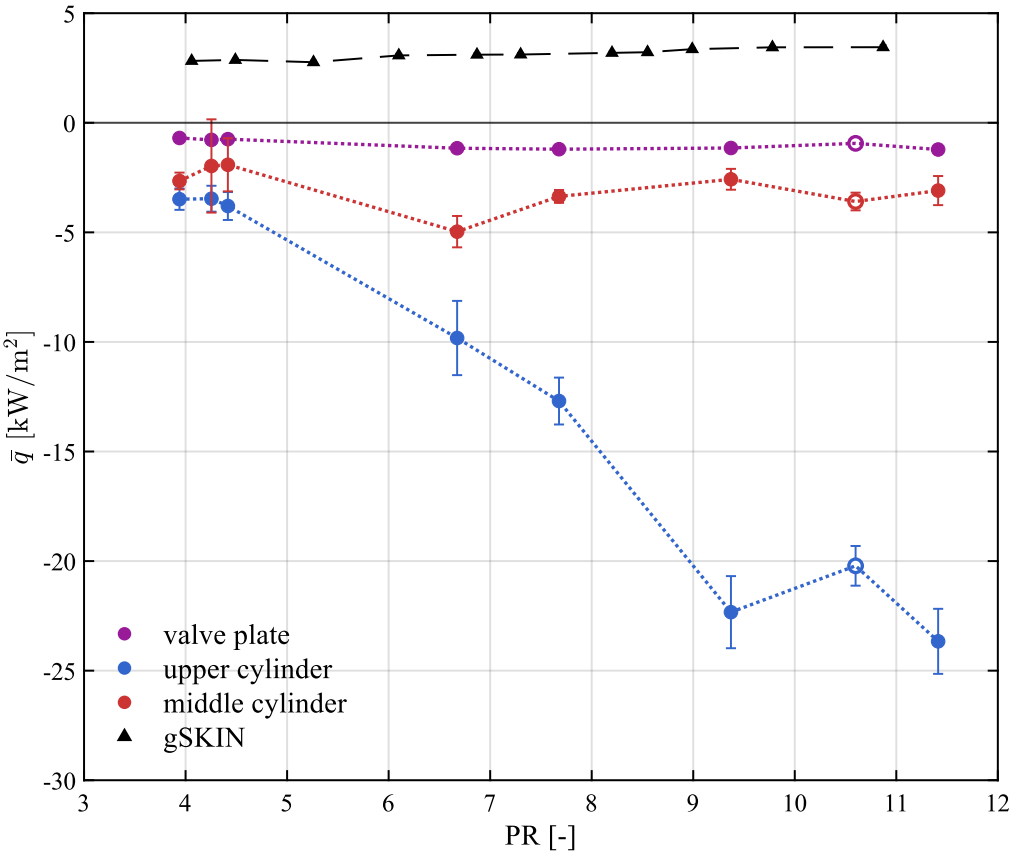

Figure 6.26 Cycle-averaged heat flux for each surface versus pressure ratio with error bars, together with a preliminary reading from the external gSKIN sensor.

The discharge-phase oscillations of the measured heat flux are weaker and of higher frequency than the recirculation-driven oscillations computed by Disconzi [9]. Their relation to the valve sticking and to the acoustics identified in Section 6.7 is discussed. The coaxial signals recorded in the pressure acquisition session show a systematic attenuation of about one half that is not yet explained. The parallel heat flux evaluation from that session is therefore retained only as a diagnostic.

6.9 Heat Transfer Coefficient on Selected Surfaces

The HTC is presented on three levels. The first level is the heat flux itself, which is fully measured and free of any singularity. The second level is a least-squares estimate of the quasi-static coefficient for each phase and surface. It avoids the division by the temperature difference, and the angles around the gas-to-wall temperature crossings are marked as invalid. The third level is a two-term model with an in-phase and a quadrature component. It absorbs the lag between the heat flux and the temperature difference and turns the crossings into a regular part of the fit. This two-term fit is a measured complex HTC, its in-phase and quadrature parts corresponding to the real and imaginary components of the complex Nusselt number [47]. The phase-averaged quasi-static coefficient works on the valve plate in three phases of four (Fig. 6.27). During suction it is 430 to 960 W/m²K, during discharge 400 to 630 W/m²K, and during expansion 440 to 730 W/m²K, all stable and positive. During compression the phase average falls between −170 and +210 W/m²K and is mostly negative, so the lag defeats the static description even as a phase average. At the liner positions the suction average changes sign between PR 4.4 and 6.7, from about +450 to −1400 W/m²K at the upper sensor and from about +400 to −280 W/m²K at the lower sensor. A negative phase average means that the bulk temperature difference has the opposite sign to the local driving difference.

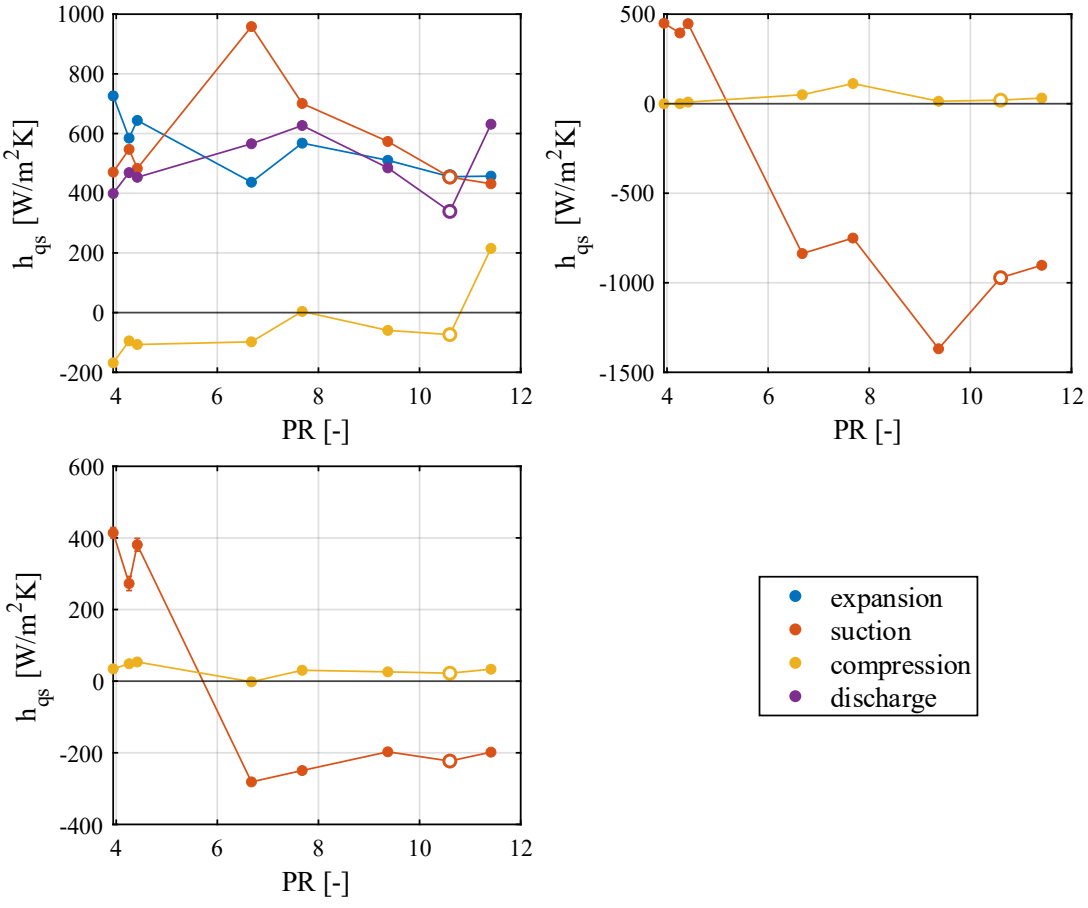

Figure 6.27 Quasi-static least-squares heat transfer coefficient for each phase versus pressure ratio, with error bars. (a) valve plate, (b) upper cylinder thermocouple, (c) middle cylinder thermocouple.

The quasi-static definition fails in a documented way. The measured flux at the temperature crossing of the compression phase is far from zero, about −43 kW/m² at the valve plate at PR 7.7, so the pointwise coefficient diverges and changes sign. This reproduces the observations of Overbye [41] and Lawton [14]. Engine wall heat transfer studies further show that the static form fails most strongly on expansion and that an unsteady term tied to the rate of compression and expansion is needed to recover the measured flux [44], [59]. An inversion of Newton's law shows the same failure from the opposite direction. In parts of the cycle no physical gas temperature reproduces the measured flux together with a quasi-static coefficient.

The two-term fit gives the magnitude and the phase of the coefficient for each surface and pressure ratio. The phase at the valve plate has the opposite sign to the gas-spring prediction of Kornhauser [47] (Fig. 6.28). The cold near-wall layer left by the suction jet is the proposed explanation. The two-term fit at the valve plate holds across the whole load range, with a magnitude of 296 to 521 W/m²K, a phase of −12 to −32 degrees, and a coefficient of determination of 0.65 to 0.83. The magnitude is 3 to 5 times the gas-spring level of Kornhauser, which is 95 to 117 W/m²K for the present oscillation Péclet numbers. The pointwise quasi-static coefficient is negative throughout the late compression, between about 260 and 320 degrees, so the static description fails over a quarter of the cycle and not only near the crossings.

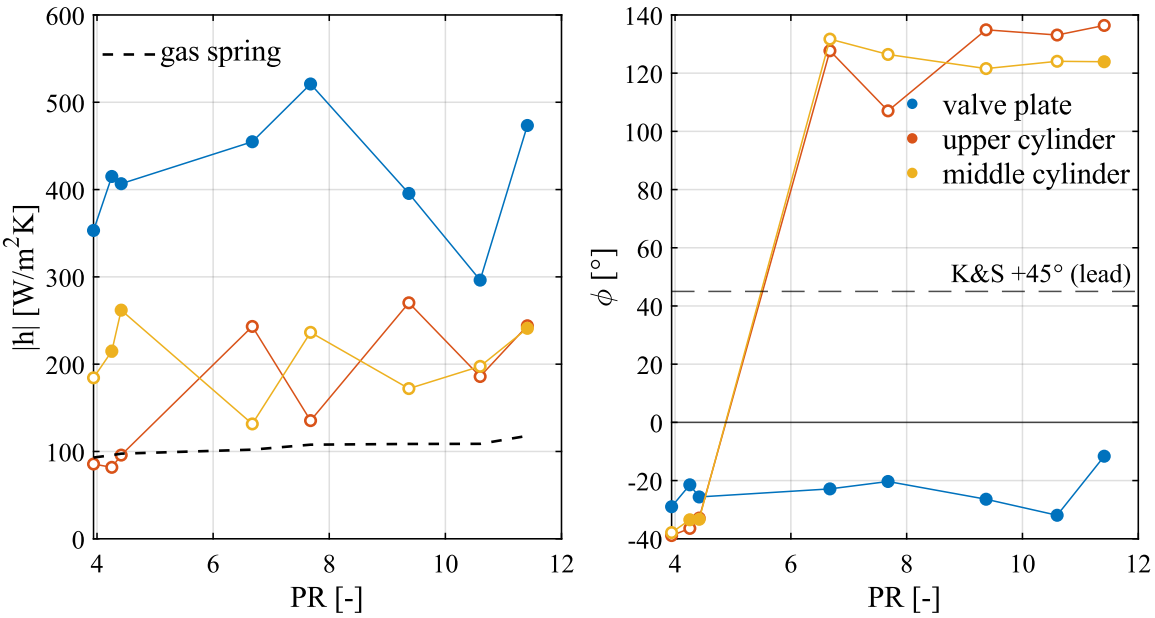

Figure 6.28 Magnitude and phase of the two-term heat transfer coefficient for each surface versus pressure ratio. (a) magnitude, (b) phase lag.

The phase of the heat flux is the clearest point of contact with the literature. Kornhauser [47] measured heat transfer in piston-cylinder gas springs and showed that the flux runs out of phase with the bulk temperature difference, leading it by up to 45 degrees at high oscillation Péclet number. Their complex Nusselt number (Equation 2.15) is the standard description of that lead. The valve plate here does the opposite, with the flux lagging the temperature difference by 12 to 32 degrees (Fig. 6.29). A phase offset of this kind is the classical signature of unsteady gas-side heat transfer, where the flux is not in simple proportion to the instantaneous temperature difference [92]. Carrying it in a correlation requires a quadrature term in the time derivative of

the gas temperature, which is the route taken when a derivative term is added to the quasi-static engine and compressor correlations [44], [58]. The gas spring is a closed adiabatic process, while the valve plate sees an open process dominated by the suction and discharge jets. In an engine, the flux led the temperature difference on expansion in the motored case, as in a gas spring, but lagged once combustion stirred the charge [93]. The lag measured here at the jet-swept valve plate belongs to that second regime, where advection rather than adiabatic compression sets the timing.

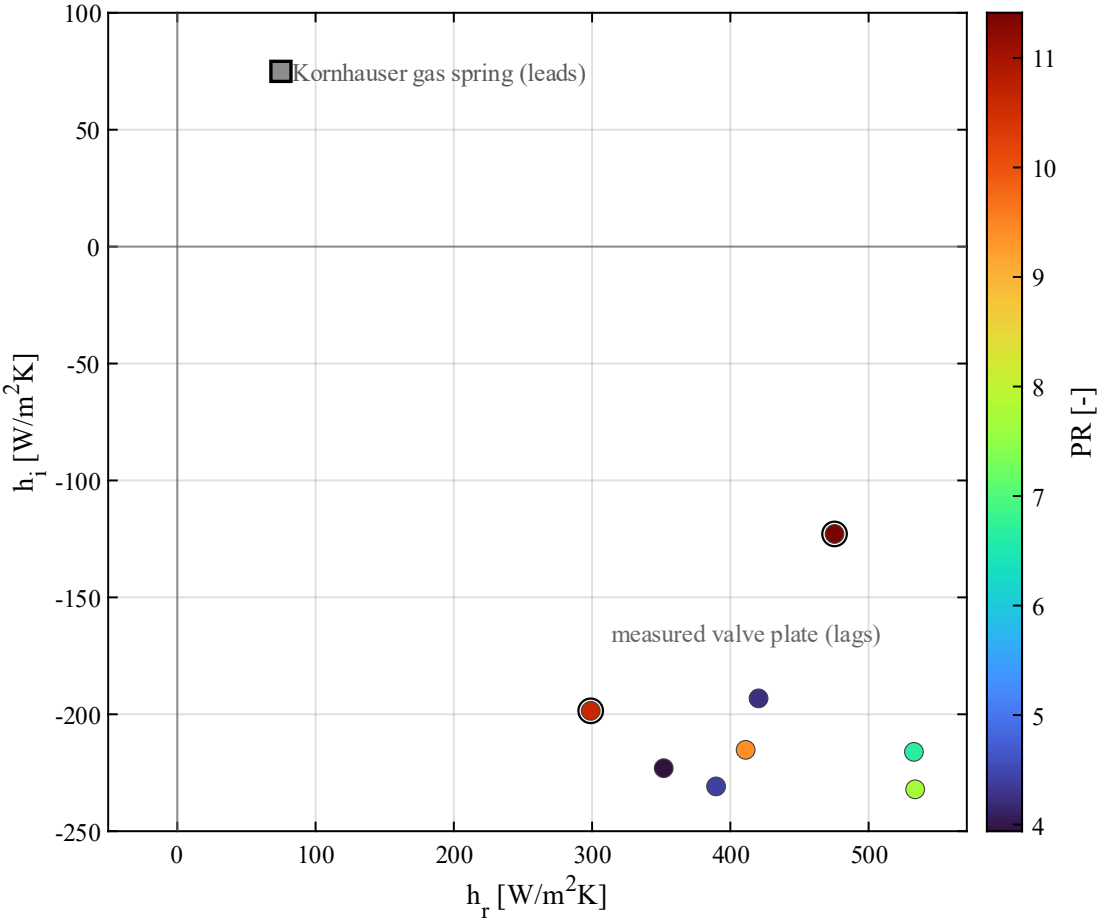

Figure 6.29 Two-term heat transfer coefficient at the valve plate in the complex plane. The in-phase part is the real axis and the quadrature part the imaginary axis, so a quasi-static coefficient lies on the real axis. The measured points lie below it at every load, which shows the flux lags the temperature difference, while the gas-spring prediction of Kornhauser lies above it and leads. Coloured by pressure ratio, with open symbols at the two highest loads.

The failure of the quasi-static coefficient is documented just as clearly. In an engine, the instantaneous heat flux stays high during compression and goes negative during expansion without vanishing at the gas-wall temperature crossing, so a coefficient formed by dividing flux by temperature difference turns negative and diverges exactly as it does here [14]. The complex coefficient was proposed as the cure for the same failure in a gas spring [47]. The two-term fit used here is that cure in measured form. The two published forms that build this quadrature term into a predictive correlation do not transfer to the compressor. A complex coefficient cal-

ibrated on a gas spring assumes a smooth periodic gas temperature and breaks at the valve events, where the sharp change in the rate of the gas temperature produces unphysical spikes [47]. A derivative term scaled on the rate of cylinder volume change degenerates on this machine, its constants fitting to zero because that kinematic rate does not follow the thermal phase of the measured flux [58]. A freely fitted quadrature term carries the phase that the published constants cannot. A Lissajous plot puts two quantities that both oscillate over the cycle on the two axes, against each other rather than against crank angle. A constant-coefficient law would trace a single straight line through the origin, and a phase lag opens that line into a loop whose width is the lag. Plotting the measured flux against the gas-wall temperature difference at the valve plate shows the lag directly, as an open loop that does not pass through the origin rather than the straight line of a quasi-static coefficient (Figure 6.30). The present data add that the quasi-static description fails not only at the crossings but across about a quarter of the cycle in late compression, so the breakdown is wider than a local artefact. Resolved by cycle phase, the lag is strongly localised. In the re-expansion of the clearance gas the flux follows the temperature difference to within about 1.5 degrees at every load, so this part of the cycle is effectively quasi-static. The lag is carried by the compression and the valve-open phases, and the whole-cycle two-term phase is the weighted average of a near-zero expansion and a strongly lagged compression.

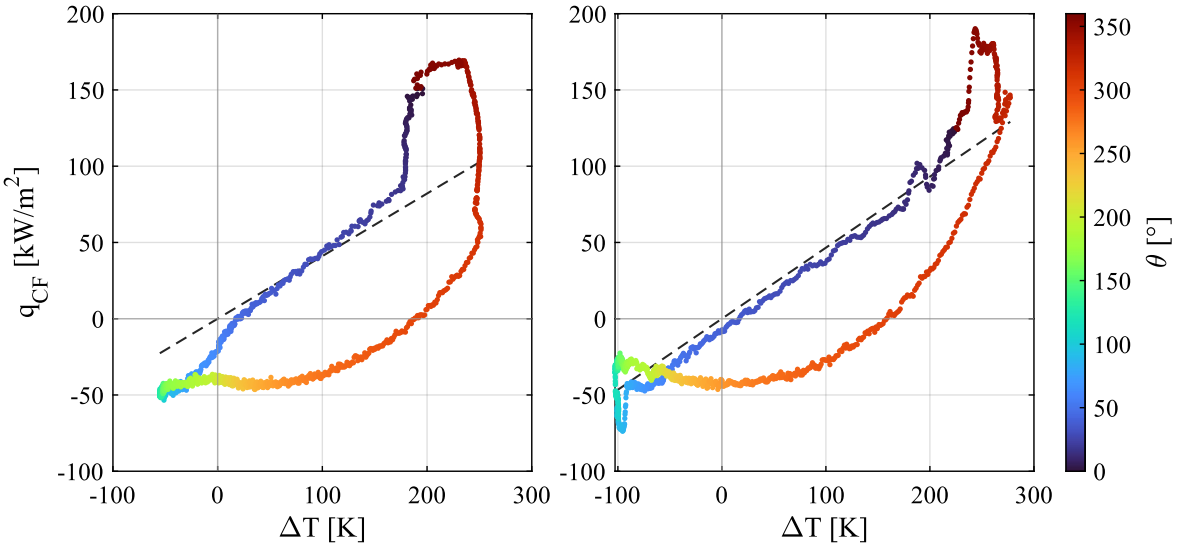

Figure 6.30 Measured heat flux against the gas-wall temperature difference at the valve plate (Lissajous loop) at two representative pressure ratios, coloured by crank angle: (a) a medium load (PR ≈ 6.7) and (b) a high load (PR ≈ 11.4). The two quantities are plotted against each other rather than against crank angle, so a constant-coefficient law would trace a single straight line and a phase lag opens it into a loop. The dashed line in each panel is the quasi-static fit. The open loop and the non-zero flux where the temperature difference vanishes show the phase lag.

At the lower liner sensor, the two-term description holds only up to PR ≈ 4.4. At higher loads the fitted phase jumps to about +120 to +134 degrees and the coefficient of determination drops toward zero, so even the two-term bulk model fails there. At the upper liner sensor, the fit does not reach a usable quality at any load, because the exposed part of the cycle leaves only a weak signal driven by local events. The jump coincides with the transition identified independently

by the Aigner inflow term and by the reconstructed charge temperature between PR 4.4 and 6.7. The presentation therefore combines three elements. The phase-by-phase averages are reported where they are valid. The two-term model describes the valve plate. The documented failures serve as evidence of stratification.

Five independent observations point to the same mechanism. The reconstructed charge temperature at the suction valve closing exceeds the suction chamber temperature far beyond what wall heating of a well-mixed gas can deliver. The inflow Stanton number is not identifiable from the bulk temperature difference. The heat flux at the valve plate lags the bulk temperature difference. The quasi-static correlations underestimate the valve plate swing the most. The phase-averaged suction coefficient at the liner changes sign between PR 4.4 and 6.7, together with the phase flip of the two-term fit. A stratified charge with a cold near-wall layer below a hot mixed core, the non-uniform charge anticipated in Chapter 2, explains all five.

No published measurement resolves this near-wall layer directly. The cold-wire records of Morriesen [3] sample a single point in the suction chamber, so they capture the transient of the bulk gas but not the gradient between the core and the wall inside the cylinder. The present surface measurement is sensitive to that gradient, because the heat flux is read at the wall. The two pictures are consistent. A bulk gas already several degrees out of equilibrium with the adiabatic reference, as their probe shows, leaves the wall-side gas colder still once the suction jet sweeps it along the surface. The effect grows with load and becomes dominant at the lower liner between PR 4.4 and 6.7, the same threshold at which the near-wall coefficient changes sign.

The simulations that resolve the in-cylinder flow support a jet-driven layer rather than a well-mixed charge. Pereira [48] computed the heat flux separately on the piston, the valve plate and the cylinder wall, and found that the suction and discharge jets, not the piston motion, set the flux during the valve-open periods, at a level that differs from one surface to the next. Disconzi [9] reached the same conclusion and found the effect too large for any piston-speed scale, which is why they built their velocity from the valve mass flow. Both pictures describe a charge stirred by a wall-hugging jet, which matches the axial difference measured here between the valve plate and the liner. This is also the assumption that the system-level models of the field set aside. The single-zone control volumes used in lumped models treat the cylinder gas as one well-mixed temperature, which is adequate for the cycle-integral energy balance but cannot carry the near-wall gradient that controls the instantaneous flux [2], [27], [51].

6.10Validation of Heat Transfer Correlations

The five correlations evaluated here share a single property. Each predicts the instantaneous in-cylinder HTC over the whole cycle in the dimensionless Nusselt or Stanton form and needs only quantities available from the zero-dimensional model [4], [5], [6], [9], [10]. They span the engine experiments, the compressor experiment, and the two-dimensional and three-dimensional CFD that bound current practice, and they are the set assessed against a thermodynamic

model by Tuhovčák [11]. The remaining reviewed forms are either superseded direct-expression formulas, variants of an included correlation, dynamic models that need the instantaneous gas-temperature derivative, or fits specific to one machine, so they fall outside the like-for-like comparison. Section 6.9 shows this directly. On the present machine the derivative term degenerates to a zero constant and the gas-spring complex coefficient breaks at the valve events, so neither transfer as a predictive correlation.

The five correlations are first evaluated exactly as published, with the experimental gas temperature and without any adjustment (Fig. 6.31). The deviation is reported for each surface and for each phase of the cycle (Fig. 6.31). None of the correlations reproduces the measured swing at the valve plate, where the underestimation is the largest.

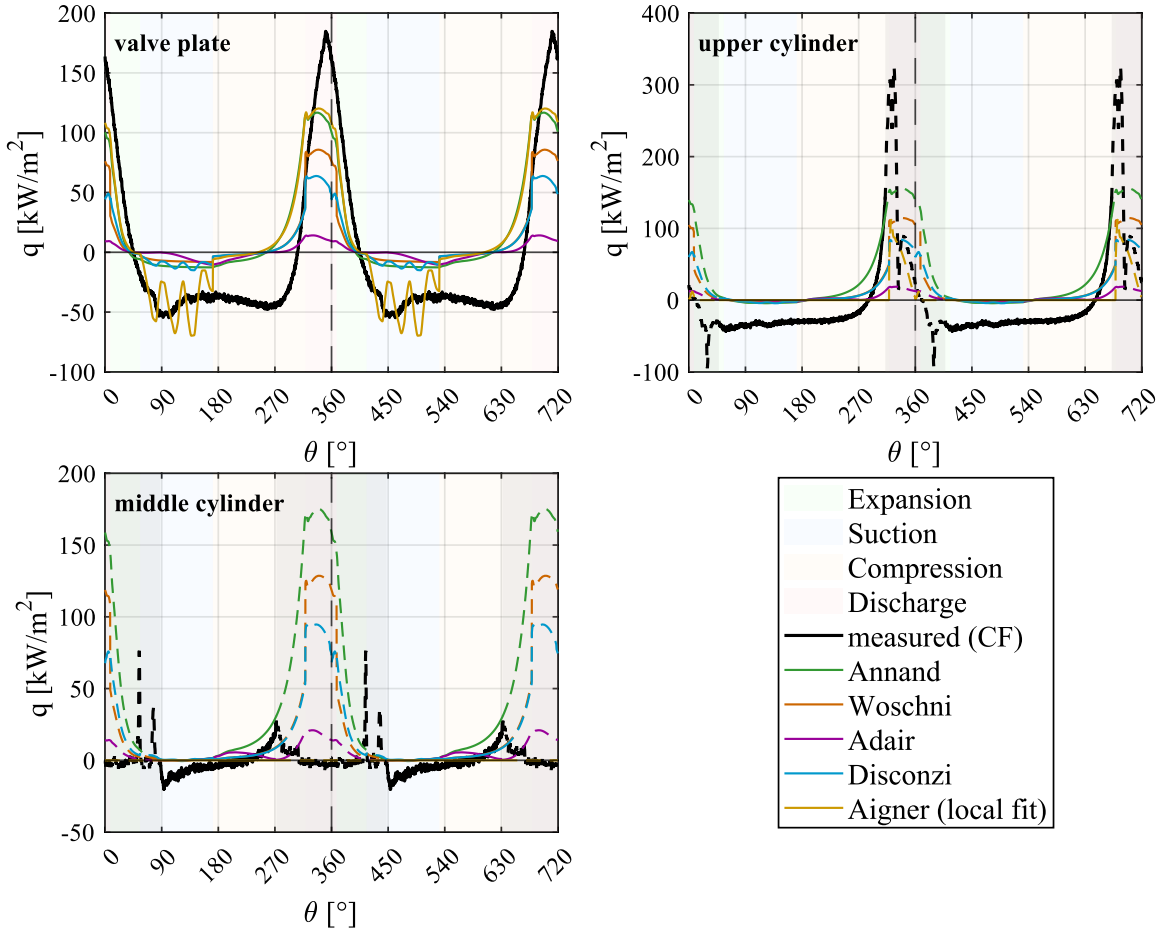

Figure 6.31 Measured heat flux for each surface against the as-published correlation predictions at a representative pressure ratio, over two revolutions. (a) valve plate, (b) upper cylinder, (c) middle cylinder. Each panel gives the measurement and all five correlations. Annand, Woschni, Adair and Disconzi use their literature constants, and Aigner, whose inflow, outflow and instantaneous-piston constants are not published, uses its local fit.

The comparison for individual surfaces has an axial structure. The standard correlations underestimate the swing at the valve plate by a factor of roughly 2 to 4, and the Adair correlation (Equation 2.7) by about 8 to 12. In a conjugate heat transfer CFD study, the classical Annand, Woschni and Disconzi correlations all underpredict the in-cylinder heat transfer [50]. Piston-speed correlations show the same shortfall in earlier compressor work. A direct numerical so-

lution gave instantaneous fluxes about an order of magnitude above the classical form, an independently fitted correlation needed a leading constant more than an order of magnitude larger, and a high-pressure measurement required a separate flow-velocity term in the Reynolds number to represent the heat transfer at valve opening [7], [8], [45]. Restoring Adair's original swirl constant (Equation 2.7c) in place of the reduced Brok value would raise the predicted coefficient only in the phases around top dead centre, and there only by roughly a factor of 1.7, because the characteristic velocity doubles and the Nusselt number scales with its 0.8 power. This is far too small to close that gap. The Aigner correlation (Equation 2.13) alone does not underestimate the swing, at 0.7 to 1.6, but reproduces it with the wrong phase. The valve jets reach velocities around 32 m/s [3], an order of magnitude above the mean piston speed of 2.2 m/s, and no correlation built on the piston speed can represent them. At the upper liner position the correlations overestimate the swing. At the lower liner position the agreement during suction is nearly exact. A spatially averaged correlation thus describes the conditions in the middle of the liner, while the real coefficient grows toward the cylinder head. None of the published correlations contains an axial dependence [12]. A three-dimensional simulation of a small fast-running piston compressor that resolves the heat flux separately on the valve plate, the piston, and the liner shows the same surface-to-surface variation, with the highest coefficients where the gas streams fastest through the valve ports and the liner carrying only a few % of the total, so the flux follows the valve flow rather than the piston motion and no single spatially averaged correlation can hold it [57].

A global fit of the leading constants follows. The fitted constants (Section 5.4) are reported together with the spread of the two reconstruction schemes of Section 5.7. The Annand constant is a = 0.70 to 0.82, consistent with the value 0.7 recommended for air. The Woschni and Adair constants exceed the published values several times. The velocity exponents of the Disconzi correlation collapse toward zero in the fit. The inflow Stanton number of the Aigner correlation is not identifiable from the bulk temperature difference during suction. A low residual alone does not imply physical fidelity. The flexible phase factors of the Woschni form can bend the prediction in two zones, while the more physically structured Disconzi form reaches a similar residual without stressing any parameter.

Figure 6.32 repeats the surface-by-surface comparison with the fitted constants. At the valve plate the fitted forms rise toward the measured peak, which removes much of the underestimation of the as-published curves, but they keep a single smooth hump and do not follow the finer structure that the discharge valve dynamics (Fig. 6.13) and the valve jets impose on the measured flux. These forms were inherited almost entirely from internal combustion engine work and only rarely built for compressors [12], so a global fit rescales them but cannot supply the valve plate structure they never held. The two liner thermocouples lie under the piston through the part of the cycle that holds the peak flux, so only the low-flux phases stay exposed, and there the difference between the fitted forms and the measurement is small. The fit therefore lowers the residual at the valve plate (Fig. 6.32) by matching the amplitude of the peak and not its shape, in line with the caution above that a low residual need not mean physical fidelity.

During suction the fitted Disconzi and Aigner curves break into large oscillations that reach

about −160 and −250 kW/m², far below the smooth measured flux of about −50 kW/m². These are not physical. Annand, Woschni and Adair scale the Reynolds number on the mean piston speed, but Disconzi and Aigner scale it on a through-valve gas velocity, which Aigner builds from the time derivative of the cylinder mass. During suction that velocity amplifies the cylinder pressure ripples of the suction tract (Section 6.7), so the Reynolds number and the HTC swing hard, and the heat flux carries the swing. The global fit deepens the swing rather than damping it, because the only constant with real leverage in these two forms is the one that scales the valve-flow term, and the fit raises it to reach the measured amplitude near top dead centre, which inflates the same term during suction. The oscillations survive because they largely cancel over the phase, so their integral stays close to the measured flux even while the instantaneous values are wild. The integrated heat transfer is therefore preserved, and with it the effect on the performance parameters, while the instantaneous prediction is not. The measured flux stays smooth because the Cook and Felderman inversion works from the wall surface temperature and never uses this velocity, so the excursions belong to the correlation input and not to the real heat flux.

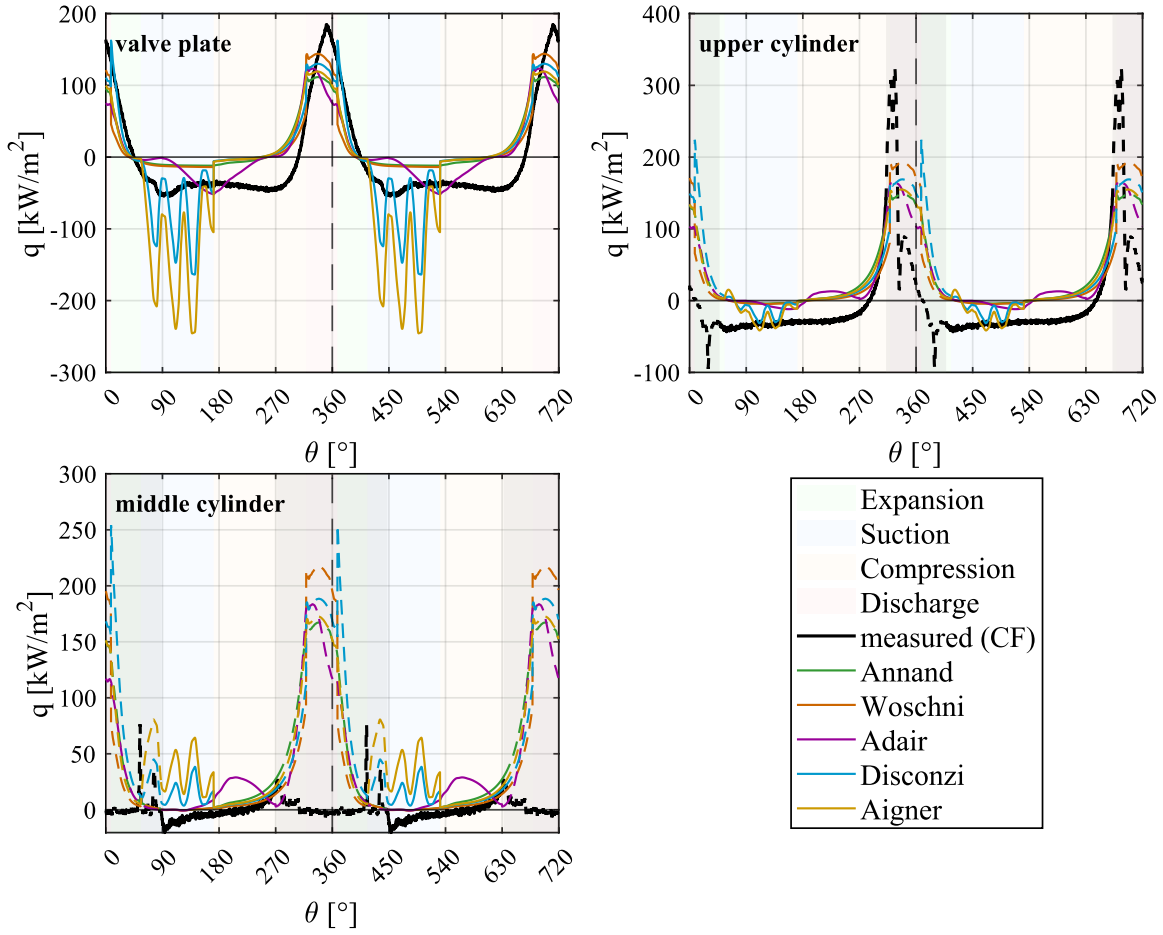

Figure 6.32 Measured heat flux for each surface against the globally fitted correlation predictions at a representative pressure ratio, over two revolutions. (a) valve plate, (b) upper cylinder, (c) middle cylinder. Each panel shows the measurement and all five correlations evaluated with the fitted constants of Table 6.1.

The fitted Aigner mean Stanton number, 0.042, can be compared directly with the value Aigner

derives from CFD for the cylinder head, which scatters between about 0.023 and 0.054 over twenty-four cases. The present fit reproduces the source correlation's own value to within about thirty per cent, and at the low Reynolds number of this compressor, of order 10^4, where Aigner's cases cluster near 0.04 to 0.05, the agreement is closer still. Both the fitted and the CFD values lie three to seven times above a plain turbulent-duct estimate from the Reynolds–Colburn analogy [94], the modest enhancement expected for the more agitated flow inside the cylinder, so the bulk heat transfer is of the right order of magnitude rather than an artefact of the fit.

Table 6.1 Fitted leading constants of the correlations. The v3 value is the centre of the primary reconstruction scheme, the band covers both schemes of Section 5.7, and the published value is the original literature constant. Aigner reports no constants in tabular form. The mean Stanton number is read from the published scatter graph and ranges from about 0.023 to 0.054. The inflow Stanton number is not given

Constant	Fitted (v3)	Scheme band	Published
Annand a	0.700	0.70–0.82	0.7
Woschni C	0.0624	0.062–0.069	0.035
Adair C	0.293	0.29–0.33	0.053
Disconzi C_{base}	0.173	0.17–0.19	0.08
Aigner St_m	0.0417	0.042–0.048	0.023–0.054
Aigner St_{in}	0.455	0.082 to 0.455 (factor 5.5)	—

The fitted constants might be expected to inherit the negative bias of the mean measured flux from the thermocouple installation (Section 6.2). A deliberate +35 % offset on the mean heat flux, of the order of the mean-flux under-prediction reported [89], shifts the structural constants (those of Annand, Woschni, Adair and Disconzi, together with the Aigner mean Stanton number) by less than 0.6 %. It shifts the ill-conditioned Aigner inflow Stanton number by at most +1.6 %. Both are an order of magnitude below the reconstruction-scheme band of Section 5.7. The constants are set by the cyclic amplitude of the heat flux, not by its mean level, so the installed bias changes neither the ranking nor the shape comparison (Table 6.2).

Table 6.2 Sensitivity of the fitted leading constants to a deliberate +35 % offset on the mean heat flux (installed-error test of Section 6.2). The shift is the change of the multi-run centre relative to the unbiased baseline, and reaches +1.6 % for the Aigner inflow Stanton number at the highest pressure ratio

Constant	Baseline	+35 % offset	Shift
Annand a	0.700	0.697	−0.4 %
Woschni C	0.0624	0.0622	−0.3 %
Adair C	0.293	0.292	−0.4 %
Disconzi C_{base}	0.173	0.172	−0.4 %
Aigner St_m	0.0417	0.0415	−0.5 %
Aigner St_{in}	0.455	0.457	+0.7 %

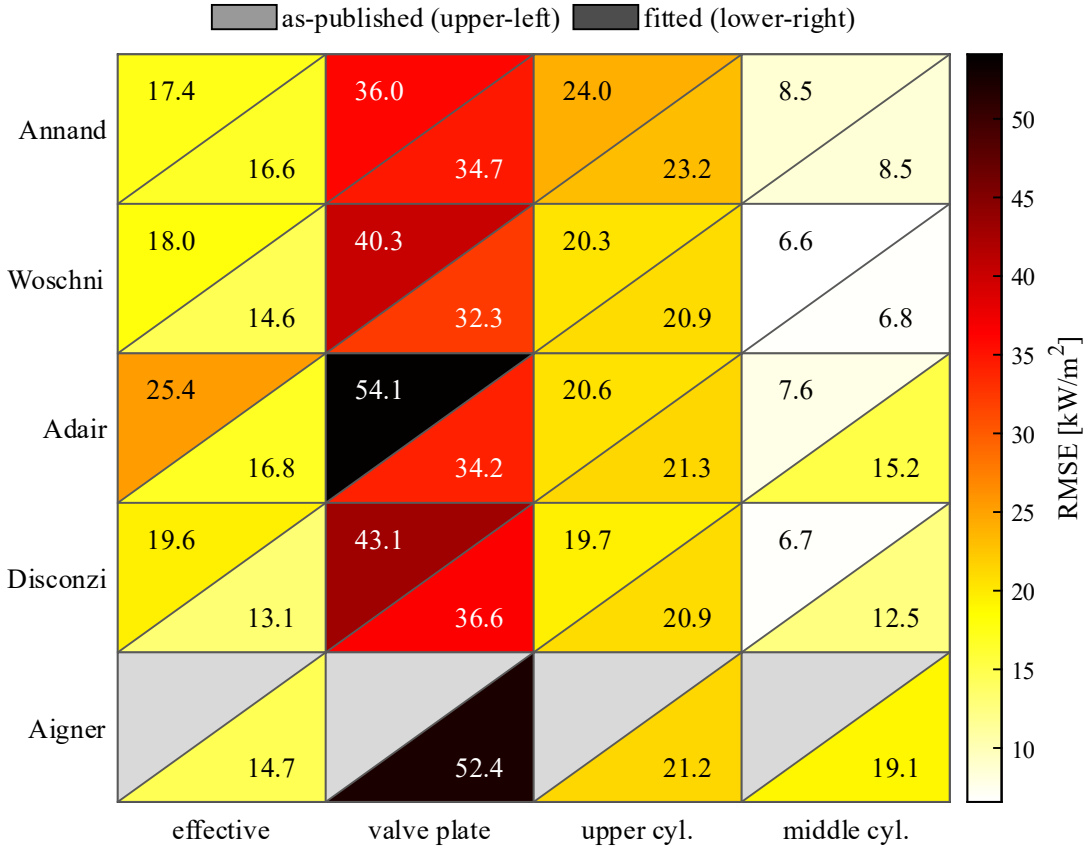

Figure 6.33 RMSE of the correlation predictions for each surface, averaged over all pressure ratios.

The root mean square error (RMSE) of every correlation on each surface, as published and after the fit, is collected in Figure 6.33. The comparison answers the question whether velocity scales beyond the mean piston speed pay off. After the fit, all five correlations reach a similar residual of roughly 11 to 21 kW/m², lowest for the Disconzi form at 11 to 16, and rising with the pressure

ratio (Figure 6.34). The additional terms improve the prediction only marginally, because the dominant error is the phase structure of the heat flux, not the velocity scale. That phase structure is captured directly by the two-term coefficient of Section 6.9, whose quadrature component carries the lag that no quasi-static form can reproduce. The instantaneous piston velocity in particular carries no information beyond the mean, since the Stanton component of the Aigner form tied to it fits to zero in every run. This is the structural disagreement formulated in hypothesis H3.

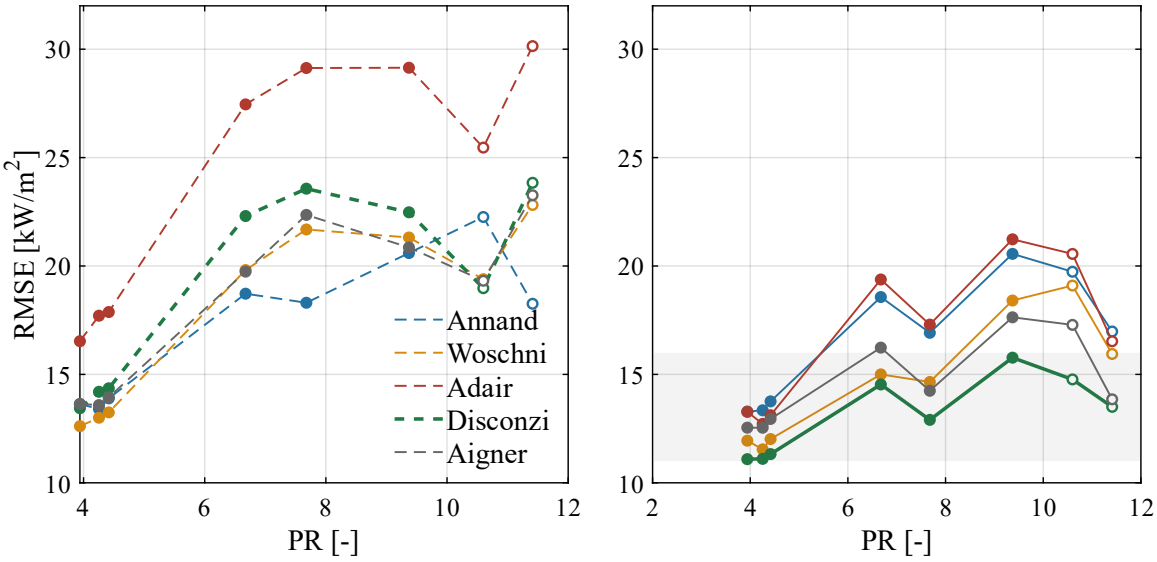

Figure 6.34 Root mean square error of the five correlations against the measured flux versus pressure ratio: (a) as published and (b) after refitting the leading constants. After refitting all forms reach a similar residual, lowest for the Disconzi form at 11 to 16 kW/m² and within about 21 for the others, and the floor rises with the pressure ratio. The shaded band in (b) marks this floor.

Three results stand out from the comparison. First, the measured flux changes direction at least twice in each revolution at every surface, and its cycle mean carries heat from the wall into the gas at the valve plate, with −0.7 to −1.2 kW/m², and at the upper liner, with −0.2 to −0.9 kW/m². This inward cycle-mean flux at the head-end surfaces feeds the in-cylinder superheating and identifies the head end of the cylinder as its source. The lower liner is shielded by the piston through the compression and expansion phases and is excluded from the flux evaluation. Second, the quasi-static correlations underestimate the heat transfer most at the valve plate, where the jets of both valves act, and the shortfall is concentrated in the valve-open phases that they cannot represent. Third, the disagreement is structural rather than one of calibration, and it shows in three independent ways: after the fit of the leading constants all correlations still reach a similar residual, the heat flux lags the bulk temperature difference by 12 to 32 degrees at the valve plate, and the quasi-static coefficient turns negative over a quarter of the cycle, with the bulk description failing entirely at the liner above PR ≈ 4.4.

No earlier study had confronted the standard correlations with a measured instantaneous in-cylinder heat flux in this way. The comparisons in the recent literature were made differently. Tuhovcak [11] ran the five correlations through a thermodynamic cycle model and ranked them by their effect on the predicted volumetric and isentropic efficiency. Their accuracy had not

been verified experimentally because of the difficulty of the measurement. The more recent comparisons keep the same numerical basis. In a numerical model of a large-bore carbon dioxide compressor the correlations were ranked by their effect on predicted performance [56], and complex Nusselt forms were evaluated numerically for a cryogenic liquid-hydrogen pump [18]. Both extend the comparison to new fluids and conditions, but neither tests the correlations against a measured instantaneous in-cylinder flux.

The two forms that carry a valve-flow scale were themselves built from simulation. Both the Disconzi (Equation 2.12) and the Aigner (Equation 2.13) correlations were derived from CFD of specific compressor geometries. The first using a valve mass-flow velocity and the second using three-dimensional Stanton numbers, so each carries the geometry it was tuned on [9], [10]. The present comparison closes that loop with measurement, and it confirms from data that the valve-flow scale of Disconzi is the structurally closest, as the jet-dominated flow would suggest.

For the prediction of the instantaneous heat flux none of the published correlations is reliable without refitting. For integral performance parameters all of them remain usable, because the errors largely cancel over the cycle, and the choice then matters within the spread identified by Tuhovcak [11]. The phase information of Section 6.9 indicates what a future correlation needs beyond a velocity scale. Such a correlation needs a quadrature term that carries the 12 to 32° lag of the heat flux behind the bulk temperature difference at the valve plate, of the opposite sign to the gas-spring model of Kornhauser [47], and an axial dependence that none of the published forms contains. A larger velocity scale alone does not reduce the residual, as the fit of the leading constants shows.

The compressor tested here is an open, air-cooled machine, directly driven by its motor, and this sets it apart from much of the cited literature. None of these differences, however, reaches the structural result. The phase lag of the flux behind the temperature difference, and the inability of a single static coefficient to follow it, arise from the form $q = h\,\Delta T$ itself and would appear on any reciprocating machine, so this part of the disagreement is not specific to the open, air-cooled configuration.

The simulations of Disconzi [9] and Pereira [48], and the thermal models of Ribas [2] and Morriesen [3], concern hermetic or semi-hermetic refrigeration compressors, in which the motor shares a shell with the cylinder and is cooled by the suction gas that passes over it, so the gas is already warmed when it reaches the cylinder. The exception among the cited work is Tuhovcak [24], whose experiments were carried out on the same open compressor as the present study, so there the machine type is shared, and the difference is the integral-versus-instantaneous one already noted.

Against the hermetic studies, two consequences follow. The shell-recirculation path that dominates the suction superheating of a hermetic machine is absent, so the in-cylinder superheating measured here is a cleaner isolate of the in-cylinder and suction-line contribution. The wall temperature is set by an external cooling stream rather than by a warm shell interior, so the gas-wall temperature difference that drives the flux follows a different distribution from the ma-

chines on which the correlations were calibrated. Part of the disagreement with the published correlations may therefore reflect this difference in cooling and boundary conditions, not only their structural limits.

The working fluid is a further difference. The compressor correlations were calibrated on refrigerants rather than air, so even with temperature-dependent air properties in the dimensionless groups the calibrated constants are carried outside the fluid for which they were fitted.

A consolidated note on the limits of these results is in order. The crank-angle-resolved heat flux and the coefficients rest on the high-speed campaign, eight runs covering pressure ratios from about four to eleven, with the lowest-pressure run excluded because its fitted constants collapse toward zero and two high-load runs flagged for the uncertainty in the suction-flow scaling. The absolute cycle-mean flux carries the installed error of the flush sensor, whose higher thermal product overstates the wall temperature swing, so its magnitudes are read with that bias in mind. The shielded lower liner, the adiabatic piston, and the coefficient that cannot be formed at the temperature crossings or at the liner above a pressure ratio of about 4.4 are the measurements that the next chapter sets out to tighten.

7 CONCLUSION

This chapter summarises the findings of this work, states the contribution to the field, and outlines directions for future research.

7.1 Summary of Findings

This work measured the instantaneous heat transfer inside the cylinder of a small reciprocating compressor while it ran across several pressure ratios. The surface temperature was recorded with flush-mounted coaxial thermocouples at the valve plate and at two liner positions, sampled at 50 kHz and ensemble-averaged over many cycles. The heat flux was recovered from the surface temperature with the CF and Reichelt formulations of the semi-infinite solid, and the instantaneous gas temperature was reconstructed from the measured cylinder pressure through a phase-resolved thermodynamic model. The three research questions of Chapter 4 can now be answered.

The first question concerned the size of the instantaneous surface fluxes and how they evolve over the cycle and with the pressure ratio. The instantaneous heat flux reaches tens of kilowatts per square metre and exceeds a hundred at the valve plate. It changes direction at least twice in each revolution at every surface and grows with the pressure ratio. Its cycle mean is directed from the wall into the gas on the inner surfaces, from −0.7 to −1.2 kW/m² at the valve plate and from −0.2 to −0.9 kW/m² at the upper liner. The lower liner is shielded by the piston for most of the cycle and is not evaluated. The gas is heated mainly from the head end of the cylinder, and the charge at the closing of the suction valve is superheated above the suction chamber by 35 to 85 K. This confirms the first hypothesis and shows that the in-cylinder heat transfer feeds the suction gas superheating directly.

The second question asked whether a HTC can be recovered from flush-mounted coaxial thermocouples at the speed of a small production compressor. The HTC can be obtained reliably from the coaxial thermocouples on the valve plate, where a two-term fit that carries both a magnitude and a phase holds across the whole load range, with a magnitude of 296 to 521 W/m²K and a phase of −12 to −32 degrees. It cannot be obtained as a pointwise quasi-static coefficient, which diverges and changes sign where the heat flux crosses zero, nor at the liner above a pressure ratio of about 4.4, where the bulk description breaks down. The limitation is the quasi-static definition of the coefficient, not the coaxial thermocouple, which resolves the temperature swing at the sampling rate of a production compressor. The phase of the flux lags the gas-wall temperature difference, which is the opposite sign to the gas-spring model and points to a cold layer left at the wall by the suction jet.

The third question asked which correlation describes the measured heat transfer best and in which phases the correlations fail. None of the five published correlations reproduces the measured instantaneous flux without a refit of its leading constant. The Disconzi form, which scales

its velocity on the valve mass flow, is the structurally closest, while all of them fail in the valve-open phases at the valve plate, where the jets of both valves act. After the constants are refitted the correlations reach a similar residual, because the dominant error is the phase structure of the heat flux and not the velocity scale. For the cycle-integral parameters that drive the efficiency the correlations remain usable, because the phase error averages out over the revolution. These results confirm the second and third hypotheses, that the quasi-static correlations underestimate the heat transfer in the valve-open phases and that the disagreement is structural rather than a matter of a single constant.

Three further results emerged from the same measurements. The charge inside the cylinder is not well mixed. A cold layer left at the wall by the suction jet sits below a hotter core, and this stratification bends the HTC at the valve plate and reverses its sign at the lower liner above a pressure ratio of about 4.4. The suction flow is acoustically resonant at the two highest loads, where a running-speed order coincides with the quarter-wave frequency of the suction line, a coincidence identified from the mode shape rather than from the frequency alone. Part of the apparent superheating at high load is not wall heating but blow-by past the discharge valve, read by the cycle closure as heat, which the instantaneous reconstruction separates from the real wall contribution.

The leakage behind this was quantified from the measured pressures and the cycle energy balance. The re-expansion exponent falls from about 1.57 at the lowest load to about 1.07 at the highest, well below the adiabatic value, which shows the gas flowing back through the discharge valve. Three independent estimates, the energy residual, the pressure-driven orifice and the volume overshoot, agree at low and moderate load and place the backflow near eight and a half % of the trapped charge at the highest load. The piston-ring blow-by, taken as an upper bound from the annular-gap model, reaches a comparable size.

7.2 Contribution to the Field

The central contribution of this work is the first direct experimental test of the standard in-cylinder heat transfer correlations against a measured instantaneous heat flux, obtained on a running compressor of this class across a range of pressure ratios. The earlier comparisons in the literature were numerical and ranked the correlations through their effect on a simulated efficiency rather than against a measured flux. This comparison provides the missing experimental reference and marks where the published forms fail and why.

The distinction from the established approach lies in what is compared. The reference simulation tools of the field, such as the zero-dimensional energy-balance model of Tuhovcak implemented in their reComp tool, insert a heat transfer correlation into a cycle and judge it by how well the computed indicator diagram and the efficiency match a global measurement. The correlation is never confronted with the local instantaneous flux it is meant to predict, and the cycle integral hides its phase and its surface dependence. The present work removes that intermediate step. It measures the flux at the wall, at the crank-angle resolution and on the surfaces

where the correlation is evaluated, so each correlation is tested against its own output rather than against a downstream quantity that averages its errors away.

The credibility of that measured flux rests in part on its independence of the inversion method. The flux was recovered in two ways, by the CF convolution in the time domain and by the Reichelt analytical solution in the Laplace domain, and the two agree within a few percent at the valve plate. They share the one-dimensional semi-infinite model of the wall but differ completely in their mathematics, so the agreement shows that the recovered flux is method-independent and is not an artefact of the noise sensitivity of the time-domain scheme. The semi-infinite model itself is supported separately, by the thermal penetration depth staying well below the sensor thickness over a cycle.

The work also contributes a validated measurement and reduction workflow that combines ensemble averaging, the Reichelt formulation of the heat flux, a synchronised 50 kHz acquisition, and a phase-resolved thermodynamic reconstruction of the gas temperature. Two physical results follow from it. The heat flux at the valve plate lags the temperature difference and the charge carries a cold near-wall layer, which together explain why a quasi-static coefficient cannot describe the valve plate. The determination of the HTC during the discharge phase, and at the liner above a pressure ratio of about 4.4, is identified as a distinct limit of the bulk framework rather than a shortcoming of the sensor.

The work establishes several physical results that had not been measured inside a running compressor of this class. The heat flux at the valve plate lags the gas-wall temperature difference, with a sign opposite to the adiabatic gas-spring model, and a two-term coefficient that carries both a magnitude and a phase describes it across the whole load range. The charge carries a cold near-wall layer, and the in-cylinder superheating it produces, between 35 and 85 K at the closing of the suction valve, extends the superheating chain previously measured only along the suction path to the wall of the cylinder itself. The cycle-averaged flux is directed from the wall into the gas on the inner surfaces, which fixes the head end of the cylinder as the source of the in-cylinder part of the superheating.

Two further contributions follow from the same data set. The suction-side unsteadiness is shown to be an acoustic resonance of the suction line rather than a kinematic harmonic of the induction pulse, and the distinction is made with a mode-shape test that does not need an independent acoustic model. The reconstruction also separates the real wall-driven superheating from the apparent superheating produced by blow-by, which the integral models of the field cannot distinguish because a single polytropic exponent absorbs both. Taken together, these results provide a measured reference against which the zero-dimensional and the system-level models can be checked, not only for their cycle-integral output but for the instantaneous heat transfer that drives it.

The practical reading for a designer is that a correlation tuned to reproduce the cycle-integral efficiency still cannot be trusted for the local instantaneous flux that sets the wall temperature and the thermal load on the valve plate. The in-cylinder superheating measured here is large enough to carry a real efficiency penalty, which marks the head end of the cylinder as a concrete

target for reducing the heat fed into the suction gas.

7.3 Recommendations for Future Work

Several directions follow from the limits of this work. The measurement covered three surface positions, so a denser set of coaxial thermocouples would map the axial variation of the heat flux that the present data only sample. The working fluid was air, and an extension to refrigerants would test the correlations under the conditions for which they are most often used. The measured instantaneous flux is a natural boundary condition for a coupled simulation, so pairing it with a CFD model would let the near-wall field be resolved directly rather than inferred. A more detailed valve dynamics model would sharpen the instantaneous mass flow rate at discharge, which is the largest single systematic of the reconstruction during the open phases, alongside the unmeasured piston flux.

Several of these directions address limits of the present measurement directly. The piston face was not instrumented and was treated as adiabatic, which is the largest single systematic error of the gas-temperature reconstruction near top dead centre, so a heat flux sensor on the piston crown would tighten the high-load temperatures. The determination of the coefficient during the discharge phase, and at the liner above a pressure ratio of about 4.4, remains open, and a measurement that resolves the near-wall layer, for example with a second sensor at a known depth, would test the stratification picture directly.

Two of the pressure features reported here are still read from the pressure signals alone. The low-load fluctuation on the cylinder pressure is ascribed to flutter of the discharge reed valve, and the oscillations that persist after the suction valve closes are ascribed to a late reattachment of that valve. A direct measurement of the valve lift, by a proximity probe or a strain gauge on the reed, would confirm or rule out the valve-dynamic origin of both. It would also serve the central quantity of this work, the instantaneous heat flux, by tying its structure to the valve events that the piston-speed correlations cannot represent, so the discharge and suction phases of the flux could be read against the measured valve motion rather than inferred from the pressure trace. A further step is the instantaneous bulk gas temperature, which would give the HTC directly and remove the reconstruction, although no probe yet resolves it within the cycle, which is the reason the present work reconstructs it. The piston-ring blow-by was taken only as an upper bound from the annular-gap model, so a direct measurement of the ring leakage would fix its share of the high-load mass balance that the cycle energy balance now bounds only from above.

On the modelling side, the measured instantaneous flux is the natural target for a correlation that goes beyond a velocity scale. The phase results indicate that such a correlation needs a quadrature term to carry the lag of the flux behind the temperature difference, together with an axial dependence that none of the published forms contains. Coupling the measured flux into a zero-dimensional or a system-level compressor model, as a boundary condition or as a validation target, would let the effect of the in-cylinder heat transfer on the volumetric and isentropic

efficiency be assessed against data rather than against another correlation. An extension of the rig to a refrigerant and to more than one cylinder would then place these findings in the conditions of a production machine.

PUBLICATIONS RELATED TO THE THESIS

P. Bouchal, J. Hejčík, and M. Jícha, "Heat Flux Assessment in Reciprocating Compressor," in *EPJ Web of Conferences*, EDP Sciences, 2022, p. 01006. doi: 10.1051/epjconf/202226401006.

P. Bouchal, J. Hejčík, and M. Jícha, "Heat Flux Assessment in Reciprocating Compressor," in *EPJ Web of Conferences*, EDP Sciences, 2024, p. 01004. doi: 10.1051/epjconf/202429901004.

P. Rapta, J. Hejčík, and M. Jícha, "Thermocouple Influence on Heat Transfer Coefficient Measurement," in *Proceedings of the 10th IIR Conference on Compressors and Refrigerants*, Slovakia: International Institute of Refrigeration, 2024. doi: 10.18462/iir.compr.2024.0614.

OTHER PUBLICATIONS

HÁJEK, Ondřej, **BOUCHAL Patrik**, Ondřej CEJPEK, Milan MALÝ, Jiří HÁJEK, František PRINZ, Dawid ZAWADSKI, Michal BLATKIEWICZ and Miroslav JÍCHA. Characteristics of droplets formed on the outer surface of the rotating packed bed. EPJ Web of Conferences. 2024, 299, 01013. ISSN 2100-014X. doi: 10.1051/epjconf/202429901013

HÁJEK, Ondřej, **BOUCHAL Patrik**, Milan MALÝ, Dawid ZAWADSKI, Michal BLATKIEWICZ, Miroslav JÍCHA. Comparative analysis of droplet characteristics generated in the outer cavity of RPB for two packings. In: ILASS-Asia 2023 – 23rd Asian Meeting on Liquid Atomization and Spray Systems, Jeju: ILASS-Asia. 2023. Available at: www.ilass-asia2023.org/Proceedings.asp

ZÁLEŠÁK Martin, **BOUCHAL Patrik**, OSTRÝ Milan, HEJČÍK Jiří. Experimental set up for the investigation of partial phase changes of phase change materials. In EFM21 – 15th International Conference "Experimental Fluid Mechanics 2021". EPJ Web of Conferences. EDP Sciences, 2022. iss. 1, p. 234-237. ISSN: 2100-014X.

ZÁLEŠÁK, Martin, KLIMEŠ, Lubomír, CHARVÁT, Pavel, PECH, Ondřej, **RAPTA, Patrik**. An Effective Thermal Conductivity-based Approach for Modelling of Convective Heat Transfer in a Rectangular Cavity Filled with PCM. Chemical Engineering transactions, 2023, vol. 103, iss. 1, p. 715-720. ISSN: 2283-9216.

Creative activities

Functional sample Green Heat Pump

ŘEHÁK KOPEČKOVÁ, Barbora, FIŠER, Jan, BŘEZINA, Michal, **RAPTA, Patrik**, HEJČÍK, Jiří, PECH, Ondřej, POKORNÝ, Jan, MRKVICA, Tomáš, ZAPLETAL Michal, CARDANO, Giulio, WAN, Qin. EcoHeP modul. Green Heat Pump.

Functional sample ZickZack packing for rotating packed bed

HÁJEK, Ondřej, MALÝ, Milan, **RAPTA, Patrik**, JÍCHA, Miroslav. TN02000025//003-V09. ZickZack packing for rotating packed bed.

Utility model Air handling unit for heating, ventilation and air conditioning

FIŠER, Jan, HEJČÍK, Jiří, **RAPTA, Patrik**, MRKVICA, Tomáš, FOJTLÍN, Miloš. 39045. Air handling unit for heating, ventilation and air conidtioning.

Functional sample HVAC unit for heating/cooling the cabin without direct evaporation of the

refrigerant

FIŠER, Jan, **RAPTA, Patrik**, HEJČÍK, Jiří, PECH, Ondřej, FOJTLÍN, Miloš, MRKVICA, Tomáš. Čikita. HVAC unit for heating/cooling the cabin without direct evaporation of the refrigerant.

Functional sample RPB demonstration unit

HÁJEK, Ondřej, MALÝ, Milan, **RAPTA, Patrik**, JÍCHA, Miroslav. TN02000025//003-V10. RPB demonstration unit

NOMENCLATURE

The symbols below are grouped into Latin letters, Greek letters, dimensionless groups, subscripts, operators, and abbreviations. Units are given in SI; a dash denotes a dimensionless quantity. Where one symbol carries more than one meaning, the meanings are separated by context as noted.

Latin letters

Symbol	Unit	Meaning	Symbol	Unit	Meaning
A	m²	area	A_1, A_2	–	engine-order amplitude
a, b, c	–	correlation constants and exponents	C	–	correlation leading constant
C_d	–	discharge coefficient	C_u, C_p	–	ring-leak shape factors
c	J/(kg·K)	specific heat	c_s	m/s	speed of sound
D	m	bore (characteristic length)	d	m	diameter
E_{miss}	J	closed-phase energy residual	E_0	V	thermopile output voltage
F	–	Pfriem transient ratio function	f	Hz	frequency
g	m	piston-ring radial clearance	h	W/(m²·K)	heat transfer coefficient
i	–	index; imaginary unit	k	–	summation index, engine-order number
k	N/m	reed-valve stiffness	L	m	connecting-rod length
L_w	°CA	history-window length	l_{th}	m	thermal penetration depth
m	kg	trapped gas mass	m	–	acoustic mode number
N	–	thermopile turns	N	RPM	shaft speed
n	–	polytropic exponent	p	Pa	pressure
p	–	Laplace variable	Q	J	wall heat exchanged over a phase
q	W/m²	heat flux	R	J/(kg·K)	specific gas constant

$R_{i,k}$, $S_{i,k}$	–	Reichelt discrete-sum coefficients	r	m	crank radius
r_p	–	orifice pressure ratio	S	m	stroke
s	J/(kg·K)	specific entropy	T	K (°C)	temperature
t	s	time	UA	W/K	thermal conductance
u_{char}	m/s	characteristic velocity	u_p	m/s	instantaneous piston speed
V	m³	volume	W	J	work
x	m	depth below the surface			

Greek letters

Symbol	Unit	Meaning	Symbol	Unit	Meaning
α	m²/s	thermal diffusivity	β	W·s^½/(m²·K)	thermal product
δ	m	thickness	δ_T	–	temperature modulation
δ_v	–	relative volume modulation	δ_0	bar	pressure-transducer offset
ε_c	–	clearance ratio	ε_S	V/K	Seebeck coefficient
η	–	efficiency	θ	° (rad)	crank angle
κ	–	isentropic exponent	λ	W/(m·K)	thermal conductivity
μ	Pa·s	dynamic viscosity	ν	m²/s	kinematic viscosity
ξ	–	penetration ratio	ρ	kg/m³	density
σ	varies	standard deviation	τ	s	time; time constant
φ	–	mixing parameter	Φ	–	mode-shape amplitude ratio
ψ	rad	phase angle	ω	rad/s	angular frequency

Dimensionless groups

Symbol	Unit	Meaning	Symbol	Unit	Meaning
Nu	–	Nusselt number	Pe_ω	–	oscillatory Péclet number
Re	–	Reynolds number	F_0	–	Fourier number

Symbol	Unit	Meaning	Symbol	Unit	Meaning
Pr	–	Prandtl number	*PR*	–	pressure ratio
St	–	Stanton number	*Θ*	–	dimensionless gas temperature

Subscripts

Index	Meaning	Index	Meaning
gas	in-cylinder gas	*meas, corr*	measured, corrected
wall	cylinder wall	*CF*	Cook–Felderman
suc, dis	suction, discharge	*CI*	cast iron
suc,hs	fast suction-pressure sensor	*r, i*	ring / real part, index / imaginary part
cyl, vessel	cylinder, discharge vessel	*sw*	swept
IVO, IVC	inlet-valve opening, closure	*D, re (D,re)*	dead (clearance) volume; re-expansion
EVO, EVC	discharge-valve opening, closure	*comp, exp*	compression, expansion
VP	valve plate	*dep*	throttling depression
C1, C2, C3	cylinder-liner sensor positions	*sv, dv*	suction-valve, discharge-valve
ref	reference	*ad, poly*	adiabatic, polytropic
TC, TC1, TC2	thermocouple; sensor	*base*	baseline value
s	sampling; Seebeck	*in*	inlet
surf	surface	*max, min*	maximum, minimum
junction	thermocouple junction	*th*	theoretical / displacement; thermal
∞	ambient / far-field	*dir, total*	direct, total
peak	peak value	*shaft*	shaft
p	piston; port	*shell*	compressor shell
H, C	hot, cold	*char*	characteristic
is	isentropic	*g*	swirl, gas
v (vol)	volumetric	*b*	reed, beam
m	mechanical; mean; mode number	*0*	initial / reference
e (el)	electrical		

Operators and accents

Notation	Meaning	Notation	Meaning
$\bar{x}$ *(over-bar)*	cycle mean	$\delta(x)$	uncertainty of x
$\dot{x}$ *(dot)*	time derivative	Δ	difference
$\langle x \rangle$	cycle-average		

Abbreviations

Abbr.	Meaning	Abbr.	Meaning
AC	alternating current	HTC	heat transfer coefficient
BDC	bottom dead centre	ICE	internal combustion engine
BFSL	best-fit straight line	IEA	International Energy Agency
CA	crank angle	ITS-90	International Temperature Scale of 1990
CF	Cook–Felderman	IVC	inlet (suction) valve closure
CFD	computational fluid dynamics	IVO	inlet (suction) valve opening
CI	cast iron	NI	National Instruments
COP	coefficient of performance	NIST	National Institute of Standards and Technology
DC	direct current	PR	pressure ratio
DV	discharge valve	PSD	power spectral density
EB	energy balance	RMS	root mean square
EFRC	European Forum for Reciprocating Compressors	RMSE	root mean square error
EMF	electromotive force	RPM	revolutions per minute
EVC	exhaust (discharge) valve closure	SI	International System of Units
EVO	exhaust (discharge) valve opening	SLA	stereolithography
FFT	fast Fourier transform	SLPM	standard litres per minute
FSI	fluid–structure interaction	SV	suction valve
FSO	full-scale output	TC	thermocouple
HFC	Heat Flux Calculator	TDC	top dead centre
HFS	heat flux sensor	TSI	reference thermal mass flow meter
HT	heat transfer	VP	valve plate

REFERENCES

[1] International Energy Agency, “The Future of Cooling: Opportunities for Energy-Efficient Air Conditioning,” OECD/IEA, Paris, 2018. doi: 10.1787/9789264301993-en.

[2] F. A. Ribas Jr., C. J. Deschamps, F. Fagotti, A. Morriesen, and T. Dutra, “Thermal Analysis of Reciprocating Compressors - A Critical Review,” in *Proceedings of the International Compressor Engineering Conference at Purdue*, West Lafayette, IN: Purdue University, 2008.

[3] A. Morriesen and C. J. Deschamps, “Experimental Investigation of Transient Fluid Flow and Superheating in the Suction Chamber of a Refrigeration Reciprocating Compressor,” *Appl. Therm. Eng.*, vol. 41, pp. 61–70, 2012, doi: 10.1016/j.applthermaleng.2011.12.011.

[4] W. J. D. Annand, “Heat Transfer in the Cylinders of Reciprocating Internal Combustion Engines,” *Proceedings of the Institution of Mechanical Engineers*, vol. 177, no. 1, pp. 973–996, 1963, doi: 10.1243/PIME_PROC_1963_177_069_02.

[5] G. Woschni, “A Universally Applicable Equation for the Instantaneous Heat Transfer Coefficient in the Internal Combustion Engine,” in *SAE Technical Paper Series*, Warrendale, PA: Society of Automotive Engineers, 1967. doi: 10.4271/670931.

[6] R. P. Adair, E. B. Qvale, and J. T. Pearson, “Instantaneous Heat Transfer to the Cylinder Wall in Reciprocating Compressors,” in *Proceedings of the International Compressor Engineering Conference at Purdue*, West Lafayette, IN: Purdue University, 1972.

[7] R. Liu and Z. Zhou, “Heat Transfer Between Gas and Cylinder Wall of Refrigerating Reciprocating Compressor,” in *Proceedings of the International Compressor Engineering Conference at Purdue*, West Lafayette, IN: Purdue University, 1984.

[8] W. H. Hsieh and T. T. Wu, “Experimental Investigation of Heat Transfer in a High-Pressure Reciprocating Gas Compressor,” *Exp. Therm. Fluid Sci.*, vol. 13, no. 1, pp. 44–54, 1996, doi: 10.1016/0894-1777(96)00013-1.

[9] F. P. Disconzi, C. J. Deschamps, and E. L. L. Pereira, “Development of an In-Cylinder Heat Transfer Correlation for Reciprocating Compressors,” in *Proceedings of the International Compressor Engineering Conference at Purdue*, West Lafayette, IN: Purdue University, 2012.

[10] R. Aigner and H. Steinrück, “Modelling Fluid Dynamics, Heat Transfer and Valve Dynamics in a Reciprocating Compressor,” in *Proceedings of the 5th Conference of the EFRC (European Forum for Reciprocating Compressors)*, Prague, Czech Republic: European Forum for Reciprocating Compressors, 2007, pp. 171–180.

[11] J. Tuhovčák, J. Hejčík, and M. Jícha, “Comparison of heat transfer models for reciprocating compressor,” *Appl. Therm. Eng.*, vol. 103, pp. 607–615, 2016, doi: 10.1016/j.applthermaleng.2016.04.120.

[12] B. Rutczyk and I. Szczygieł, “Development of internal heat transfer correlations for the cylinders of reciprocating machines,” *Energy*, vol. 230, p. 120795, 2021, doi: 10.1016/j.energy.2021.120795.

[13] L. Reichelt, U. Meingast, and U. Renz, “Calculating transient wall heat flux from measurements of surface temperature,” *Int. J. Heat Mass Transf.*, vol. 45, no. 3, pp. 579–584, 2002, doi: 10.1016/S0017-9310(01)00157-0.

[14] B. Lawton, “Effect of Compression and Expansion on Instantaneous Heat Transfer in Reciprocating Internal Combustion Engines,” *Proceedings of the Institution of Mechanical Engineers, Part A: Power and Process Engineering*, vol. 201, no. 3, pp. 175–186, 1987, doi: 10.1243/PIME_PROC_1987_201_022_02.

[15] A. C. Alkidas and J. P. Myers, “Transient Heat-Flux Measurements in the Combustion Chamber of a Spark-Ignition Engine,” *J. Heat Transfer*, vol. 104, no. 1, pp. 62–67, 1982, doi: 10.1115/1.3245069.

[16] J. B. Heywood, *Internal Combustion Engine Fundamentals*. New York: McGraw-Hill, 1988.

[17] B. Zhao, X. Jia, Y. Zhang, J. Feng, and X. Peng, “Investigation on Transient Temperature of a Reciprocating Compressor Based on a Two-Thermocouple Probe,” *International Journal of Thermal Sciences*, vol. 122, pp. 313–325, 2017, doi: 10.1016/j.ijthermalsci.2017.09.007.

[18] G. Qiu *et al.*, “Numerical Study on Unsteady Heat Transfer and Fluid Flow in a Closed Cylinder of Reciprocating Liquid Hydrogen Pumps,” *Int. J. Hydrogen Energy*, vol. 48, no. 78, pp. 30156–30169, 2023, doi: 10.1016/j.ijhydene.2023.04.145.

[19] M. Farzaneh-Gord, A. Niazmand, M. Deymi-Dashtebayaz, and H. R. Rahbari, “Thermodynamic Analysis of Natural Gas Reciprocating Compressors Based on Real and Ideal Gas Models,” *International Journal of Refrigeration*, vol. 56, pp. 186–197, 2015, doi: 10.1016/j.ijrefrig.2014.11.008.

[20] M. Mohammadi-Amin, A. R. Jahangiri, and M. Bustanchy, “Thermodynamic modeling, CFD analysis and parametric study of a near-isothermal reciprocating compressor,” *Thermal Science and Engineering Progress*, vol. 19, p. 100624, 2020, doi: 10.1016/j.tsep.2020.100624.

[21] X. Gao and Y. Liu, “Thermodynamic Analysis of a Novel Self-Air-Cooling Reciprocating Compressor,” *IEEE Access*, vol. 9, pp. 79225–79238, 2021, doi: 10.1109/ACCESS.2021.3060773.

[22] C. D. Pérez-Segarra, J. Rigola, M. Sòria, and A. Oliva, “Detailed Thermodynamic Characterization of Hermetic Reciprocating Compressors,” *International Journal of Refrigeration*, vol. 28, no. 4, pp. 579–593, 2005, doi: 10.1016/j.ijrefrig.2004.09.014.

[23] M. L. Todescat, F. Fagotti, A. T. Prata, and R. T. S. Ferreira, “Thermal Energy Analysis in Reciprocating Hermetic Compressors,” in *Proceedings of the International Compres-*

sor Engineering Conference at Purdue, West Lafayette, IN: Purdue University, 1992.

[24] J. Tuhovčák, "Development of Simulation Tool for Semi-Hermetic Compressor with the Objectives to Improve Efficiency," Brno, Czech Republic, 2017.

[25] S. W. Brok, S. Touber, and J. S. van der Meer, "Modeling of Cylinder Heat Transfer: Large Effort, Little Effect?," in *Proceedings of the Purdue Compressor Technology Conference*, West Lafayette, IN: Purdue University, 1980, pp. 43–50.

[26] F. M. Tello-Oquendo, D. C. Vásconez-Núñez, and E. Navarro-Peris, "Comparison of the Influence of Energy Losses on Efficiencies of a Scroll Compressor and a Reciprocating Compressor Used in Heat Pumps," *Información Tecnológica*, vol. 31, no. 5, pp. 205–214, 2020, doi: 10.4067/S0718-07642020000500205.

[27] Y. H. Sim, Y. Youn, and M. K. Min, "A Study on Heat Transfer and Performance Analysis of Hermetic Reciprocating Compressors for Refrigerators," in *Proceedings of the International Compressor Engineering Conference at Purdue*, West Lafayette, IN: Purdue University, 2000.

[28] R. Almbauer, W. Lang, D. Nagy, and E. Berger, "Application of Computational Fluid Dynamics for the Thermodynamic Development of a New Generation of Hermetic Reciprocating Compressor," in *Proceedings of the International Compressor Engineering Conference at Purdue*, West Lafayette, IN: Purdue University, 2010.

[29] R. Singh and W. Soedel, "Mathematical modeling of multicylinder compressor discharge system interactions," *J. Sound Vib.*, vol. 63, no. 1, pp. 125–143, 1979, doi: 10.1016/0022-460X(79)90382-1.

[30] H. E. Khalifa and X. Liu, "Analysis of Stiction Effect on the Dynamics of Compressor Suction Valve," in *Proceedings of the International Compressor Engineering Conference at Purdue*, West Lafayette, IN: Purdue University, 1998.

[31] R. A. Pizarro-Recabarren, J. R. Barbosa J, and C. J. Deschamps, "Modeling the Stiction Effect in Automatic Compressor Valves," in *Proceedings of the International Compressor Engineering Conference at Purdue*, West Lafayette, IN: Purdue University, 2012.

[32] C. J. Deschamps, F. C. Possamai, and E. L. L. Pereira, "Numerical Simulation of Pulsating Flow in Suction Mufflers," in *Proceedings of the International Compressor Engineering Conference at Purdue*, West Lafayette, IN: Purdue University, 2002.

[33] H. Steinrück, R. Aigner, and G. Machu, "Transversal waves in a reciprocating compressor," *Acta Mech.*, vol. 201, no. 1–4, pp. 231–247, 2008, doi: 10.1007/s00707-008-0061-3.

[34] W. Soedel, *Sound and Vibrations of Positive Displacement Compressors*. Boca Raton, FL: CRC Press (Taylor & Francis), 2007.

[35] J. Brablik, "Gas Pulsations as Factor Affecting Operation of Automatic Valves in Reciprocating Compressors," in *International Compressor Engineering Conference (Purdue Compressor Technology Conference)*, West Lafayette, IN, USA: Purdue University,

Ray W. Herrick Laboratories, 1972, pp. 188–195. [Online]. Available: https://docs.lib.purdue.edu/icec/29

[36] M. L. Munjal, *Acoustics of Ducts and Mufflers*, 2nd ed. Chichester, West Sussex, UK: John Wiley & Sons, Ltd, 2014.

[37] B. Zhao, X. Jia, S. Sun, J. Wen, and X. Peng, "FSI model of valve motion and pressure pulsation for investigating thermodynamic process and internal flow inside a reciprocating compressor," *Appl. Therm. Eng.*, vol. 131, pp. 998–1007, 2018, doi: 10.1016/j.applthermaleng.2017.11.151.

[38] V. M. Braga and C. J. Deschamps, "Parametric Analysis of Gas Leakage in the Piston-Cylinder Clearance of Reciprocating Compressors," *Machines*, vol. 11, no. 1, p. 42, 2023, doi: 10.3390/machines11010042.

[39] S. K. Lohn and E. L. L. Pereira, "Numerical Investigation of the Gas Leakage through the Piston-Cylinder Clearance of Reciprocating Compressors," in *Proceedings of the International Compressor Engineering Conference at Purdue*, West Lafayette, IN: Purdue University, 2014.

[40] R. T. da S. Ferreira and D. E. B. Lilie, "Evaluation of the Leakage Through the Clearance Between Piston and Cylinder in Hermetic Compressors," in *Proceedings of the International Compressor Engineering Conference at Purdue*, West Lafayette, IN: Purdue University, 1984.

[41] V. D. Overbye, J. E. Bennethum, O. A. Uyehara, and P. S. Myers, "Unsteady Heat Transfer in Engines," SAE International, Warrendale, PA, 1961. doi: 10.4271/610041.

[42] G. Sitkei, "Beitrag zur Theorie des Wärmeüberganges im Motor," *Konstruktion*, vol. 14, no. 2, pp. 67–71, 1962.

[43] T. LeFeuvre, P. S. Myers, and O. A. Uyehara, "Experimental Instantaneous Heat Fluxes in a Diesel Engine and Their Correlation," in *SAE Technical Paper Series*, Warrendale, PA: SAE International, 1969, p. 690464. doi: 10.4271/690464.

[44] W. J. D. Annand and T. H. Ma, "Instantaneous Heat Transfer Rates to the Cylinder Head Surface of a Small Compression-Ignition Engine," *Proceedings of the Institution of Mechanical Engineers*, vol. 185, no. 1, pp. 976–987, 1970, doi: 10.1243/PIME_PROC_1970_185_110_02.

[45] G. W. Recktenwald, J. W. Ramsey, and S. V Patankar, "Predictions of Heat Transfer in Compressor Cylinders," in *Proceedings of the International Compressor Engineering Conference at Purdue*, West Lafayette, IN: Purdue University, 1986.

[46] F. Fagotti, M. L. Todescat, R. T. S. Ferreira, and A. T. Prata, "Heat Transfer Modeling in a Reciprocating Compressor," in *Proceedings of the International Compressor Engineering Conference at Purdue*, West Lafayette, IN: Purdue University, 1994.

[47] A. A. Kornhauser and J. L. Smith Jr., "Application of a Complex Nusselt Number to Heat Transfer During Compression and Expansion," *Journal of Heat Transfer (Trans-*

actions of the ASME), vol. 116, no. 3, pp. 536–542, 1994, doi: 10.1115/1.2910904.

[48] E. L. L. Pereira, C. J. Deschamps, and F. A. Ribas Jr., "Numerical Analysis of Heat Transfer inside the Cylinder of Reciprocating Compressors in the Presence of Suction and Discharge Processes," in *Proceedings of the International Compressor Engineering Conference at Purdue*, West Lafayette, IN: Purdue University, 2010.

[49] F. Balduzzi, G. Ferrara, A. Babbini, and R. Maleci, "Reciprocating Compressor Cylinder's Cooling: A Numerical Approach Using CFD with Conjugate Heat Transfer," in *Proceedings of the ASME 2014 Pressure Vessels and Piping Conference (PVP2014)*, Anaheim, CA: ASME, 2014. doi: 10.1115/PVP2014-28702.

[50] X. Kang, Z. Liu, Y. Ge, X. Gao, and Y. Li, "CFD analysis and conjugate heat transfer modeling of ionic compressors," *Int. J. Hydrogen Energy*, vol. 49, pp. 264–277, 2024, doi: 10.1016/j.ijhydene.2023.07.213.

[51] K. T. Ooi, "Heat Transfer Study of a Hermetic Refrigeration Compressor," *Appl. Therm. Eng.*, vol. 23, no. 15, pp. 1931–1945, 2003, doi: 10.1016/S1359-4311(03)00150-9.

[52] A. R. Ozdemir, E. Oguz, and S. Onbasioglu, "An Investigation of the Heat Transfer Phenomena Between the Hermetic Reciprocating Compressor Components," in *8th International Conference on Compressors and their Systems*, 2013, pp. 385–395. doi: 10.1533/9781782421696.7.385.

[53] M. C. Diniz and C. J. Deschamps, "Performance Analysis of a Reciprocating Compressor under Typical Transients of Refrigeration Systems," in *Proceedings of the International Compressor Engineering Conference at Purdue*, West Lafayette, IN: Purdue University, 2016.

[54] J. Sanvezzo Jr. and C. J. Deschamps, "A Heat Transfer Model Combining Differential and Integral Formulations for Thermal Analysis of Reciprocating Compressors," in *Proceedings of the International Compressor Engineering Conference at Purdue*, West Lafayette, IN: Purdue University, 2012.

[55] R. Zhou *et al.*, "Heat Transfer Simulation for Reciprocating Compressor with Experimental Validation," in *IOP Conference Series: Materials Science and Engineering*, 2017, p. 012011. doi: 10.1088/1757-899X/232/1/012011.

[56] Z. Liu, X. Yang, X. Yang, H. Zhai, and Z. Duan, "Performance Evaluation on the In-Cylinder Heat Transfer of a Reciprocating Compressor using CO2 as a Working Fluid," *Journal of Thermal Science*, vol. 31, no. 5, pp. 1518–1530, 2022, doi: 10.1007/s11630-022-1456-5.

[57] T. Müllner and O. Bielmeier, "Heat Transfer in Small Piston Compressors," in *Proceedings of the International Compressor Engineering Conference at Purdue*, West Lafayette, IN: Purdue University, 2008.

[58] F. Fagotti and A. T. Prata, "A New Correlation for Instantaneous Heat Transfer Between Gas and Cylinder in Reciprocating Compressors," in *Proceedings of the International*

Compressor Engineering Conference at Purdue, West Lafayette, IN: Purdue University, 1998.

[59] C. D. Rakopoulos, G. M. Kosmadakis, and E. G. Pariotis, "Critical evaluation of current heat transfer models used in CFD in-cylinder engine simulations and establishment of a comprehensive wall-function formulation," *Appl. Energy*, vol. 87, no. 5, pp. 1612–1630, 2010, doi: 10.1016/j.apenergy.2009.09.029.

[60] D. Roskosch, V. Venzik, and B. Atakan, "Thermodynamic model for reciprocating compressors with the focus on fluid dependent efficiencies," *International Journal of Refrigeration*, vol. 84, pp. 104–116, 2017, doi: 10.1016/j.ijrefrig.2017.08.011.

[61] G. F. Hohenberg, "Advanced Approaches for Heat Transfer Calculations," SAE International, Warrendale, PA, 1979. doi: 10.4271/790825.

[62] J. F. Hamilton, "Extension of Mathematical Modeling of Positive Displacement Type Compressors," in *Short Course Text*, West Lafayette, IN: Ray W. Herrick Laboratories, Purdue University, 1974.

[63] J. Polman, "Heat Transfer in a Piston-Cylinder System," *Int. J. Heat Mass Transf.*, vol. 24, no. 1, pp. 184–187, 1981, doi: 10.1016/0017-9310(81)90108-3.

[64] J. Tuhovčák, J. Hejčík, and M. Jícha, "Modelling of Fluid Flow and Heat Transfer in a Reciprocating Compressor," in *IOP Conference Series: Materials Science and Engineering*, 2015, p. 012018. doi: 10.1088/1757-899X/90/1/012018.

[65] P. R. N. Childs, J. R. Greenwood, and C. A. Long, "Heat Flux Measurement Techniques," *Proc. Inst. Mech. Eng. C J. Mech. Eng. Sci.*, vol. 213, no. 7, pp. 655–677, 1999, doi: 10.1177/095440629921300702.

[66] C. T. Kidd and J. C. Adams Jr., "Fast-Response Heat-Flux Sensor for Measurement Commonality in Hypersonic Wind Tunnels," *J. Spacecr. Rockets*, vol. 38, no. 5, pp. 719–729, 2001, doi: 10.2514/2.3738.

[67] D. L. Schultz and T. V Jones, "Heat-Transfer Measurements in Short-Duration Hypersonic Facilities," Advisory Group for Aerospace Research and Development (AGARD), NATO, Paris, 1973.

[68] T. Dutra and C. J. Deschamps, "Experimental characterization of heat transfer in the components of a small hermetic reciprocating compressor," *Appl. Therm. Eng.*, vol. 58, no. 1–2, pp. 499–510, 2013, doi: 10.1016/j.applthermaleng.2013.04.039.

[69] J. Taler and P. Duda, *Solving Direct and Inverse Heat Conduction Problems*. Berlin, Heidelberg: Springer, 2006. doi: 10.1007/978-3-540-33471-2.

[70] S. Zhang, Q. Wang, J. Li, X. Zhang, and H. Chen, "Coaxial Thermocouples for Heat Transfer Measurements in Long-Duration High Enthalpy Flows," *Sensors*, vol. 20, no. 18, p. 5254, 2020, doi: 10.3390/s20185254.

[71] J. Taler, "Theory of transient experimental techniques for surface heat transfer," *Int. J. Heat Mass Transf.*, vol. 39, no. 17, pp. 3733–3748, 1996, doi: 10.1016/0017-

9310(96)00015-4.

[72] W. J. Cook and E. J. Felderman, “Reduction of Data from Thin-Film Heat-Transfer Gages: A Concise Numerical Technique,” *AIAA Journal*, vol. 4, no. 3, pp. 561–562, 1966, doi: 10.2514/3.3486.

[73] K. J. Irimpan, N. Mannil, H. Arya, and V. Menezes, “Performance evaluation of coaxial thermocouple against platinum thin film gauge for heat flux measurement in shock tunnel,” *Measurement*, vol. 61, pp. 291–298, 2015, doi: 10.1016/j.measurement.2014.10.056.

[74] M. N. Özişik and H. R. B. Orlande, *Inverse Heat Transfer: Fundamentals and Applications*, 2nd ed. Boca Raton, FL: CRC Press, 2021.

[75] S. R. Sanderson and B. Sturtevant, “Transient heat flux measurement using a surface junction thermocouple,” *Review of Scientific Instruments*, vol. 73, no. 7, pp. 2781–2787, 2002, doi: 10.1063/1.1484255.

[76] U. Meingast, M. Staudt, L. Reichelt, U. Renz, and F.-A. Sommerhoff, “Analysis of Spray/Wall Interaction Under Diesel Engine Conditions,” in *SAE Technical Paper Series*, Warrendale, PA: Society of Automotive Engineers, 2000. doi: 10.4271/2000-01-0272.

[77] S. Agarwal, N. Sahoo, and R. K. Singh, “Experimental techniques for thermal product determination of coaxial surface junction thermocouples during short duration transient measurements,” *Int. J. Heat Mass Transf.*, vol. 103, pp. 327–335, 2016, doi: 10.1016/j.ijheatmasstransfer.2016.07.062.

[78] S. K. Manjhi and R. Kumar, “Surface heat flux measurements for short time-period on combustion chamber with different types of coaxial thermocouples,” *Experimental Heat Transfer*, vol. 33, no. 3, pp. 282–303, 2020, doi: 10.1080/08916152.2019.1630031.

[79] G. Li, X. Cheng, H. Meng, T. Deng, and C. Yang, “The introduced error associated with the contact-type detection for piston surface temperature in combustion engines using coaxial thermocouples and its eliminating algorithm,” *Int. J. Heat Mass Transf.*, vol. 195, p. 123170, 2022, doi: 10.1016/j.ijheatmasstransfer.2022.123170.

[80] S. Park, H. Lee, B. Jang, J. Kim, and G. Park, “Technical study of fast-response coil-type coaxial surface junction thermocouple,” *Journal of Mechanical Science and Technology*, vol. 38, no. 3, pp. 1463–1471, 2024, doi: 10.1007/s12206-024-0238-2.

[81] S. K. Manjhi and R. Kumar, “Comparative Performance of K, E, and J-Type Fast Response Coaxial Probes for Short-Period Transient Measurements,” *J. Therm. Sci. Eng. Appl.*, vol. 13, no. 3, p. 031029, 2021, doi: 10.1115/1.4048664.

[82] D. R. Buttsworth, “Assessment of Effective Thermal Product of Surface Junction Thermocouples on Millisecond and Microsecond Time Scales,” *Exp. Therm. Fluid Sci.*, vol. 25, no. 6, pp. 409–420, 2001, doi: 10.1016/S0894-1777(01)00093-3.

[83] L. Qi, G. Han, Z. Hu, C. Wang, and Z. Jiang, “Numerical investigations of the lateral

heat transfer in coaxial thermocouples," *Numeri. Heat Transf. A Appl.*, vol. 82, no. 6, pp. 280–298, 2022, doi: 10.1080/10407782.2022.2078586.

[84] L. Qi, G. Han, and Z. Jiang, "Optimal design of E-type coaxial thermocouples for transient heat measurements in shock tunnels," *Appl. Therm. Eng.*, vol. 218, p. 119388, 2023, doi: 10.1016/j.applthermaleng.2022.119388.

[85] D. N. Assanis and E. Badillo, "On Heat Transfer Measurements in Diesel Engines Using Fast-Response Coaxial Thermocouples," *J. Eng. Gas Turbine. Power*, vol. 111, no. 3, pp. 458–465, 1989, doi: 10.1115/1.3240276.

[86] P. Bouchal, J. Hejčík, and M. Jícha, "Heat Flux Assessment in Reciprocating Compressor," in *EPJ Web of Conferences*, EDP Sciences, 2024, p. 01004. doi: 10.1051/epjconf/202429901004.

[87] T. Ahn, J. Kang, J. J. Jeong, and B. Yun, "Measurement of local wall temperature and heat flux using the two-thermocouple method for a heat transfer tube," *Nuclear Engineering and Technology*, vol. 51, no. 7, pp. 1853–1859, 2019, doi: 10.1016/j.net.2019.05.007.

[88] P. D. Welch, "The Use of the Fast Fourier Transform for the Estimation of Power Spectra: A Method Based on Time Averaging Over Short, Modified Periodograms," *IEEE Transactions on Audio and Electroacoustics*, vol. 15, no. 2, pp. 70–73, 1967, doi: 10.1109/TAU.1967.1161901.

[89] P. Rapta, J. Hejčík, and M. Jícha, "Thermocouple Influence on Heat Transfer Coefficient Measurement," in *Proceedings of the 10th IIR Conference on Compressors and Refrigerants*, Slovakia: International Institute of Refrigeration, 2024. doi: 10.18462/iir.compr.2024.0614.

[90] H. S. Carslaw and J. C. Jaeger, *Conduction of Heat in Solids*, 2nd ed. Oxford: Clarendon Press, 1959.

[91] A. I. Taleb, C. Barfuss, P. Sapin, A. J. White, D. Fabris, and C. N. Markides, "Simulation of thermally induced thermodynamic losses in reciprocating compressors and expanders: Influence of real-gas effects," *Appl. Therm. Eng.*, vol. 217, p. 118738, 2022, doi: 10.1016/j.applthermaleng.2022.118738.

[92] H. Pfriem, "Nichtstationäre Wärmeübertragung in Gasen, insbesondere in Kolbenmaschinen," VDI-Verlag, Berlin, 1942. doi: 10.1007/BF02586004.

[93] W. J. D. Annand and D. Pinfold, "Heat Transfer in the Cylinder of a Motored Reciprocating Engine," in *SAE Technical Paper Series*, Warrendale, PA: Society of Automotive Engineers, 1980. doi: 10.4271/800457.

[94] A. Bejan, *Convection Heat Transfer*, 4th ed. Hoboken, NJ: John Wiley & Sons, 2013. doi: 10.1002/9781118671627.